A BIOMECHANICAL INVESTIGATION OF A NOVEL IMPLANT FOR THE STABILIZATION OF DISTAL RADIUS FRACTURES

By

Andrew Allan

Submitted in partial fulfilment of the requirements
for the degree of Master of Applied Science

at

Dalhousie University
Halifax, Nova Scotia
August 2012

DALHOUSIE UNIVERSITY

SCHOOL OF BIOMEDICAL ENGINEERING

The undersigned hereby certify that they have read and recommend to the Faculty of Graduate Studies for acceptance a thesis entitled "A BIOMECHANICAL INVESTIGATION OF A NOVEL IMPLANT FOR THE STABILIZATION OF DISTAL RADIUS FRACTURES" by Andrew Allan in partial fulfilment of the requirements for the degree of Master of Applied Science.

Dated: August 15, 2012

External Examiner:

_____

Dr. Darrel Doman

Supervisor:

_____

Dr. Michael Dunbar

Readers:

_____

Dr. Janie Astephen-Wilson

_____

Dr. Mark Filiaggi

DALHOUSIE UNIVERSITY

DATE: August 15, 2012

AUTHOR: Andrew Allan

TITLE: A BIOMECHANICAL INVESTIGATION OF A NOVEL IMPLANT FOR THE STABILIZATION OF DISTAL RADIUS FRACTURES

DEPARTMENT OR SCHOOL: School of Biomedical Engineering

DEGREE: MASc CONVOCATION: October YEAR: 2012

_____

Signature of Author

TABLE OF CONTENTS

LIST OF TABLES

LIST OF FIGURES

ABSTRACT

Distal radius fractures are the single most common type of fracture suffered among the adult population. Presently, clinical decision making regarding optimal treatment of distal radius fractures is inconclusive. There has been a recent trend towards increased use of open reduction and internal fixation with locked volar plates. This method of treatment is known to provide an earlier return to function than more conservative modes of treatment, but at a much higher cost. The goal of this thesis was to design, develop, and biomechanically test a novel implant for the stabilization of distal radius fractures. The novel implant is intended to provide a minimally invasive, low cost alternative to locked volar plates, while still permitting an earlier return to function.

The novel implant consists of an angled bar with a sharp cutting edge that allows it to penetrate through bone. The implant is inserted using a minimally invasive approach through the radial styloid at an angle that allows it to bridge a distal radius fracture. Surgical instrumentation was designed to facilitate the procedure in a controlled manner. To determine whether the implant would be capable of providing an early return to function, biomechanical tests were conducted both experimentally and numerically.

In vitro experimental tests were performed on both foam cortical shell and composite sawbones. Results showed the novel implant to be inferior to a conventional percutaneous pinning treatment in foam cortical shell sawbones. The nature of the implant design caused high stresses at the implant/bone interface resulting in failure of the synthetic bone material below simulated physiological loads. Additional testing in composite sawbones demonstrated that in stronger bones implant failure would occur at the low end of anticipated physiological loads. Experimental results were used to validate a finite element model of the novel implant. The finite element model confirmed the implants inability to provide an early return to function in human bone. Based on experimental and numerical results the novel implant is not recommended for clinical use.

LIST OF ABBREVIATIONS USED

Abbreviation	Long Form
1D	One Dimensional
2D	Two Dimensional
3D	Three Dimensional
AP	Anteroposterior
CAD	Computer-aided Design
CT	Computed Tomography
FCS	Foam Cortical Shell
FEA	Finite Element Analysis
IFM	Interfragmentary Motion
IFS	Interfragmentary Strain
K-wire	Kirschner Wire

ACKNOWLEDGEMENTS

I would like to first thank the Orthopaedic Research Group for providing me with the opportunity to continue my education in the field of Biomedical Engineering. This includes: Allan Hennigar and Elise Laende, who were always available to answer questions and provide me with the resources necessary to complete my research; as well, Carrie Anderson who always found the time to fit me into Dr. Dunbar's schedule. I would like to acknowledge Dave Wilson for introducing me to the School of Biomedical Engineering and for all of the help and support he has offered me throughout this project. I could always count on him for advice and valuable insight on new design ideas.

I would also like to acknowledge the help I have received from outside of the Orthopaedic Research Group: Andrew Yabsley, for offering me his expertise in machining; Dr. Dean Forgeron and Phil Vickers, for their assistance in conducting experimental testing; Dr. Darrel Doman, for helping me understand finite element analysis and allowing me access to his lab equipment; and Martin Petrak, for giving me the chance to complete an internship with his group at the Concordia Hip & Knee Institute in Winnipeg, MB. In addition, I would like to thank the funding bodies that have provided me with the opportunity to complete this research: the Natural Sciences and Engineering Research Council of Canada and Innovacorp.

I feel fortunate to have had a supervisory committee that was both helpful and supportive. I would like to give a special thanks to Dr. Janie Astephen-Wilson and Dr. Mark Filiaggi for their guidance and never hesitating to give me feedback as needed. Finally and most importantly, I want to thank my supervisor Dr. Michael Dunbar for giving me the opportunity to pursue a Graduate Degree in Biomedical Engineering. His enthusiasm and positive perspective helped keep me inspired and showed me the value of my research.

This degree would not have been possible without the continued support of my parents and for that I am extremely grateful.

CHAPTER 1 INTRODUCTION

Distal radius fractures are the single most common type of fracture suffered among the adult population. This injury was first classified in 1814 by an Irish surgeon named Abraham Colles and is frequently referred to as a Colles' fracture (Colles, 1814). Presently, clinical decision making regarding optimal treatment of distal radius fractures is inconclusive (AAOS Now, 2009). Although a number of treatment methods currently exist, the lack of a definitive approach presents a unique opportunity to explore alternative treatment methods. The goal of this thesis is to investigate a novel treatment that is intended to improve how distal radius fractures are managed. This chapter will provide the necessary background to understand: the injury as well as existing treatment options, the testing and validation of novel orthopaedic devices including a review of the pertinent literature, and the research objectives of this thesis.

1.1 Anatomy

Comprehension of a distal radius fracture begins by first understanding the gross anatomy and medical terminology used to describe the arm and hand. The anatomical term 'distal' is used to identify the furthest point on an appendage from the point of attachment. Contrarily, the term 'proximal' is used to identify the point on an appendage nearest to the point of attachment. The terms 'dorsal' and 'volar' refer to the back side and palmar side of the hand and arm, respectively. The radius bone is one of two long bones that comprise the skeletal structure of the forearm, the second is the ulna. These two bones are connected by a flat sheet of ligament called the interosseous membrane and also by a synovial joint at both their proximal and distal ends. These two joints, known as radio-ulnar joints, permit rotation of the radius around the ulna, a movement referred to as pronation and supination. The radius bone widens at its distal end forming the radio-carpal (wrist) joint with two carpal bones, the scaphoid and lunate. The radio-carpal joint permits flexion and extension of the hand as well as radial and ulnar deviation. The orientation of these bones and important landmarks can be seen in Figure 1.1 and Figure 1.2. Anatomical movements of the hand are described in Figure 1.3.

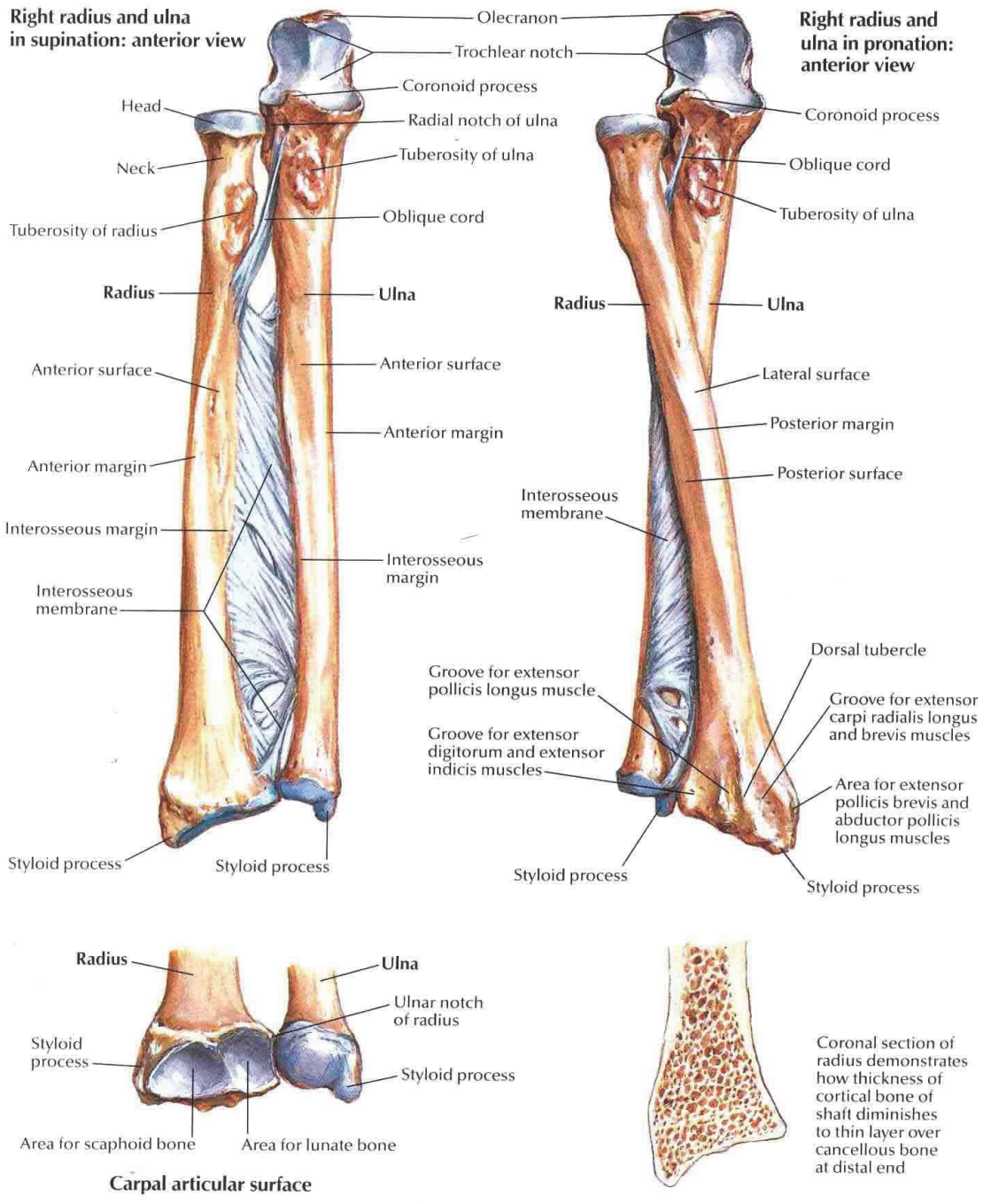

Figure 1.1: Anatomy of the radius and ulna bones (Netter et al., 2012)

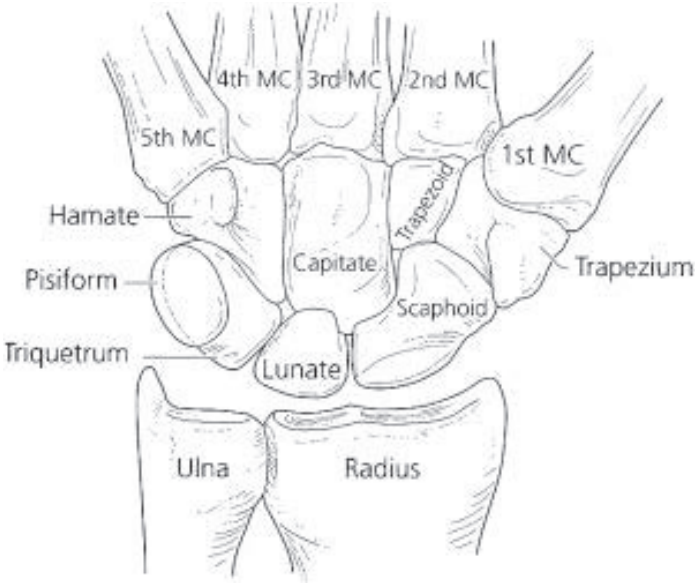

Figure 1.2: Osseous anatomy of the wrist (Steinburg et al., 1995)

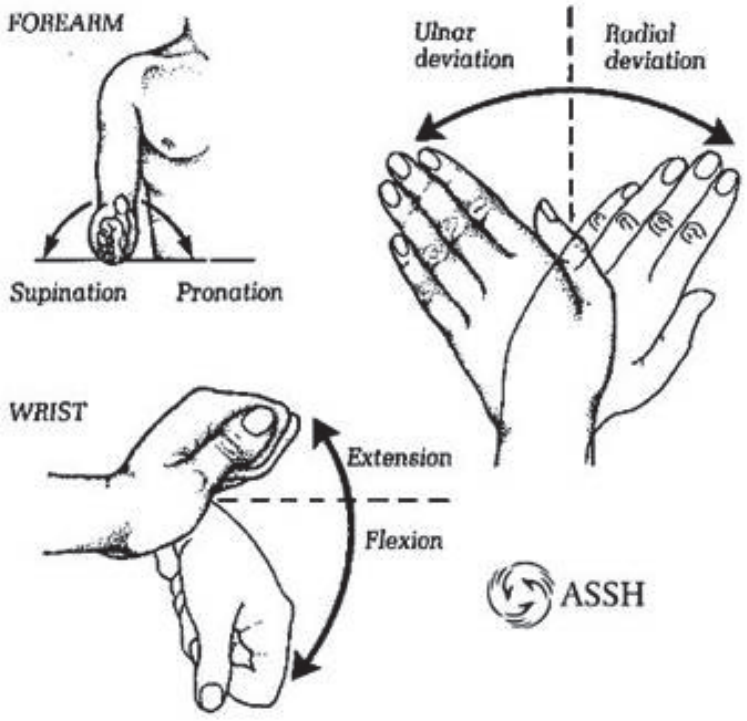

Figure 1.3: Terminology for describing motion of the hand (American Society for Surgery of the Hand, 2009)

1.2 Distal Radius Fractures

A distal radius fracture refers to any fracture of the radius bone that occurs within the distal region extending approximately an inch and a half proximal to the radio-carpal joint (Colles, 1814).

1.2.1 Incidence and Epidemiology

Distal radius fractures account for roughly 17.5% of all fractures treated in emergency departments (Court-Brown, 2006). The annual occurrence of distal radius fractures has been reported to be greater than 500,000 in the United States alone (Frost & Sullivan, 2003). Previous studies have shown the overall incidence rate to be anywhere from 195 to 383/100,000 person-years (Brogren et al., 2007; Court-Brown, 2006; Flinkkila et al., 2010). The incidence of this injury is described by a bimodal distribution with the highest rates occurring in the pediatric and elderly patient populations (Court-Brown, 2006; Nellans et al., 2012). For the pediatric population, distal radius fractures account for up to 23% of all fractures with boys being at greater risk (Wood et al., 2010). The high incidence in children is attributed to their rapidly developing skeletal structure and increased participation in sport-related activities (Nellens et al., 2012; Wood et al., 2010). For the elderly population, the high incidence of fractures is correlated to the high prevalence of osteoporosis. Osteoporosis is a skeletal disorder characterized by low bone mass and compromised bone strength resulting in increased bone fragility and susceptibility to fracture (Consensus Development Conference on Osteoporosis, 1990). Its prevalence is higher in women as a result of a drop in estrogen levels at the time of menopause. Therefore, beyond the age of 50 years the risk of an osteoporotic fracture for females begins to rise (Kannus et al, 2001). It has been estimated that 372,000 people aged 65 or greater experience a distal radius fracture each year in the United States (Diaz-Garcia et al. 2011).

Clinical data points to an increase in the incidence of distal radius fractures in recent years (Nellens et al., 2012). A major contributing factor is an aging population with an increased life expectancy due to improved health care. In addition, our population is becoming accustomed to living healthier and more active lifestyles into their later years

(Jupiter, 2012). The already high incidence of distal radius fractures in combination with the expected rise has lead to an increase in overall demand for orthopaedic intervention.

1.2.2 Fracture Mechanisms

A distal radius fracture can result from any degree of trauma whether it is mild, moderate, or high energy. In the preadolescent and young adult patient population the mechanism of injury is typically a high energy trauma such as a motor vehicle accident or sports-related injury. In the elderly population often affected by osteoporosis a simple fall from standing onto an extended hand can be enough to cause injury (Beil et al., 2011). Hand positioning and the direction of impact loads influence how forces are transferred through the radius and will often determine the type of fracture. The three general loading scenarios that can cause a distal radius fracture are bending, shear and compression.

Fernandez was the first to attempt to classify distal radius fractures using a patho-mechanical approach (Fernandez, 2001). His classification system is displayed in Figure 1.4. The most common fracture is a Type I resulting from an externally applied bending load (Flinkkila, 2010). A dorsally angulated bending load on the radius causes high tensile forces on the volar metaphysis and high compressive forces on the dorsal metaphysis (Cooney et al, 1991; Fernandez, 2001). Depending on the impact load and patient's bone quality, compression forces on the dorsal side of the radius can lead to varying degrees of metaphyseal comminution. The degree of comminution has a direct influence on fracture stability, which is important when deciding how to manage a fracture. This type of fracture would be expected from a fall onto an extended hand and is representative of a traditional Colles' fracture. Similarly, a fall onto a flexed hand may result in a Type I fracture; however this is far less common. The failure load of a radius depends on factors such as bone quality and

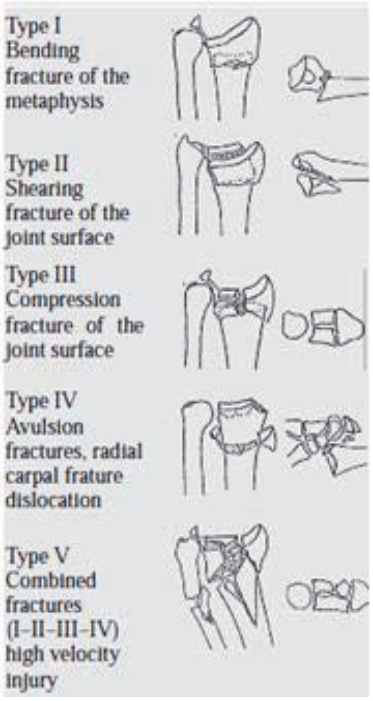

Figure 1.4: Fracture types based on mechanism of injury (Fernandez, 2001)

direction of load and has been shown experimentally to be in the range of 1600-3400 N (Augat et al., 1998; Muller et al., 2003; Pistoia et al., 2002).

A Type II fracture occurs when the bone is forced in two opposing directions creating a shearing force. As the force exceeds the shear strength of the bone, the fractured fragment begins to displace away from the intact radial shaft. The entire joint cartilage is often sheared away with the underlying bone. The involvement of the joint surface and the inherently small size of the fractured fragment make this type of fracture difficult to treat (Wolfe, 2007). Type III fractures, or compression fractures, are caused by large axial compressive loads on the hand. Compressive loads have a tendency to drive the carpal bones into the radio-carpal joint surface. This type of fracture is typically caused by a high energy trauma as a significant load is required to yield the bone in compression (Wolfe, 2007). Type IV and V fractures represent more complex fracture patterns resulting from catastrophic high energy traumas and are far less frequent. Type IV fractures show dislocation of the radio-carpal joint and a Type V fracture signifies a combination of fracture Types I-IV.

1.2.3 Fracture Diagnosis

Despite the high incidence of distal radius fractures, optimal treatment selection continues to be a topic for debate in the literature. Several factors influence management decisions including fracture type, bone quality, patient co-morbidities, and personal experience of the surgeon. In an attempt to standardize treatment selection, Cherubino et al. (2010) summarized a set of diagnosis criteria that consists of fracture type, fracture displacement, reduction acceptability criteria, fracture instability parameters and associated joint lesions. This set of criteria is intended to guide optimal treatment selection.

Fracture type is assessed by radiographic examination using lateral and anteroposterior (AP) projections. Important characteristics used to define the type of fracture include extent of articular joint involvement, degree of comminution, fracture displacement, and associated ulna injuries. In addition to the patho-mechanical classification system developed by Fernandez (Fernandez, 2001), other classification systems have been proposed in the literature including AO (Muller, 1991), Frykman

(1997), Melone (1984), and Universal (Cooney, 1993). Although inter and intra-observer reliability for each classification system have been doubted (Kural et al, 2010), basic fracture characteristics such as articular joint involvement are useful in determining how to manage a fracture. A fracture that does not disrupt the articular surface of the radio-carpal joint is considered to be extra-articular, while an intra-articular fracture indicates some degree of joint surface involvement. Minimally displaced extra-articular fractures, often a result of low energy traumas, are more easily treated than intra-articular distal radius fractures. Intra-articular fractures are common in young adults and comprise a more complex subgroup of patients. These injuries are inherently unstable, are difficult to reduce, and cannot be immobilized with a conservative treatment. For these reasons it is believed that distal radius fractures in young adults are more disabling than osteoporotic extra-articular fractures suffered by the elderly (Gliatis et al., 2000).

Fracture displacement is an important factor used to assess the reducibility of a fracture. This measure is also quantified by radiographic examination and helps define fracture stability. In an attempt to establish the essential radiographic measurements Van Der Linden and Ericson (1981) conducted a study to determine the co-variation between various measures of displacement. The radiographic parameters that were used to define displacement of distal radius fractures included dorsal angle, dorsal shift, radial angle, radial shortening, and radial shift as shown in Figure 1.5 and Figure 1.6. The study concluded that displacement can be defined with only two measurements, one for dorsal and one for radial displacement.

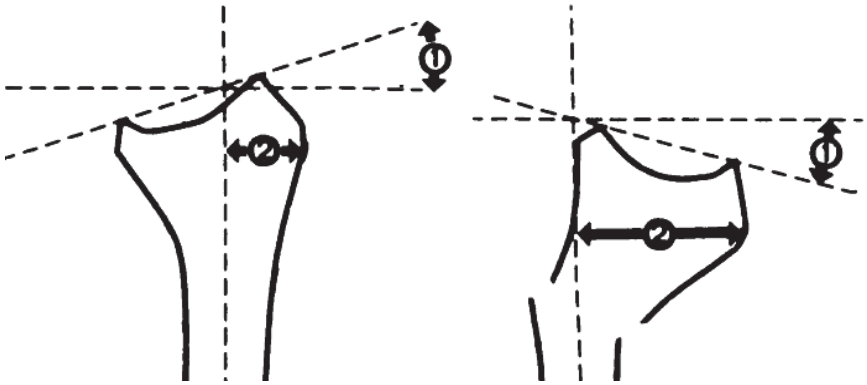

Figure 1.5: Lateral radiographic measures of fracture displacement, (1) dorsal angle, (2) dorsal shift (Van Der Linden and Ericson, 1981)

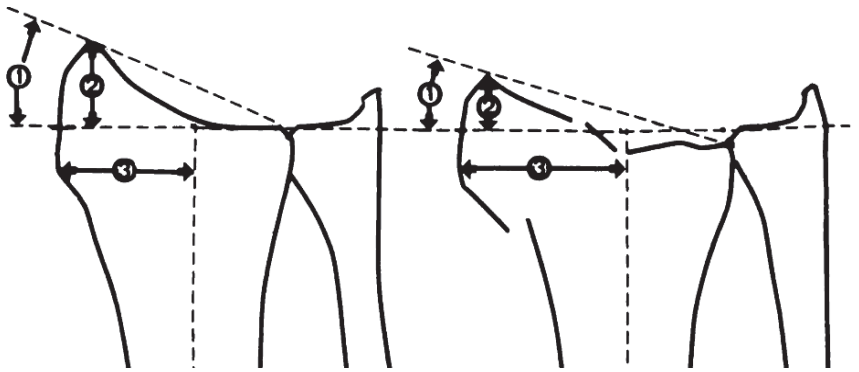

Figure 1.6: AP radiographic measures of fracture displacement. (1) radial angle, (2) radial shortening, (3) radial shift (Van Der Linden and Ericson, 1981)

Anatomical reduction of a distal radius fracture is not always necessary to achieve good outcomes. Fernandez (2000) suggested that good outcomes can be attained if the following reduction criteria are met: dorsal tilt less than 10^{o}, radial shortening less than 2 mm, radial inclination greater than 15^{o}, distal radio-ulnar joint congruence, and an articular step off less than 2 mm. The ability to maintain a good reduction is important to consider when choosing an appropriate treatment plan. The probability of a secondary re-displacement is dependent on the stability of a fracture. Lafontaine et al. (1989) described fracture instability parameters as: a dorsal angle greater than 20^{o}, dorsal bone comminution, an intra-articular fracture line, presence of an ulna fracture, and patient age greater than 60 years. It is believed that the presence of three or more of these instability parameters increases the probability for a loss of reduction (Cherubino et al., 2010). These diagnosis parameters are often used to guide treatment selection and predict clinical outcomes.

1.2.4 Fracture Management and Bone Healing

From a mechanical perspective there are two primary objectives when managing a fracture. First, the fractured bone should be restored to its anatomical position. Second, the fractured bone should be fixed to prevent re-displacement while promoting new bone formation. A large number of patient and biological factors influence fracture management and bone healing; however, for this thesis only mechanical factors were evaluated.

For distal radius fractures anatomical reconstruction of both the radio-carpal and radio-ulnar joint architecture are pre-requisites for restoration of normal wrist kinematics (Fernandez, 2000). Good functional outcomes in young adults have been associated with adequate restoration of the original anatomy based on radiographic evidence (Gliatis, 2000). Maintaining a good anatomical reduction in elderly patients can be more difficult and increased age has been shown as a good predictor of secondary re-displacement (Hollevoet, 2010). This can be attributed to compromised stability in osteoporotic bone due to bone impaction and fracture fragmentation. Mal-union rates in patients above the age of 60 years were reported to be as high as 50% in one review (Gehrmann et al., 2008). Interestingly, many studies have shown the correlation between radiographic and clinical outcomes to be insignificant in low demand elderly patients (Anzarut et al., 2004; Beumer et al., 2003; Hollevoet, 2010; Kilic et al., 2009). However, as our elderly population begins to live more active lifestyles, achieving and maintaining an anatomical reduction is desirable.

There are two standard techniques used to re-align a fractured distal radius: a closed reduction or open reduction. A closed reduction is performed by manual manipulation of fractured fragments without skin incisions. Manipulation of fractured fragments can be achieved through a combination of traction and palpation. A typical closed reduction approach for an extra-articular distal radius fracture is longitudinal traction with minor volar flexion and ulnar deviation (AO foundation). The majority of distal radius fractures present as dorsally displaced, so this approach serves to disimpact the fractured fragment and restore correct alignment. Traction can be applied manually or using finger traps connected to counterweights. If a fracture cannot be reduced using a closed technique, an open reduction is performed. An open reduction requires an invasive procedure in which the patient's wrist is surgically exposed. This permits direct visualization of the bone allowing an accurate reduction to be achieved more easily.

Once a fracture has been reduced the ultimate goal is to provide fixation that will prevent re-displacement and promote bone healing. Research has shown the degree of fixation will dictate the process through which bone heals. In general, the degree of fracture fixation is described by relative or absolute stability. Bone healing through relative stability is characterized by the formation of an intermediate callus prior to bone

formation and is referred to as ‘secondary bone healing’. Secondary bone healing occurs in three main phases: inflammation, repair, and remodeling. The inflammatory phase begins immediately at the time of injury with the formation of a hematoma at the fracture site. The hematoma sets the stage for the repair phase by releasing growth factors, stimulating angiogensis and bone formation (Mizuno et al., 1990; Street et al., 2000). Resorption of necrotic bone is also carried out during this phase through the signaling of osteoclasts (Millis, 1999). The inflammatory phase lasts approximately 3-7 days and concludes with a decrease in swelling and pain followed by the repair phase. The repair phase signifies the transformation of the hematoma into granulation tissue. As granulation tissue matures into connective tissue, collagen fibres become more abundant and interfragmentary motion (IFM) at the fracture site decreases. Perren (1980) proposed a theory that bone formation will only occur in a stable biomechanical environment where interfragmentary strain (IFS) is less than 2%. IFS is equivalent to the IFM at the fracture site divided by the original fracture gap width (Claes et al., 1998). The percent of IFS influences the type of tissue that forms at a fracture site. During the repair phase of secondary bone healing a soft callus forms and eventually, through mineralization converts to a hard callus. Callus formation begins to restore bone strength and stiffness, reducing IFM to a point that allows compact bone formation. The formation of a soft callus takes 2-3 weeks while hard callus formation can take anywhere from 4-16 weeks. At the end of the repair phase the bone is strong enough for low impact exercise and the remodeling phase begins. This is the final phase in which bone remodels to adapt for optimal function and strength. The remodeling phase can take several years to be completed.

Fracture management with absolute stability promotes direct bone healing without intermediate callus formation. This mode of healing was first discovered by Danis (1949) and was termed ‘primary bone healing’. Based on Perren’s strain theory primary bone healing will occur if IFS is less than 2%. Primary bone healing can occur either by means of contact healing or gap healing. Contact healing can be expected when the defect between bone ends is less than 0.01 mm (Mann et al., 1989; Shapiro, 1988). This results in direct formation of lamellar bone parallel to the long axis, (Mann et al., 1989; Rahn, 2002) with bone union and remodeling occurring simultaneously (Kaderly, 1991). Direct

bone formation can also occur through gap healing if defect sizes are less than 1.0 mm and IFS is less than 2% (Kaderly, 1991). Gap healing is characterized by direct formation of lamellar bone perpendicular to the long axis filling the fracture gap. The perpendicular orientation of the bone has inherently weak mechanical strength and thus a secondary remodeling phase begins after 3-8 weeks (Johnson et al., 2002). Both primary and secondary bone healing are considered to be acceptable in fracture care. The literature suggests an IFS < 2-5% will result in primary bone healing while an IFS < 15% will stimulate secondary bone healing (Claes et al., 1998; Egol et al., 2004; Perren et al, 1980).

1.2.5 Existing Treatments and Fracture Fixation Devices

A number of treatment options exist for distal radius fractures ranging from conservative management to varying degrees of surgical intervention. Treatment selection is dependent on the fracture diagnosis criteria previously described in this chapter. The four primary treatment methods include: conservative management, percutaneous pinning, external fixation, and internal fixation.

Conservative Management

Conservative management is performed with a closed reduction and cast immobilization. Indications for conservative treatment are low-demand patients presenting with stable fractures showing minimal displacement. Hand positioning within the cast is dependent on fracture type, although extreme deviations from the neutral position should be avoided (AO Foundation). After the cast has been applied it should be split in the longitudinal direction and spread slightly to avoid constriction during post-traumatic swelling. Once all swelling has subsided the cast is closed and the arm is immobilized for a minimum of 6 weeks. Conservative management is a simple, cost effective treatment option; however, potential complications resulting from a long immobilization period include joint stiffness and muscle dystrophy. Despite preserving good radial alignment, conservative management provides minimal axial stability and therefore is not recommended for active patients or unstable fractures (Gofton et al., 2010).

Percutaneous Pinning

Conservative treatment is often supplemented with percutaneous pinning for additional fracture stability. The primary indications for this treatment method are patients with high functional demands and unstable extra-articular fractures. The procedure is performed with a closed reduction followed by insertion of kirschner wires (k-wires) and cast immobilization. K-wires are inserted percutaneously through the skin and pass across a fracture for improved fixation. Positioning of these wires is fracture specific; however, typical entry points are through the radial styloid and dorso-ulnar rim of the radius as shown in Figure 1.7. This treatment helps maintain an anatomical reduction while limiting damage to the surrounding soft tissue (Keast-Butler et al., 2008). Pins are left in for 4-6 weeks and casts are typically removed during the 6 week follow up (Cherubino et al., 2010; Gofton et al., 2010). Percutaneous pinning is advantageous because it is a cost effective, minimally invasive method of enhancing fracture stability. However, k-wire fixation may be compromised in osteoporotic bone with the risk of re-displacement. Surgeons must be careful when positioning k-wires to prevent nerve injury, and pin site care is important to prevent infection.

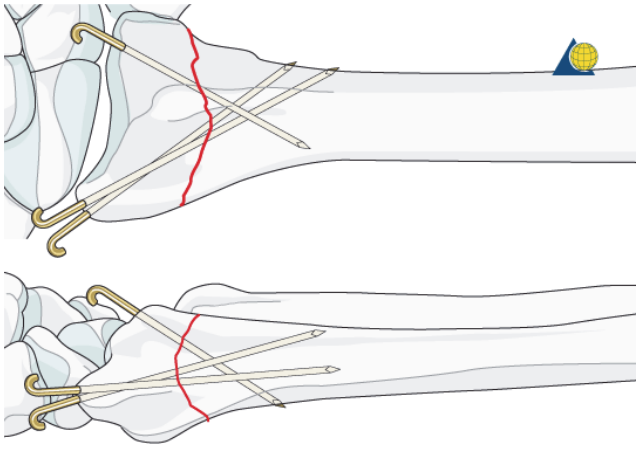

Figure 1.7: Standard k-wire technique for AO Type A3 fracture. (AO Foundation)

External Fixation

External fixation offers another minimally invasive surgical treatment and is indicated for unstable extra-articular fractures in active patients. Again, the procedure begins with a closed reduction followed by the insertion of percutaneous pins. These pins are then connected with an external fixation device. There are two techniques used to apply external fixation: bridging and non-bridging. A bridging external fixator connects pins placed proximal to the fracture with pins placed distal to the fracture site. This serves to distract the radius and off-load the fractured fragment(s). This can be helpful when

problems associated with gaining fixation in the fractured fragment(s) are present (Keast-Butler et al., 2008). Also, it helps reduce extrinsic forces which are a primary cause of fracture re-displacement. K-wires are sometimes used in addition to external fixation for more complex unstable fractures. Non-bridging external fixators are used to directly fix the fractured fragment(s) to the proximal intact radius. This approach requires a large distal fragment for adequate fixation (Keast-Butler et al., 2008). Figure 1.8 displays Stryker's Hoffmann II External Fixation System that includes both bridging and non-bridging frames. Similar to percutaneous pinning, risks such as pin site infection, nerve injury, and extensor tendon injury exist when using external fixation.

Figure 1.8: Stryker Hoffmann II External Fixation System (left: bridging, right: non-bridging) (Stryker, Trauma)

Internal Fixation

Internal fixation is indicated for complex intra-articular fractures which are inherently unstable. A standard treatment approach begins with an open reduction followed by internal fixation with a plate and screws. Original plates were designed to be implanted on the dorsal side of the radius for optimal fixation, as most fractures present as dorsally displaced. Conventional plating techniques rely on large compression forces at the plate/bone interface in order to resist motion. With this design, axially applied loads are counteracted by the frictional force generated between the plate and bone. The frictional force is equal to the normal force, which is a function of screw torque, multiplied by the coefficient of friction at the interface. Therefore, good purchase between the screw and bone is necessary to achieve a good fixation. Good screw purchase can be difficult to attain in osteoporotic bone limiting the effectiveness of this design. Figure 1.9 shows how conventional compression plates resist axially applied

loads. Dorsal compression plates proved to be capable for stabilizing fractures; however, there was a high complication rate associated with extensor tendon injury. The dorsal side of the radius has a convex shape forcing dorsal plates to lie in direct contact with the extensor tendons. This resulted in a high incidence of extensor tendon complication including irritation, attrition, and rupture (Martineau et al, 2010).

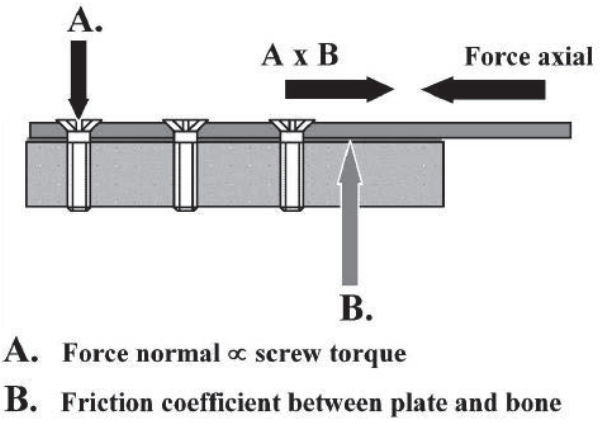

Figure 1.9: Engineering principles of conventional plate designs (Egol et al., 2004)

The high complication rate linked to dorsal plating led to the development of volar locked plates. Volar locked plates are now considered the standard of care for open reduction and internal fixation of distal radius fractures. A volar approach has the benefit of a thick soft tissue layer, and the plate can be positioned beneath the pronator quadratus muscle preventing flexor tendon irritation (Keast-Butler et al., 2008). Locked plate technology consists of screw heads that can rigidly fix to the plate establishing a 'locked' connection. This minimizes the need for good screw purchase because the plate-screw construct acts as a fixed angled implant. This design allows axially applied loads to be transferred as compression forces over the entire body of each screw as shown in Figure 1.10. New poly-axial plate designs permit screws to be implanted at various angles giving the surgeon additional freedom when treating complex fractures.

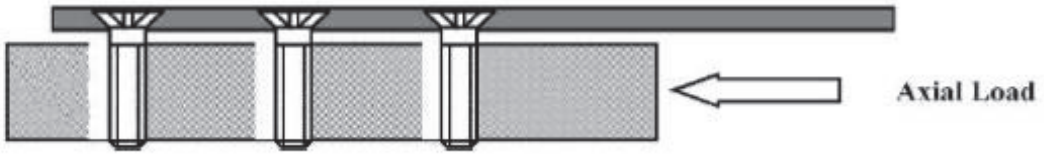

Figure 1.10: Engineering principles of locked plate designs (Egol et al., 2004)

An open reduction allows direction visualization of the fractured bone making an anatomical reduction easier to achieve. Volar locked plates provide excellent fixation

allowing earlier mobilization of the hand and wrist. This is advantageous to prevent joint stiffness and loss of function. However, the procedure is invasive and can be technically challenging for less experienced surgeons. Compared to conservative management and percutaneous pinning, procedural and implant costs are high particularly if a secondary intervention is required for implant removal. Figure 1.11 shows Stryker's volar locking plate system that is used to treat distal radius fractures.

Figure 1.11: Stryker's VariAx Distal Radius Locking Plate System (Stryker, Trauma)

1.2.6 Review of Clinical Literature Evaluating Existing Treatments

The literature on clinical outcomes associated with different methods of distal radius fracture treatment is extensive. Clinical and functional outcome measures commonly reported include: radiographic parameters (Figure 1.5 and Figure 1.6), range of motion, and grip strength. Subjective measures from patient questionnaires such as the Patient Rated Wrist Evaluation and Disabilities of the Arm Shoulder and Hand are also used to assess functional outcomes. Both questionnaires score patients based on questions regarding their ability to perform daily activities and their severity of pain and discomfort.

Existing treatment options have proven effective in managing distal radius fractures; however, as with any medical procedure there are potential risks of complication. A study conducted by McKay et al. (2001) evaluating the incidence of complications associated with treatment of distal radius fractures found a physician reported complication rate of 27%. The complications that were shown to have the highest rate of incidence include: carpal tunnel syndrome (22%), radial nerve damage

(11%), reflex sympathetic dystrophy (20%), and tendon irritation (14%). Conservative management has been used extensively in elderly patients to treat both stable and unstable fractures with good success. Anzarut et al. (2003) evaluated 74 patients over the age of 50 years treated with conservative management. The study found 64% of patients to have an acceptable radiographic reduction with a 59% patient satisfaction rate. Interestingly, no correlation was found between patient satisfaction and radiographic outcomes. A review of the literature conducted by Diaz-Garcia et al. (2011) supported this evidence by concluding that patients over the age of 60 years can have good functional outcomes despite poor radiographic alignment. Kilic et al. (2009) conducted a study evaluating the efficacy of conservative management for intra-articular fractures in elderly patients. A total of 29 patients were treated with an overall complication rate of 38%. The majority of complications (76%) involved a loss of reduction due to the unstable nature of the fractures and a high incidence of osteoporosis. Although conservative management is not ideal for unstable intra-articular fractures it can be used in elderly patients with moderate success to avoid the risks associated with surgery.

Board et al. (1999) showed improved radiographic and functional outcomes in elderly patients with intra-articular fractures when treated with percutaneous pinning in addition to cast immobilization. However, an additional complication linked to the use of percutaneous pins is pin track infection. Hargreaves et al. (2004) compared the rate of pin tract infection between percutaneous and buried wires and found infection rates to be 34% and 7%, respectively. The same risk exists when using external fixation, with one study reporting a 19% incidence of pin site infection (Egol et al., 2006). Percutaneous pins must be positioned carefully to avoid tendon and nerve damage. Singh et al. (2005) reported 20% of patients treated with percutaneous pins as having endured an injury to the sensory branch of the superficial radial nerve. Ludsvigsen et al. (1997) found a comparable rate of superficial radial nerve injury when using pin fixation.

Open reduction and internal fixation with volar locked plates has been used successfully, primarily to treat intra-articular fractures. A significant decrease in tendon damage has been witnessed with the adoption of volar plates when compared to traditional dorsal plates. Although the incidence of flexor tendon injury is low, Soong et al. (2011) demonstrated plate design and positioning may be important in minimizing

risk. Volar plates that are designed to be implanted more distally tend to lie with greater volar prominence increasing the risk of injury to the flexor tendons. Extensor tendon injuries can also occur when using volar plates as a result of dorsal screw prominence if screws are not implanted carefully. A study conducted by Knight et al. (2010) on patients treated with volar locked plates found a complication rate of 48%. The majority of complications were a result of screw penetration into the radio-carpal joint due to postoperative fracture collapse. Of these patients, 25% ended up with mal-unions and 12.5% experienced a ruptured extensor tendon.

A large number of prospective randomized trials have been conducted in an effort to compare the difference in outcomes between treatment options. Azzopardi et al. (2005) compared cast immobilization to cast immobilization supplemented with k-wires in elderly patients and found improved radiographic parameters at one year in the k-wire group. However, no difference in functional outcome was shown. When comparing bridging external fixation versus cast immobilization, Young et al. (2003) found patient satisfaction to be high in both groups and long terms outcomes were considered similar. Multiple studies evaluating external fixation versus percutaneous pinning have shown no difference in radiographic or functional outcomes as well as comparable complication rates (Harley et al., 2004; Ludvigsen et al., 1997). Mixed results have been shown when comparing non-bridging and bridging external fixators. McQueen (1998) found non-bridging fixators to be better at restoring carpal alignment. However, Krishan et al. (2003) compared the two types of external fixation and found no statistically significant differences in radiological or clinical outcomes. Provided the fractured fragment is large enough and pins are placed carefully to avoid tendon injury, non-bridging fixation is recommended. A number of studies comparing volar locked plating to percutaneous pinning with or without external fixation found improved functional outcomes in the volar locked plate group during early follow ups with similar results after one year (Egol et al., 2008; Jeudy et al., 2012; Kreder et al., 2005; McFadyen et al., 2011; Wilcke et al., 2011). Hence, volar locked plates are advantageous for early mobilization and resumed function of the hand and wrist.

In 2009, the American Association of Orthopaedic Surgeons (AAOS) performed an extensive review of the literature in an effort to provide recommendations for the

treatment of distal radius fractures. The results found a lack of reliable evidence to support an optimal treatment selection. Despite a lack of evidence favoring one treatment over another, multiple studies have reported a trend showing increased use of open reduction and internal fixation with volar locked plates. Chung et al. (2009) conducted a study evaluating treatment selection for elderly patients in the United States between the years of 1996 and 2005. The study reported an increase in the incidence of open reduction and internal fixation treatment from 3% in 1996 to 16% in 2005. Conservative management was found to be the most prevalent form of treatment; however, its use decreased from 82% in 1996 to 70% in 2005. Mattila et al. (2011) reported a similar trend for patient treatment in Finland. The number of surgical treatments more than doubled from 1998 to 2008 and the incidence of plate fixation increased from 2.3/100,000 person-years in 1998 to 30.9/100,000 person years in 2008. The most dramatic change in plate fixation incidence was found between 2006 and 2008, shortly after volar locked plating technology was introduced. Although there is no clear evidence showing improved outcomes with open reduction and internal fixation an obvious trend exists towards increased use. It has been suggested this is due to increasingly successful marketing schemes directed towards surgeons to adopt exciting new technologies (Nellans et al., 2012).

1.3 Testing and Validation of Novel Orthopaedic Devices

In recent years there has been a push for an improved evidence-based approach in bringing new orthopaedic devices to market (Schemitsch et al., 2010). Under the U.S. Food and Drug Administration's 510K pathway it is possible to receive regulatory approval of a new medical device by simply proving substantial equivalence to a predicate device. This means new devices can be marketed and implanted in patients without significant clinical evidence proving safety and efficacy. In 2008, at a meeting of the American Orthopaedic Association and Canadian Orthopaedic Association, 87% of surgeons believed that a standardized evidence-based approach for bringing new devices to market was a critical topic to explore (Schemitsch et al., 2010). Figure 1.12 shows a proposed pyramid for the development of novel orthopaedic implants beginning with preliminary laboratory tests and concluding with a pivotal randomized control trial.

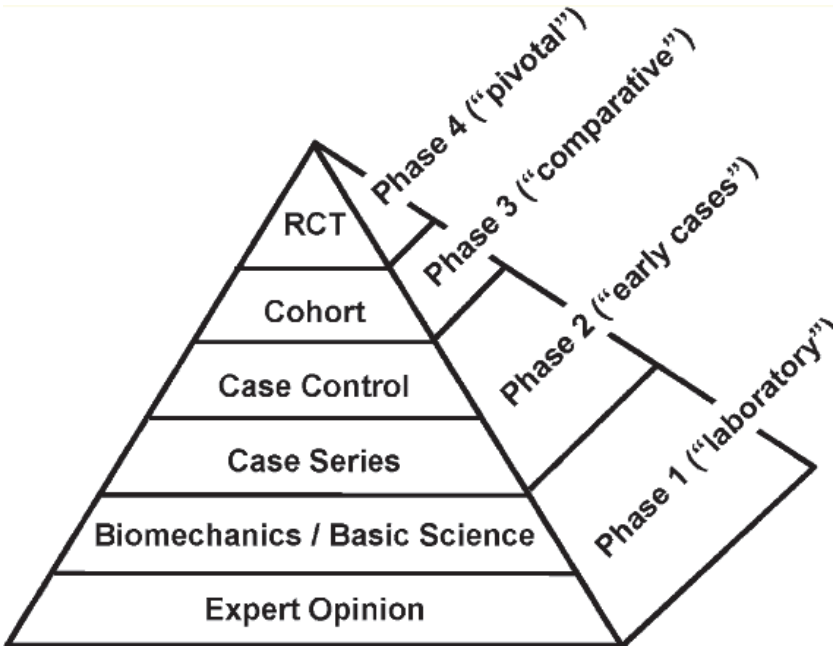

Figure 1.12: Proposed orthopaedic pyramid for an evidence-based approach of bringing new products to market. RCT = Randomized Control Trial (Schemitsch et al., 2010)

The implementation of the proposed evidence-based approach is likely to meet resistance due to the time, energy, and resources necessary to complete each phase. In addition, many orthopaedic implants require longitudinal follow-up studies upwards of 15-20 years to fully understand potential concerns. However, one aspect that remains consistent between current and proposed orthopaedic product development processes is the need to obtain relevant and repeatable pre-clinical data. Pre-clinical testing falls under Phase 1 of the proposed pyramid and is the focus of this thesis.

1.3.1 In vitro Experimental Testing

In vitro experimental testing is a common practice used to collect pre-clinical data of novel orthopaedic implants. The first biomechanical tests on human cadaveric long bones and orthopaedic implants date back over a century (Roesler, 1987). Physiological loading is a complex combination of anatomical geometry, material properties, muscle activity, and surrounding soft tissue. *In vitro* tests attempt to simplify this complex loading by isolating test specimens under axial compression, bending, and torsion loads. External loads are applied in an effort to replicate expected physiologic loads. Quasi-static loading can be easily implemented with experimental testing; however, cyclic and

impact loading are better representations of *in vivo* loads (Fulkerson et al., 2006; Mather, 1968). Cadaver specimens are often used as test mediums for experimental studies as they provide a 'true' representation of human bone. However, human bone quality is highly variable and the material properties of cadaver bone can be altered depending on preservation methods. A study analyzing differences between fresh-frozen and embalmed cadaver bone showed increased stiffness in the embalmed group (Comert et al., 2009). Challenges associated with cadaver work have led to increased use of synthetic bone materials for testing. Synthetic bones are advantageous as they do not require special storage, are readily available at a low cost, and provide a standard geometry with predetermined material properties (Papini et al., 2007). Synthetic bone materials continue to be improved and studies have validated their use as a human bone surrogate with good results (Cristofolini et al., 1996; Papini et al., 2007).

A number of outcome measures can be quantified during *in vitro* biomechanical tests. Some common measures used when assessing fracture fixation devices include stiffness, failure strength, strain, and stress. Stiffness is a measure of the force necessary to generate a unit of displacement. This can be calculated from the slope of the linear portion of a load versus displacement curve. Failure strength is another interesting measure used to evaluate a fracture fixation device and can be presented as either a mechanical or clinical value. Mechanical failure strength is defined as the force necessary to cause plastic deformation or permanent damage to the implant-bone construct. Clinical failure strength may be different, and is defined as the force necessary to cause a physiologically relevant maximum displacement. Strain is another measure that has two interpretations: IFS and mechanical strain. IFS quantifies motion at a fracture site relative to the original fracture gap width. Alternatively, mechanical strain refers to the change in unit length over the original length of a material. Mechanical strain and stress can be used to determine failure limits of an implantable device.

The purpose of *in vitro* experimental testing is to provide valuable pre-clinical information to the researcher and clinician. Experimental data can expose design flaws and highlight potential design improvements. Results are used to decide whether additional time, energy, and resources should be spent on clinical trials in live animals and/or humans.

1.3.2 Finite Element Analysis

Finite element analysis (FEA) is a computational technique used to numerically model stress/strain, heat transfer, computational fluid dynamics, and electromagnetism. FEA is used extensively in the aerospace and automotive industries as a tool to evaluate new designs and predict failure modes. Its value in the field of orthopaedic biomechanics include predicting the mechanical behavior of bone, evaluating new implant designs, and minimizing the time and cost associated with *in vitro* experimental testing. A finite element analysis is conducted in three general steps:

1. Model generation (geometry, meshing, material properties, boundary conditions and loading)
2. Processing (solving for nodal displacements)
3. Post-processing (solving for reaction forces, stresses, and strains)

FEA begins with the creation of a geometrical model considered to be representative of the problem at hand. This model is usually developed using computer-aided design (CAD) software. A finite element mesh is subsequently created and applied to the model. A finite element mesh refers to the discretization of a whole geometry into smaller elements. Each element in the mesh has a unique number and the end points, or vertices of the element are referred to as nodes. There are a number of different element types that can be used when creating a mesh. Element choices include; 1D structural, 2D truss, beam, frame, 2D quads, and 3D bricks (tetrahedral, hexahedral, or higher order). The accuracy of a finite element model depends on the number and type of elements chosen. Optimal element selection depends on the problem definition. In general, a selection is made based on a trade-off between accuracy and computational cost. 3D brick elements provide the best accuracy but at a much higher computational cost. Therefore, for simple problems where 1D or 2D elements give sufficient accuracy their use is recommended. Once a mesh has been created, material properties must be applied to each individual element. Material models differ in complexity and similarly to element selection a trade-off exists between accuracy and computational cost. Before calculations

can be made boundary conditions and loads must be applied to the model to define any nodal constraints and externally applied forces.

For stress and strain analysis, calculations are performed first by determining the displacement of each individual node in a finite element mesh. Nodal displacements can in turn be used to assume stress and strain distributions over corresponding elements. The fundamental finite element equation derived from the principle of strain energy that is used to solve for nodal displacements is:

$$[F] = [K] * [\Delta]$$

$$F \equiv \text{external force vector}$$

$$K \equiv \text{global stiffness matrix}$$

$$\Delta \equiv \text{nodal displacement vector}$$

The stiffness matrix [K] is calculated from the strain-displacement matrix [B], and the material properties of each individual element. The strain-displacement matrix is an interpolation of stress and strain values at various points along an element based on nodal displacements. For simple 1D and 2D problems in which strain-displacement is assumed to be linear over an entire element it is possible to solve for nodal displacements analytically. However, as the number of elements is increased these problems become increasingly difficult to solve and require the use of computational finite element code. As the complexity of a model increases, so do the computing costs required to solve the problem.

Once nodal displacements have been calculated, post-processing is performed to solve for strain [ε] and stress [σ] tensors. The strain and stress tensors are 3x3 matrices (Figure 1.13) that completely describe the three-dimensional strain and stress state at a specific element. In a state of equilibrium $\tau_{xy}=\tau_{yx}$, $\tau_{yz}=\tau_{zy}$, $\tau_{xz}=\tau_{zx}$ and $\gamma_{xy}=\gamma_{yx}$, $\gamma_{yz}=\gamma_{zy}$, $\gamma_{xz}=\gamma_{zx}$ allowing the tensor matrices to be expressed as vectors which helps to reduce computational cost.

$$[\varepsilon] = \begin{bmatrix} \varepsilon_{xx} & \gamma_{xy} & \gamma_{xz} \\ \gamma_{yx} & \varepsilon_{yy} & \gamma_{yz} \\ \gamma_{zx} & \gamma_{zy} & \varepsilon_{zz} \end{bmatrix}, [\varepsilon] = \begin{bmatrix} \varepsilon_{xx} \\ \varepsilon_{yy} \\ \varepsilon_{zz} \\ \gamma_{yz} \\ \gamma_{xz} \\ \gamma_{xy} \end{bmatrix} \quad [\sigma] = \begin{bmatrix} \sigma_{xx} & \tau_{xy} & \tau_{xz} \\ \tau_{yx} & \sigma_{yy} & \tau_{yz} \\ \tau_{zx} & \tau_{zy} & \sigma_{zz} \end{bmatrix}, [\sigma] = \begin{bmatrix} \sigma_{xx} \\ \sigma_{yy} \\ \sigma_{zz} \\ \tau_{yz} \\ \tau_{xz} \\ \tau_{xy} \end{bmatrix}$$

Figure 1.13: Strain and stress tensors

Strain and stress are calculated from the following equations:

$$[\varepsilon] = [B] * \left[\delta^{(e)}\right]$$

$$\left[\delta^{(e)}\right] \equiv \text{nodal displacements for element } 'e'$$

$$[\sigma] = [D] * [\varepsilon]$$

$$[D] \equiv \text{constitutive matrix}$$

The constitutive matrix in this equation describes properties of the material. If we recall Hooke's law for linear elastic materials we know stress is equivalent to the elastic modulus (E) of a material multiplied by strain. Therefore, for a 1D linear elastic problem the constitutive matrix would simply be equivalent to the elastic modulus of the material. If we extrapolate Hooke's law to a 3D linear elastic model the constitutive matrix becomes:

$$[D] = \frac{E}{(1+v)(1-2v)} \begin{bmatrix} 1-v & v & v & 0 & 0 & 0 \\ v & 1-v & v & 0 & 0 & 0 \\ v & v & 1-v & 0 & 0 & 0 \\ 0 & 0 & 0 & \frac{1}{2}-v & 0 & 0 \\ 0 & 0 & 0 & 0 & \frac{1}{2}-v & 0 \\ 0 & 0 & 0 & 0 & 0 & \frac{1}{2}-v \end{bmatrix}$$

$$v \equiv \text{poisson's ratio}$$

Through post-processing stress tensors are commonly represented as scalar non-directional stress invariants. One method is to report the three eigenvalues of the stress tensor, also known as the principal stresses (σ_1, σ_2, and σ_3). These principal stresses represent the three normal stresses perpendicular to the three planes of zero shear that

exist at a particular point on an object. Another stress invariant commonly reported is von Mises stress (σ_{VM}). Von Mises stress is a non-directional measure of stress state that combines shear, bending, and normal stresses. It can be calculated from the three principal stresses using the following equation:

$$\sigma_{VM} = \sqrt{\frac{1}{2}[(\sigma_1 - \sigma_2)^2 + (\sigma_2 - \sigma_3)^2 + (\sigma_1 - \sigma_3)^2]}$$

The majority of orthopaedic related finite element studies use either minimum principal stress or von Mises stress to assess failure. For this thesis, the von Mises yield criterion will be used as a surrogate measure of material failure. This criterion defines failure as a von Mises stress that exceeds the yield strength of the material.

1.3.2.1 Contact

For finite element models with multiple parts in contact, it is necessary to define contact surfaces. This requires the designation of a master and a slave surface. For one-way contact the stiffer of the two surfaces is generally defined as the master and the other as the slave. Most contact algorithms use the penalty method to check the slave nodes for penetration of the master segments. When a penetration is found a force proportional to the penetration depth is applied to resist and ultimately eliminate the penetration. Two way contact types, or surface to surface contact, perform an additional check of the master nodes for penetration of the slave segments. For this type of contact, definition of the master and slave surfaces is arbitrary. Defining a contact between surfaces allows compression loads to be transferred between the slave and master nodes. Tangential loads are also transmitted if relative sliding occurs when friction is active. The code used for this thesis employs a coulomb friction model that requires user defined coefficients of friction.

1.4 Review of Pre-Clinical Testing Literature

1.4.1 In vitro Experimental Testing Studies

Many *in vitro* biomechanical studies comparing different methods of distal radius fracture fixation have been reported in the literature. The majority of these have used cadaver models for analysis; however, more recent studies have shown synthetic bone models to be a good alternative for testing (Sobky et al., 2007). Of the studies reported in the literature, the most common type of distal radial fracture analyzed is an extra-articular dorsally comminuted fracture. Clinically, this is the most common fracture type, and experimentally can easily be replicated with a dorsal wedge osteotomy. Most studies have used axial loading configurations with torsion and bending loads used less frequently.

The introduction of volar locked plating triggered many biomechanical comparisons between dorsal and volar plate technology. Trease et al. (2005) performed a study evaluating the strength of locked versus non-locked dorsal and volar plates for treating extra-articular fractures. Embalmed cadavers were used for testing and the fracture was modeled as a 10 mm dorsal wedge centered 15 mm proximal from the radio-carpal joint surface. A quasi-static axial compressive load was applied at a rate of 1 mm/s until implant failure. The outcome measures were displayed on load versus displacement plots with implant stiffness defined as the slope of the linear portion. Failure strength was defined as the point of initial load reduction as shown on the plot. The results showed dorsal locked plates to have an axial stiffness of 1322 N/mm and failure strength of 988 N, compared to volar locked plates which had a stiffness and failure strength of 457 N/mm and 689 N, respectively.

Kandemir et al. (2008) conducted a similar study on fresh frozen cadavers in which a dorsal non locking plate was compared to a volar locking plate. In addition to quasi-static axial loading, specimens were also tested under cyclic axial and torsional loads believed to be more representative of physiologic loading patterns. To approximate physiological loads on the distal radius Putnam et al. (2000) created a cadaveric extrinsic force model to correlate grip force to the amount of force transmitted through the radius. The results showed that for 10 N of grip force, between 26 N and 52 N of force is

transmitted through the radius depending on hand positioning. Orbay et al. (2006) suggested it is common to allow patients to lift up to 5 lb of weight during early stages of rehabilitation from a distal radius fracture. Assuming a coefficient of friction equal to 1, lifting a 5 lb weight would translate to 25 lb of force on the radius, or approximately 110 N. Hence, Kandemir et al. applied cyclic compressive loads between 40 N and 100 N for 5000 cycles in an attempt to mimic physiological loads of the initial 6 week healing period. No statistically significant differences were found between dorsal plates and volar locked plates. Axial and torsional stiffness were found to be in the range of 200 N/mm and 230 N-mm/^{o}, respectively. Mean failure strength of the volar plates was 1238 N compared to 918 N for the dorsally plated specimens. The two aforementioned studies support the theory that embalmed cadavers have a greater stiffness than fresh frozen cadavers (Comert et al., 2009).

Additional biomechanical studies have been completed to compare different models of volar locked plates. Willis et al. (2006) were the first to use synthetic radii for biomechanical testing. Foam cortical shell sawbones (model #1027) were used and a dorsal wedge of bone was removed to model a fracture. Five different volar plate constructs were loaded under axial compression as well as volar and dorsal bending. Linear motion at the fracture site was measured in order to quantify axial and bending stiffness. One of the plate designs tested (DVR locking plate, Hand Innovations) has also been evaluated in subsequent experimental studies (Dahl et al., 2012; Sobky et al., 2007). Willis et al. found the DVR plate to have an axial stiffness in the range of 250 N/mm. Dahl et al. evaluated eight different volar locked plate designs using a similar synthetic bone model. However, 4th generation composite radii (model #3407) were used and cyclic axial loads reaching peaks of 100 N, 200 N, and 300 N were applied to each specimen. The stiffness of each group was found to increase with load and the axial stiffness of the DVR plate ranged from 175 N/mm to 275 N/mm. This result shows good comparison with the results found by Willis et al. In another similar study, Sobky et al. (2007) compared four volar locked plate constructs in both synthetic and cadaver radii. Foam cancellous core (model #1105) sawbones were used and a 10 mm gap was removed 20 mm proximal to the joint surface. Specimens were cycled axially up to 100 N and then loaded quasi-statically to failure. The axial stiffness of each plate including the DVR

plate was found to be in the range of 150-175 N/mm. Additional cadaver tests were conducted to validate the sawbone model and the results showed comparable modes of failure and failure loads. Based on these studies it is evident that synthetic bone models are a valid substitute to cadaveric testing. The results from these tests also support the clinical evidence that volar locked plates allow an early return to function.

Other biomechanical studies evaluating locked volar plates have compared screw quantity, type, and placement in an effort to help optimize the procedure (Drobetz et al., 2011; Martineau et al., 2008; Mehling et al., 2010; Weninger et al., 2010). A fewer number of studies have looked at the biomechanical stability of external fixation and percutaneous pinning of distal radius fractures. The only known biomechanical study comparing percutaneous pinning to volar locked plating found pin fixation to be significantly less stable than plate fixation (Knox et al., 2007).

1.4.2 Finite Element Studies

A number of finite element studies have been reported in the literature in regards to distal radius fractures. Many of these studies have analyzed the affects of bone quality on mechanical strength and fracture characteristics, with only a few evaluating the strength of existing fracture fixation devices. Multiple studies have combined high resolution imaging and micro FEA to measure the affects of bone quality on mechanical strength to better predict the risk of distal radius fractures (Arbenz et al., 2007; Boutroy et al., 2008; Varga et al., 2009). Anderson et al. (2005) performed an interesting study in which a finite element model was used to demonstrate how contact stresses in the radio-carpal joint change with respect to residual articular step-offs caused by intra-articular distal radius fractures. It was evident from this study that increased joint contact stresses are a contributing factor to post-traumatic osteoarthritis of the radio-carpal joint.

Of particular interest for this research project is the use of FEA to evaluate fracture fixation devices. Rogge et al. (2002) performed a 3D FEA of pin fixation of a distal radius fracture in an attempt to quantify fracture stability to determine an optimal pinning technique. This was the first finite element study to replicate the intricate 3D geometry of the radius. An accurate geometric model was obtained from a fine cut computed tomography (CT) scan of a fresh frozen human cadaver. Material properties of

the bone were derived from gray scale measurements taken from the CT images. The elastic modulus of each element was calculated by an empirical equation relating apparent density to elastic modulus (Carter and Hayes, 1977). An experiment was conducted to validate their model by loading the scanned cadaver specimen at 100 N and taking measurements from three strain gauges. The average difference between the numerical and experimental strain was calculated to be 7.1%. Pin configurations were modeled and interfacial frictional coefficients between the pin and cancellous and cortical bone were set to 0.3 and 0.5, respectively. These values were based on previous experimental work conducted by Rancourt et al. (1990). Results from the finite element model coincided with clinical knowledge demonstrating improved stability with pin fixation.

Similarly, Lin and Cheng both used FEA to investigate the biomechanical interactions of plate fixation angles using an internal double plating technique (Cheng et al., 2007; Lin et al., 2006). The same model was used in both studies and was created from CT scans a healthy male radius. Linear elastic, isotropic material properties were applied to the cortical (E=17 GPa) and cancellous (E=1.3 GPa) bone. Lin et al. analyzed different plating techniques, modeling plate separation angles of 50^{o}, 70^{o}, and 90^{o}. Displacements, stresses, and strains in the distal radius were measured under axial, bending, and torsional loading scenarios for all three models. It was determined that an increased angle between the plates provides greater mechanical strength and more favorable stress transmission. Compared to experimental testing, the use of FEA to evaluate distal radius fracture fixation devices has been minimal.

1.5 Thesis Objectives & Hypotheses

Objective 1

To design a novel implant and the associated surgical instrumentation to stabilize distal radius fractures using a minimally invasive surgical approach.

It is hypothesized that the novel treatment will be less costly and less invasive than open reduction and internal fixation, while providing sufficient stability to permit early mobilization of the hand and wrist, and that the surgical instrumentation will enable a less experienced surgeon to perform the procedure with relative ease.

Objective 2

To conduct *in vitro* experimental tests to quantify the stabilization strength of the novel implant. The two primary goals of the experimental analysis are to:

1. Determine if the mechanical fixation provided by the novel implant will result in IFS's conducive to bone healing in an extra-articular dorsally comminuted fracture model.
2. Compare the axial stiffness and failure strength of the novel implant to an existing percutaneous pinning treatment.

It is hypothesized that fixation with the novel implant will result in IFS less than 15% under simulated physiological loads. It is also hypothesized that the novel implant will show superior stiffness and failure strength compared to the existing percutaneous pinning treatment.

Objective 3

To recreate the experimental tests using FEA to obtain a valid model for further testing and future implant design optimization.

It is hypothesized that the finite element model will calculate axial stiffness of the implant within +/-10% of experimental values.

1.6 Structure of Thesis

This chapter of the thesis provides the necessary background to fully understand distal radius fractures and the lack of conclusive evidence supporting optimal treatment selection. It also highlights the importance of pre-clinical testing in bringing new orthopaedic devices to market and describes some of the techniques utilized to perform these tests. The following three chapters will describe the design and development of a novel treatment for distal radius fractures as well as the investigative tests used to evaluate the implant design. Each objective has been written as a standalone chapter detailing the methods used and the results obtained followed by a discussion. Chapter 2 addresses the first objective regarding the design and development of the novel treatment. Chapter 3 focuses on the *in vitro* experimental testing of the novel implant. Chapter 4 addresses the third and final objective of creating a valid finite element model. Finally, Chapter 5 summarizes the conclusions of the research and provides recommendations for future research on this project.

CHAPTER 2 DESIGN AND DEVELOPMENT OF A NOVEL TREATMENT APPROACH

2.1 Introduction

Distal radius fractures have the highest prevalence of any fracture and the number of incidents is expected to rise in the coming years (Court-Brown, 2006; Nellens et al, 2012). Despite a lack of clinical data to support a definitive treatment approach, recent reports have shown an increasing trend towards surgical intervention with internal fixation (Chung et al., 2009; Mattila et al., 2011). Internal fixation has been shown to provide improved short term results; however long term outcomes are similar to more conservative treatments. As a result of an increasing rate of incidence and a higher percentage of patients receiving internal fixation, associated health care costs are on the rise (Shauver et al., 2011; Shyamalan et al., 2009). A study performed in London found the procedural and implant cost of volar plate fixation to be greater than three times the cost of percutaneous pin fixation (Shyamalan et al., 2009). In the absence of clinical data showing internal fixation to provide superior long term outcomes, this increase in cost is considered significant. Shauver et al. (2011) reported that in 2007, Medicare made $170 million in payments related to distal radius fracture injuries. If the trend towards increased use of internal fixation continues it is projected that the future burden on Medicare will be upwards of $240 million annually. The high incidence and lack of definitive treatment presents a unique opportunity to explore alternative treatment methods.

There has been a recent surge in the health care industry towards the development of minimally invasive treatments. Treatment of distal radius fractures seems to be one of the few exceptions based on the trend showing increased use of internal fixation. In 2009, Dr. Michael Dunbar had the idea for a novel implant that could improve how distal radius fractures are managed. The idea was inspired by the plastic insert found in the collar of a men's dress shirt, and the imagination of implanting it into a radius and across a fracture. The proposed device could be implanted using a minimally invasive approach through the radial styloid. The simplicity of the implant design and the elimination of a secondary

intervention for implant removal would help reduce treatment costs. In addition, the device could potentially provide improved stability over existing minimally invasive treatments resulting in early outcomes more comparable to internal fixation. To improve implant fixation and fracture stability it was originally proposed that the novel implant exploit recent advancements in porous foamed metal technology. Porous foamed metals have become popular in the field of orthopaedics because of their advantageous properties for osseo-integration. Many implants are now being manufactured with a porous surface to permit bone growth within the pores of the surface creating a 'locked' connection. Titanium and tantalum are commonly used metals for orthopaedic implants because of their biocompatible nature. It was believed if the novel implant was machined from a porous metal, improved fixation during early stages of bone healing would support early mobilization of the hand and wrist.

In selecting the optimum technique for treating distal radius fractures, the surgical complexity, mechanical performance, and biological response should all be considered. Technically, the method is ideally simple and inexpensive. Mechanically, the fixation should provide sufficient stability to allow gentle use of the hand. Biologically, the treatment should be minimally invasive, the implants well tolerated, and the resulting bone stresses optimal for fracture healing (Aro and Chao, 1993). The proposed treatment is poised to meet each of these requirements while addressing limitations of existing treatment methods. This chapter will outline the validation of the treatment approach as well as the design and development process of the implant and associated surgical instrumentation.

2.1.1 Surgical Approach

The novel treatment is made possible through a surgical point of entry at the radial styloid. A small incision will be made and the radial styloid will be exposed by blunt dissection. The implant will be positioned carefully to avoid damage to the superficial branch of the radial nerve and the first and third extensor tendons. The surgical approach is shown in Figure 2.1.

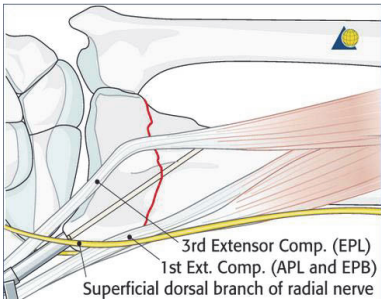

Figure 2.1: Surgical approach through radial styloid (AO, Foundation)

2.2 Methods

2.2.1 Validation of Treatment Approach

The first phase of the design and development process was a proof of concept test to validate the novel treatment approach. Prior to any testing, implant prototypes were fabricated. The original implant design was a 90^{o} angled bar with a sharp cutting edge machined into one end. The cutting edge was included to enable penetration of the implant through the bone. Three versions of the prototype were prepared for preliminary testing: one made from steel, one made from porous tantalum, and one made from porous titanium (Figure 2.2). The steel prototype was machined locally and the porous metal prototypes were supplied by industry partners, Zimmer (tantalum) and Stryker (titanium). In addition to the implants, essential surgical instruments were prototyped to facilitate the procedure. This included a hand held device to support the implants while being driven into the bone. The proof of concept test was also used to gather valuable information on the requirements of the surgical instrumentation to make the procedure possible and easy to perform.

Figure 2.2: Implant prototypes (top: steel, middle: porous tantalum, bottom: porous titanium)

Testing was conducted on cadaver radii by an experienced orthopaedic surgeon. Prior to testing, ethics approval was obtained from the Capital Health Research Ethics Board. All cadaveric testing was performed at the Skills Centre for Health Sciences. The Skills Centre is a joint initiative between Capital Health, the IWK Health Centre, and Dalhousie University. It is designed to practice surgical techniques in a simulated clinical environment. An x-ray technician was present at the time of testing to provide real time radiographic imaging using a c-arm fluoroscopy unit. Distal radius fractures were simulated with a dorsal osteotomy approximately 20 mm proximal to the radio-carpal

joint. Radii were exposed using a dorsal approach and an oscillating bone saw was used to create the fracture. An effort was made to minimize soft tissue disruption. After the fracture was created a small lateral incision was made and the radial styloid was exposed through blunt dissection. Traction was applied manually on the wrist to aid in a closed reduction. Once an acceptable anatomical reduction was confirmed through radiographic imaging, three separate attempts were made to implant each of the prototypes. Fluoroscopic guidance was used to track implant position throughout the procedure. K-wires were used as necessary to provide additional fracture stability during implantation.

The cadaver test provided valuable insight regarding necessary design criterion for the implant and surgical instrumentation to optimize the procedure. The design criteria for the implant and instrumentation are outlined in the subsequent sections.

2.2.2 Implant Design Criteria

The implantable device is the primary component of the proposed novel treatment. In order to guide the development process a set of criteria was defined for the implant to meet. The criterion was selected to ensure an effective design that adheres to the regulatory requirements for implantable medical devices. The following list of criteria was used for implant design selection:

1. Sterile:

   Sterilization is a process that completely eliminates all living micro-organisms. Implantable medical devices are required by law to be sterile prior to entering the body. It is necessary that the novel implant be manufactured from a material that can be easily sterilized.

2. Biocompatible:

   Biocompatibility of an implantable device is defined as the ability of that implant to perform its intended function, with the desired degree of incorporation in the host, without eliciting any undesirable local or systemic effects in that host (Williams, 2003). Medical device regulations require that

the novel implant be biocompatible with the native tissue of the human body.

3. Sufficient Mechanical Fixation:
   The efficacy of the implant is dependent on its ability to adequately stabilize a fracture. The mechanical fixation provided by the implant should be able to withstand physiological loads and support new bone formation. Therefore, structural stiffness must be considered when selecting an implant design. Mechanical fixation of the selected design will be quantified through experimental and numerical evaluation.

4. Sized anatomically:
   The size of the implant is constrained by the anatomical geometry of a radius bone. The implant must be long enough to bridge a fracture while minimizing implant exposure to the surrounding soft tissue. Also, the size of the implant should be able to accommodate the variability in bone geometry between patients. A trade-off exists between implant size and structural stiffness.

5. Easy to implant:
   The device should be easily implantable into human bone. A surgeon should be able to position the implant in a controlled manner, minimizing damage to the intact bone.

6. Low cost:
   Reducing healthcare costs is an important factor in developing an improved treatment option. The implant should be designed so that manufacturing costs are minimized.

Considering the aforementioned design criterion a number of implant designs were generated. Design ideas were modeled using Solid Edge CAD software to help

conceptualize various ideas. For further visualization of design concepts, prototypes were constructed using an additive manufacturing process. Finally, a Pugh Concept Selection Matrix was used to choose an implant design. A Pugh Concept Selection Matrix is a decision matrix that scores different design concepts against a set of design criterion. An existing design is chosen as the datum and all other designs are scored relative to it. Scores for each concept are defined as being better than ("+"), about the same ("s"), or worse than the datum ("-"). Total scores are tabulated for each concept and the concepts are ranked based on the results. The concept with the highest positive score is the one considered to be the best design. For scoring the implant designs, stainless steel k-wires were selected as the reference datum.

2.2.3 Surgical Instrumentation Design Criteria

The surgical instrumentation is a secondary component of the proposed novel treatment. The goal was to develop surgical tools to enable a less experienced surgeon to perform the procedure with relative ease. The following set of criteria was created to define the general requirements of the surgical instrumentation:

1. Sterile:

   Any instrumentation that enters the sterile field of the operating room must be sterile. Following the surgical procedure the instrumentation must be re-sterilized or disposable.

2. Method of holding the implant:

   The instrumentation must be able to hold the implant while it is implanted into the bone. A single surgeon should feel confident in their ability to control the implant during implantation.

3. Ability to apply traction:

   The instrumentation should be able to apply traction on the patient's wrist in various directions depending on the fracture type. Once traction has been applied it should be maintained throughout the procedure.

4. Ability to secure the patient's arm:

   The patient's arm should be restrained to limit unwanted movements during the procedure.

5. Ability to obtain AP and lateral radiographic images:

   The surgeon should have the ability to obtain AP and lateral radiographs throughout the procedure. This will allow closed reduction and implant position to be monitored in multiple planes of view.

6. Method of guiding the implant:

   The instrumentation should make it easy for the surgeon to correctly position the implant across a fracture.

Based on these requirements a flowchart was created to show the necessary components and the relationship between them in order to make the novel procedure a success (Figure 2.3).

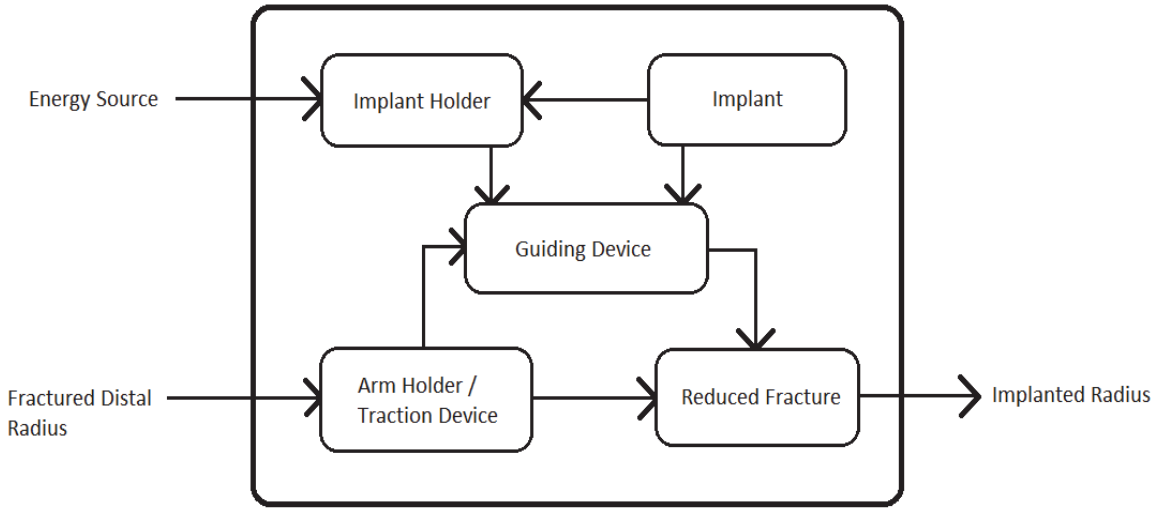

Figure 2.3: Flowchart showing the components of the novel treatment.

Inputs: Energy source and fractured distal radius.
Energy source refers to the energy required to drive the implant into the bone. Possible sources include a manual hammer, electric hammer, and pneumatic impactor.
Outputs: Implanted radius.

The surgical instrumentation deemed to be necessary for the procedure included an implant holder, a traction device, and a method of guiding the implant. The implant holder was designed using an iterative approach in which ideas were modeled, prototyped, and tested until a final design was selected. For the traction device, design requirements were divided into sub-components to simplify the selection process. The sub-components included methods of incorporating the device into the current surgical environment, methods of applying traction, methods of securing the patient's arm, and methods of rotating the patient's arm to obtain AP and lateral radiographs. Multiple ideas were considered for each sub-component and concepts were compared using a decision-matrix. In the absence of a true datum, concepts were scored as below average ("0"), average ("1"), or above average ("2") against specific requirements of each sub-component. A weighted scoring factor was used to magnify the most important requirements and overall weighted scores were used to select the optimal concept for each sub-component. A method for guiding the implant across a fracture was chosen that could easily be implemented with the selected implant, implant holder, and traction device designs.

2.3 Results

2.3.1 Validation of Treatment Approach

The cadaver study was considered a success in two facets. First, it confirmed that a device can be implanted into the radius through the radial styloid, validating the treatment approach. Second, the cadaver test provided valuable insight in regards to optimal implant and surgical instrumentation designs.

A fracture was successfully modeled in the cadaver radius, and attempts were made to implant each of the three prototypes. Additional attempts were made to implant the prototypes into an intact radius to assess the ease of penetration through bone. It was evident from the tests that the porous foamed metal prototypes could not easily be implanted. Due to the size constraints on the implant and the inherently weak mechanical properties of porous constructs, the porous foamed metals showed a tendency to buckle during implantation. This mode of failure is shown in Figure 2.4. However, the implant caused no visual signs of damage to the bone, which was an encouraging result.

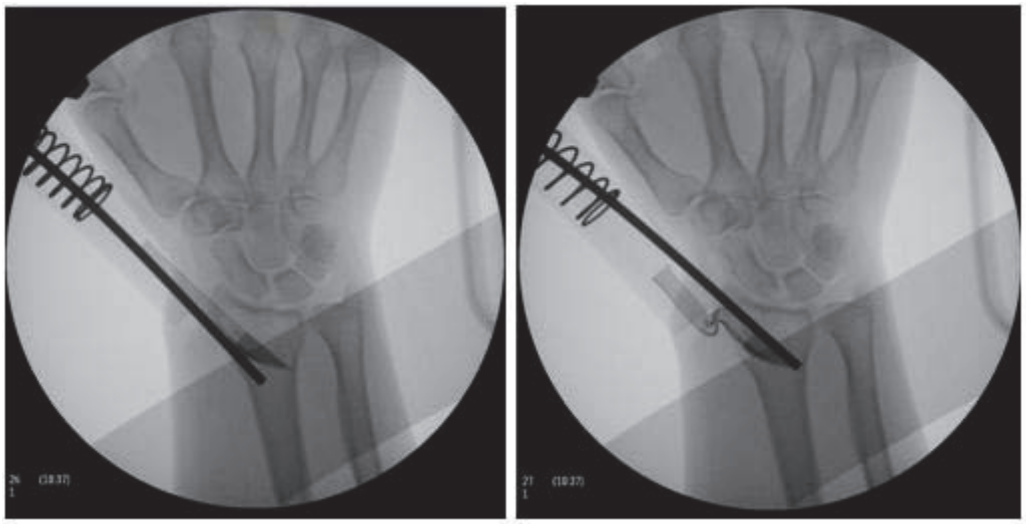

Figure 2.4: Radiographic images of porous titanium implant failure in buckling

The steel prototype was implanted into the radius with far more success than the porous metals, showing no difficulties in penetrating through bone. Figure 2.5 shows radiographic images of the implanted steel prototype. It was evident from the radiographs that the current version of the implant was too large for the geometry of the radius. However, with the increased strength of a solid metal, reducing the size of the implant was considered to be feasible. A qualitative assessment of fracture stability with the steel implant demonstrated good fixation indicating that improved osseo-integration achieved with porous foamed metals may not be necessary.

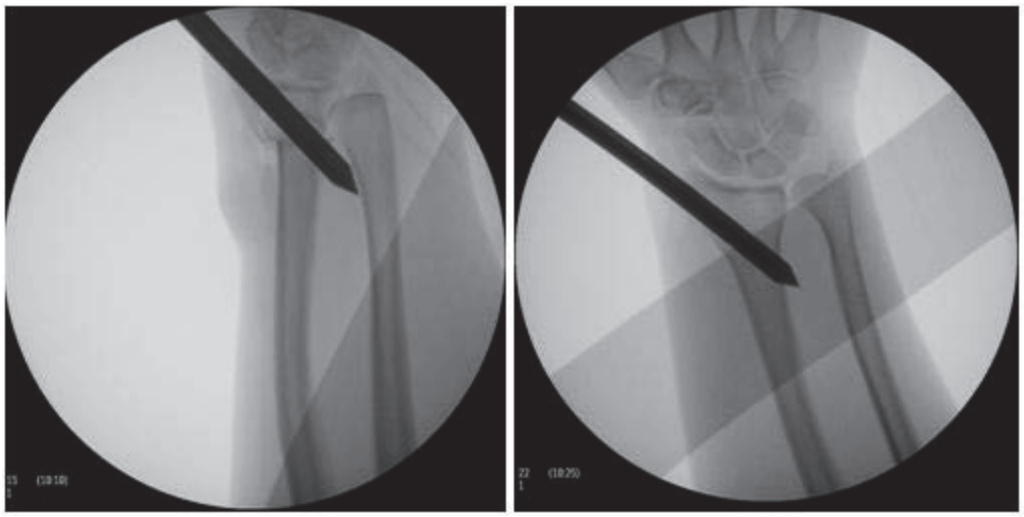

Figure 2.5: Radiographic images of steel implant positioned within cadaver radius

2.3.2 Implant Design Selection

Implant design selection was divided into two steps: selection of the implant shape and selection of the implant material. Four design concepts were modeled and considered for the implant shape. The concepts considered included an angled implant with a sharp cutting edge, a similar design with the inclusion of a central canal, a curved profile with a sharp cutting edge, and an angled implant with no cutting edge. Angled and curved profiles were chosen for improved bending stiffness compared to a thin rectangular profile. CAD models of the implant concepts are shown in Figure 2.6. The inclusion of a central canal in the second design is to allow the implant to travel over a k-wire to guide positioning. The design without a cutting edge would require an additional step in the surgical procedure to chisel a slot for the implant.

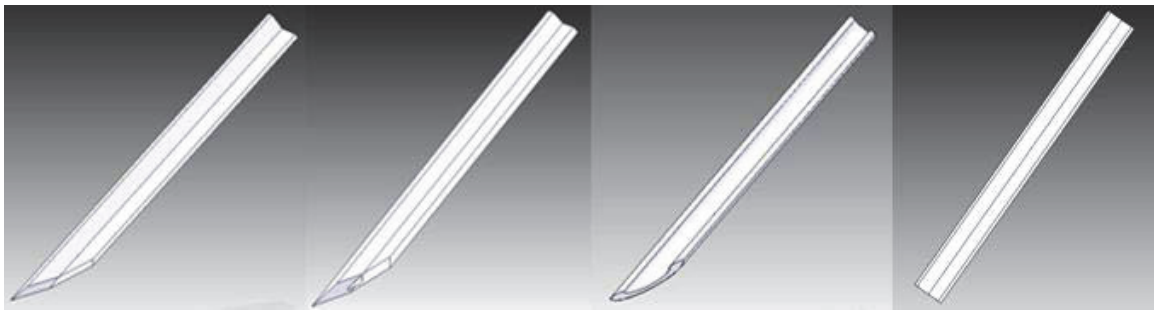

Figure 2.6: CAD models of implant design concepts
From left to right: angled profile with cutting edge, angled profile with cutting edge and canal, rounded profile with cutting edge, angled profile with no cutting edge.

Based on the results from the Pugh concept selection matrix shown in Table 2.1, the angled design with the sharp cutting edge was selected. This design was selected primarily because it is the easiest to machine and implant. The design with a central canal was carefully considered; however, it was determined that the addition of the canal increased the thickness of the implant beyond the size constraints of a radius bone.

Materials that were considered for manufacturing the implants included Stainless Steel 316L, Ti-4Al-6V Titanium Alloy, Porous Titanium, and Porous Tantalum. The Pugh concept selection matrix for implant material selection is shown in Table 2.2. It was decided that Stainless Steel 316L would be optimal. The cadaver test played an important role in the decision to select a solid metal alloy. Stainless steel 316L is often used for orthopaedic implants and could be machined at a lower cost than titanium alloys.

Table 2.1: Pugh concept selection matrix for implant shape selection ("-" = worse than datum, S = same as datum, "+" = better than datum)

Pugh Concept Selection Matrix Comparison Criteria	SS Percutaneous Pins (Datum)	**Angled with cutting tip**	Angled and cannulated	Rounded with cutting tip	Angled without cutting tip
Ease of machining		**S**	-	-	S
Mechanical strength		**+**	+	+	+
Ease of implantation		**S**	-	S	-
Anatomical size		**S**	-	S	S
Implant positioning control		**S**	+	S	S
Total +'s		**1**	2	1	1
Total -'s		**0**	3	1	1
Total Score		**1**	-1	0	0
Rank		**1**	3	2	2

Table 2.2: Pugh concept selection matrix for implant material selection ("-" = worse than datum, S = same as datum, "+" = better than datum)

Pugh Concept Selection Matrix Comparison Criteria	SS Percutaneous Pins (Datum)	**Stainless Steel 316L**	Titanium Alloy Ti-4Al-6V	Porous Titanium	Porous Tantalum
Cost of material		**S**	-	-	-
Ease of machining		**S**	-	-	-
Mechanical Strength		**S**	S	-	-
Ease of implantation		**S**	S	-	-
Osseo-integration properties		**S**	S	+	+
Biocompatibility		**S**	+	+	+
Total +'s		**0**	1	2	2
Total -'s		**0**	2	4	4
Total Score		**0**	-1	-2	-2
Rank		**1**	2	3	3

The sharp cutting edge of the implant was designed with an offset to allow easier penetration through the bone. The goal for positioning the implant is to penetrate through the radial styloid, across a fracture, and to perforate the medial cortex of the radius. The outer layer of cortical bone has a higher density than the inner cancellous bone. Therefore, having both ends of the implant fixed in cortical bone will maximize the fracture fixation strength. The offset design allows the implant to lead with the sharp tip when it enters the bone, bridges the fracture, and reaches the medial cortex. This will allow a bi-cortical fixation to be achieved as shown in Figure 2.7.

Figure 2.7: Implant positioned with a bi-cortical fixation

2.3.3 Surgical Instrumentation Design Selection

The final design for the implant holder was selected using an iterative approach. The initial design concept was a hand held device with a v-shaped slot for holding the implant. The depth of the slot was constrained to 5 mm, providing just enough support for the implant without significantly limiting the extent of penetration into the bone. The proximal end of the implant holder was designed to mate with an electric hammer used to facilitate implantation. The distal end was designed with a taper to avoid interference with the carpal and metacarpal bones of the hand. Through prototyping and testing of various concepts a number of design improvements became apparent. The initial and final designs of the implant holder are shown in Figure 2.8.

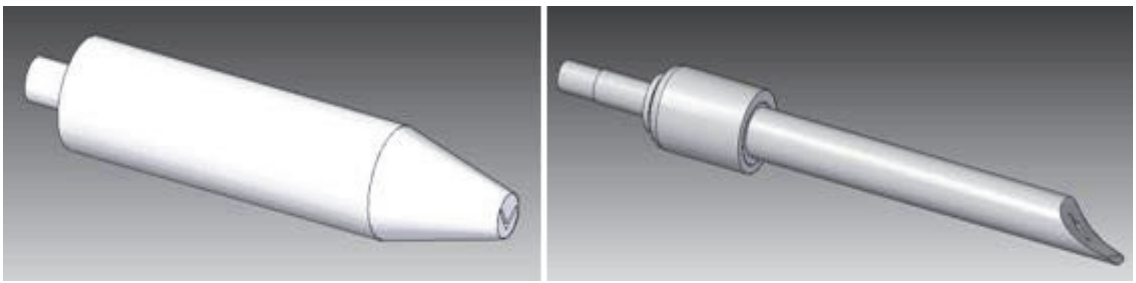

Figure 2.8: CAD model of inital (left) and final (right) iterations of implant holder design

The most significant improvement to the implant holder design was the added ability to countersink an implant below the level of soft tissue and flush with the bone. The ability to position the implant flush with the bone will mitigate risk of soft tissue irritation. The final implant holder design is comprised of three parts: an implant chamber, a pusher-piston, and a threaded cap with a built in linear bearing. The implant chamber is a slotted cylinder designed to fully enclose the implant prior to insertion into the bone. Full enclosure is intended to provide additional implant support and control during implantation. The pusher-piston consists of a cylindrical pusher rod with a piston shaped to mate with the v-shaped slot in the implant chamber. The pusher rod drives the piston through the implant chamber forcing the implant into the bone. The stroke length of the pusher-piston was designed such that the implant can be positioned flush with the bone. The threaded cap is used to connect the pusher-piston and implant chamber and allows for easy disassembly for re-sterilization of the device. The inclusion of a linear bearing generates a more fluid motion of the pusher rod. Figure 2.9 demonstrates the initial and final positions of the implant within the implant holder. Another useful feature of the final design is the curved profile of the distal face on the implant chamber. This curved profile matchs the geometry of the radial styloid enabling the surgeon to position the implant holder directly against the bone. The mating geometry provides additional control when attempting to position and insert the implant.

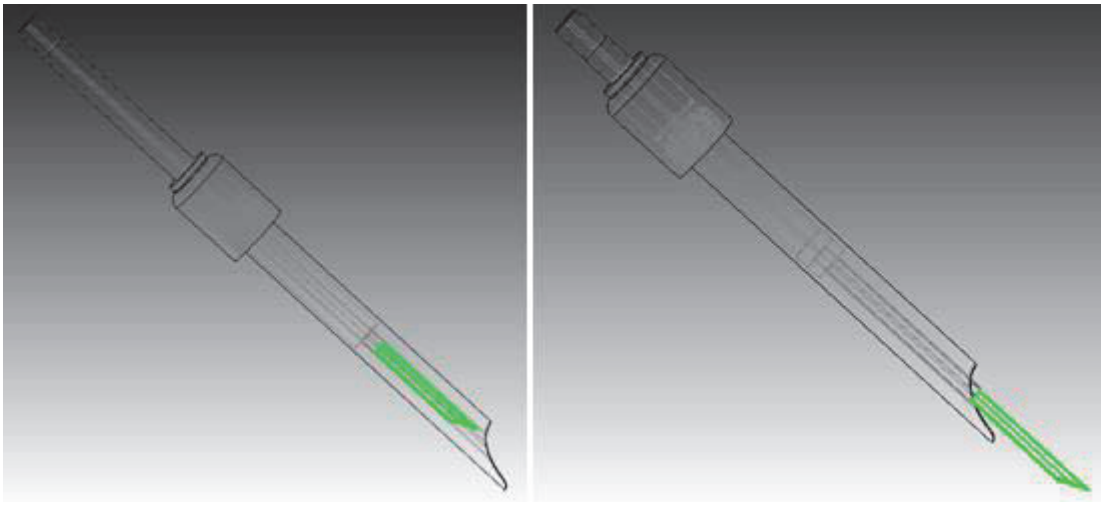

Figure 2.9: CAD model showing the initial (left) and final (right) positions of the implant (green) within the implant holder

The design of the implant holder was also influenced by the method selected for guiding the implant into the correct position. It was determined that the easiest approach to maintaining an anatomical reduction and correctly positioning the implant was to first stabilize the fracture with a single k-wire. Implanting k-wires is common surgical practice and can be done with relative ease. Therefore, it was decided that to position the implant the presence of a previously positioned k-wire would be utilized as a guide. The angular shape of the implant is advantageous for this approach as the inner vertex of the implant can easily travel over top of a cylindrical k-wire. To facilitate this approach a central canal was added to the implant holder extending through the implant chamber and pusher-piston. The concept of positioning the implant utilizing a k-wire as a guide is shown in Figure 2.10. The depth of penetration of the k-wire can also be used as a measuring tool for choosing a suitable implant length for each individual patient.

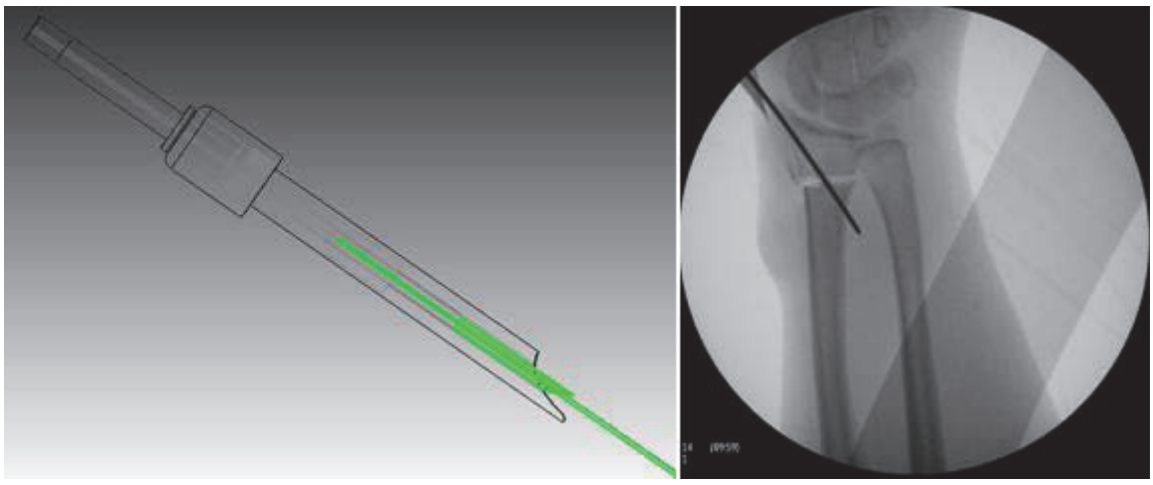

Figure 2.10: CAD model and radiographic image of implant being guided over top of a k-wire

For selection of the final traction device design, three concepts were considered for each sub-component of the assembly. The three concepts considered for incorporating the device into the current surgical environment were a device that clamps to existing surgical arm boards, a standalone device that can be positioned beside an operating table, and a device that clamps to the top of fluoroscopic c-arm detectors. The concepts considered for applying traction included finger traps connected to counter weights, finger traps connected to a ratcheting tray, and finger traps connect to a hand winch. For

securing the patients arm the three concepts considered were a vertical motion clamping bar, a velcro strap, and strap with an adjustable buckle. Finally, for rotating the patient's arm to obtain AP and lateral radiographic images the concepts considered were to rotate the entire traction device, to rotate the component securing the patient's arm, and to rotate the finger traps to subsequently rotate the patient's wrist. The decision selection matrix that was used to choose the optimal concept for each sub-component is shown in Table 2.3. The concepts with the highest scores based on the outlined design criteria are highlighted in bold font.

Table 2.3: Decision selection matrix for traction device design selection
Scoring: 0 = below average, 1 = average, 2 = above average

ARM HOLDER/TRACTION DEVICE DESIGN SELECTION MATRIX							
CRITERIA FOR EACH SUB-COMPONENT OF ASSEMBLY		**DESIGN CONCEPTS**					
Method of incorporation into surgical environment		Clamp over top of existing arm board		Portable stand alone assembly		**Rest on top of c-arm detector**	
Design Criteria	***Weight***	*Score*	*Weighted Score*	*Score*	*Weighted Score*	***Score***	***Weighted Score***
Ease of setup	1	0	0	1	1	**1**	**1**
Simplicity and user friendliness	4	1	4	1	4	**2**	**8**
Ease of sterilization	3	1	3	0	0	**1**	**3**
Compatibility with various OR's	2	1	2	2	4	**1**	**2**
Total Score			9		9		**14**
Rank			**2**		**2**		**1**

		DESIGN CONCEPTS					
Method of applying traction		Finger traps connected to counter weights		**Finger traps connected to sliding ratcheting tray**		Finger traps connected to hand winch	
Design Criteria	***Weight***	*Score*	*Weighted Score*	***Score***	***Weighted Score***	*Score*	*Weighted Score*
Ease of angle and height adjustment	2	1	2	**1**	**2**	0	0
Ease of sterilization	3	2	6	**1**	**3**	0	0
No interference with x-ray imaging	1	1	1	**1**	**1**	1	1
Incremental tension control	4	1	4	**2**	**8**	1	4
Total Score			13		**14**		5
Rank			2		**1**		3

		DESIGN CONCEPTS					
Method of securing arm		Vertical motion clamping bar		**Velcro strap**		**Strap with adjustable buckle**	
Design Criteria	***Weight***	*Score*	*Weighted Score*	***Score***	***Weighted Score***	***Score***	***Weighted Score***
Ease of sterilization or disposable use	1	0	0	**1**	**1**	**1**	**1**
Adjustable to various sized arms	3	1	3	**2**	**6**	**2**	**6**
Ability to securely fasten patient's arm	4	1	4	**1**	**4**	**1**	**4**
Ability to withstand implantation forces	2	1	2	**1**	**2**	**1**	**2**
Total Score			9		**13**		**13**
Rank			3		**1**		**1**

		DESIGN CONCEPTS					
Method of arm rotation		Rotate the entire assembly		Rotate the component securing the arm		**Rotate finger traps in order to rotate the wrist**	
Design Criteria	***Weight***	*Score*	*Weighted Score*	*Score*	*Weighted Score*	***Score***	***Weighted Score***
Ability to control rotation of the wrist	3	2	6	2	6	**1**	**3**
Ability to maintain anatomical reduction	4	2	8	0	0	**2**	**8**
Quick and easy rotation of the wrist	2	0	0	1	2	**2**	**4**
Ability to lock in AP and lateral positions	1	2	2	1	1	**2**	**2**
Total Score			16		9		**17**
Rank			2		3		**1**

The final traction device design is intended to clamp over top of a fluoroscopic c-arm detector. C-arms are currently used during the surgical treatment of distal radius fractures to obtain radiographic images for guiding reduction and implant positioning. The ability for the surgeon to operate directly on the c-arm simplifies the procedure by eliminating the need for a surgical arm board. The patient's arm is positioned on the traction device in the supine or prone position depending on the desired direction of traction. The supine position is recommended for flexed traction and the prone position is recommended for extended traction. The arm is secured to the device with a strap, and the ulnar side of the arm rests against a support. The arm support resists motion during implantation and also acts as a fulcrum when applying ulnar deviated traction. The patient's fingers are connected to finger traps and the direction of traction is controlled through height and angular adjustments. Once the finger traps have been positioned, traction is applied through extension of the ratcheting tray. The ratcheting tray slides on a

set of rollers and spring loaded latches lock in the traction at incremental intervals. A supplemental fine traction adjustment knob can be used to apply minor traction adjustments as desired. A CAD drawing of the traction device with the main sub-components highlighted is shown in Figure 2.11.

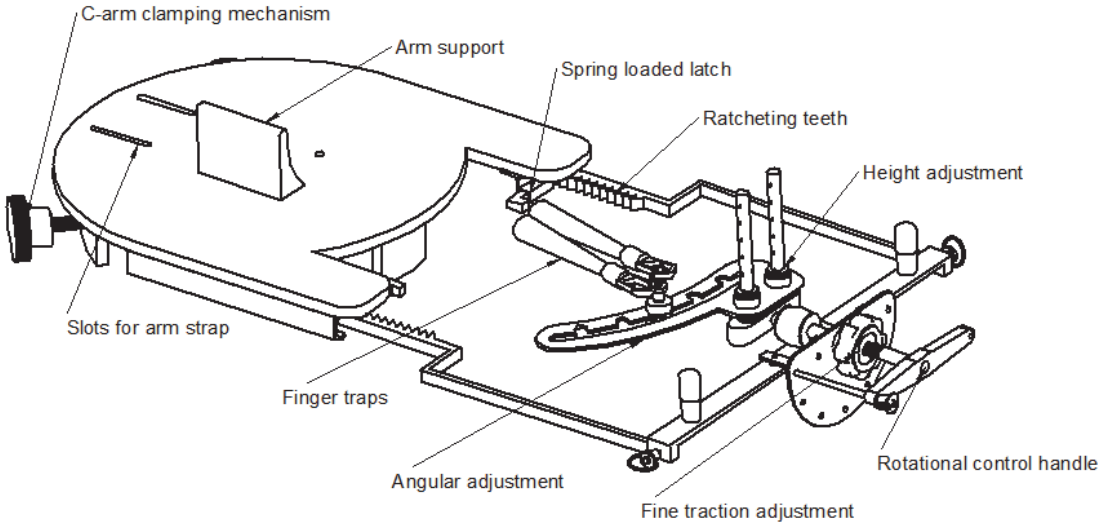

Figure 2.11: CAD drawing of traction device highlighting main sub-components

For AP and lateral radiographic imaging, the traction device has the ability to rotate. The rotational control handle rotates the finger traps as well as the height and angular adjustments (Figure 2.12). By nesting the height and angular adjustments within the rotation, the desired direction of traction is maintained throughout the rotary motion. With tension applied on the fingers and the proximal arm secured, rotation of the finger traps translates to rotation of the wrist permitting imaging in multiple planes.

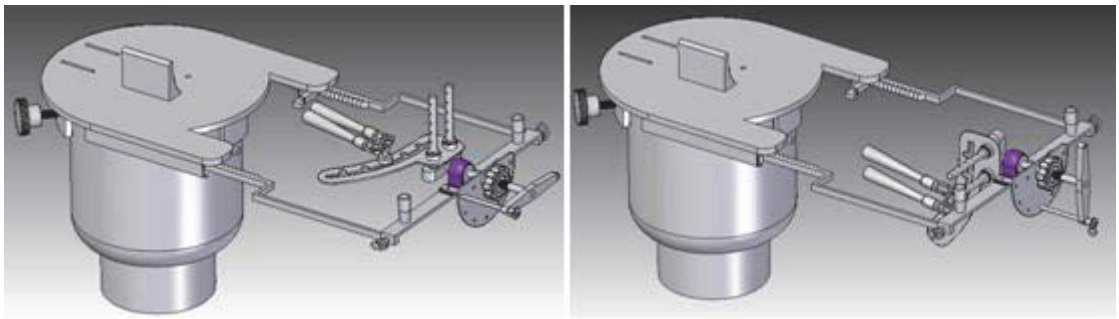

Figure 2.12: CAD model of traction device on c-arm detector at 0^{o} (left) and 90^{o} (right) positions

2.4 Discussion

The cadaver study successfully validated the novel treatment approach and provided valuable insight for optimization of the implant and instrumentation designs. On December 19, 2011, a PCT application was filed to protect the intellectual property of the aforementioned designs. In addition to the novel implant and treatment approach, the traction device is also a unique design. It is recommended that operating on the surface of a c-arm be rigorously tested prior to implementing this design to ensure no damage is inflicted on the fluoroscopy unit.

The use of porous foamed metals was not supported by preliminary validation testing. The porous metal implants buckled under the forces required to drive the implant into bone. It is believed that improvements made to the implant holder design may help minimize the likelihood of implant buckling by fully enclosing the implant throughout the procedure. However, a qualitative assessment of the steel implant fixation strength supported the use of a solid metal. Therefore, a stainless steel implant design was selected for early stage pre-clinical testing. Possible future iterations to the implant design may include the use of a porous surface and the addition of osseo-inductive carriers such as platelet derived growth factors and bone morphogenetic proteins.

The implant and surgical instrumentation were designed to meet the suggested requirements of an ideal treatment for distal radius fractures. The simplicity of the implant design and re-usable surgical instrumentation will help minimize associated hardware costs. The surgical instrumentation should help to reduce operating time and hence, reduce procedural costs. The elimination of a secondary intervention for implant removal will also minimize additional expenses. If the mechanical fixation provided by the novel implant can support physiological loads in a manner that is conducive to bone healing, the proposed treatment will provide a low cost, minimally invasive alternative to internal fixation while still enabling an early return to function.

2.4.1 Conclusion

In conclusion, cadaver testing was used to successfully validate the novel treatment approach. A novel implant was designed that consists of an angular profile with a sharp cutting edge to permit penetration through the bone and fixation into the medial cortex of the radius. An implant holder was created to facilitate accurate positioning of the implant over top of a previously placed k-wire. Finally, a novel traction device was designed to assist surgeons in performing a closed reduction while operating on the detector surface of a c-arm fluoroscopy unit. Pre-clinical testing is required to assess the mechanical fixation strength of the novel implant design.

CHAPTER 3 IN VITRO EXPERIMENTAL INVESTIGATION OF THE NOVEL IMPLANT

3.1 Introduction

Pre-clinical testing of novel orthopaedic implants is an important phase during the early stages of new product development. Pre-clinical data provides valuable evidence on the efficacy of a novel implant and helps determine if additional resources should be exhausted on subsequent phases of the development process. To assess the efficacy of the novel implant presented in Chapter 2, *in vitro* experimental tests were conducted.

The novel implant is optimized to treat extra-articular dorsally comminuted fractures. This type of fracture is commonly seen as a result of low energy traumas in elderly patients and has been shown to account for roughly 70% of all distal radius fractures (Brogren et al., 2007; Flinkkila et al., 2010). These fractures are frequently displaced due to dorsal bone comminution and typically require some degree of fixation to maintain an anatomical reduction. Conservative management is often supplemented with k-wires or external fixation to help stabilize a fracture. However, there has been a recent trend showing increased use of internal fixation with volar locked plates to treat these fractures (Chung et al., 2009; Mattila et al., 2011). Volar locked plates are known to provide an earlier return to function, but at a much higher cost. The novel implant is intended to be a low cost, minimally invasive alternative to volar locked plates. The strength of the implant is not expected to be equivalent to volar locked plates. However, improved stability over k-wire fixation would indicate that an earlier return to function may be possible.

In vivo forces transferred through the radius are the result of a complex combination of axial, bending, and torsion loads. For simplicity, only axial compressive loads were considered for *in vitro* testing. A number of extrinsic muscles span the radio-carpal joint and actively control the hand. Contraction of these muscles can transfer significant compression forces from the carpal bones to the radial joint surface. Putnam et al. (2000) found that for every 10 N of grip force, between 26 N and 52 N of force is transmitted through the radius. The magnitude of this force depends on positioning of the

hand. It has been suggested that patients recovering from distal radius fractures are commonly permitted to lift upwards of 5 lb during the early stages of rehabilitation (Orbay et al., 2006). Assuming a frictional coefficient of 1, approximately 110 N of force would be expected on the radius as a result of light active use of the hand. Ideally, a fracture fixation device will provide IFS's conducive to bone healing at loads within this range, and is capable of supporting loads well in excess.

There were two primary objectives of the experimental tests. The first was to determine if the mechanical fixation provided by the novel implant will result in IFS's conducive to bone healing in an extra-articular dorsally comminuted fracture model. The second was to compare the axial stiffness and failure strength of the novel implant to an existing percutaneous pinning treatment. It was hypothesized that the novel implant would support new bone formation and show greater stability than k-wire fixation providing evidence that an early return to function may be feasible when treated with the implant.

3.2 Methods

The experimental study was originally designed as a statistical comparison between two treatments: an implant group and a k-wire group. However, unanticipated results during the early stages of testing led to a more investigative approach.

3.2.1 Study Design

Foam cortical shell (FCS) sawbones (Model #1027, Pacific Research Laboratories) were selected as a test medium for *in vitro* tests. Sawbones were chosen for their consistent geometric and material properties, reducing intra-subject variability that is present between cadaver radii. The FCS model was determined to be most representative of osteoporotic bone expected in patients with extra-articular dorsally comminuted fractures. Also, previous biomechanical studies have used this model with good results (Drobetz et al., 2010; Weninger et al., 2010; Willis et al., 2006). These synthetic bones are manufactured with a solid rigid polyurethane foam shell and a cellular polyurethane foam core. The varying densities of polyurethane foam are intended to replicate the differences between human cortical and cancellous bone.

A total of 12 FCS sawbones were tested; 6 treated with the novel implant, and 6 treated with a standard k-wire technique. The k-wire technique that was used consists of 3 x 0.062" diameter wires positioned as shown in Figure 3.1. This technique was confirmed to be clinically relevant, and has been proven to be superior to other methods of k-wire fixation (Naidu et al., 1997). Samples were prepared with an extra-articular, dorsally comminuted fracture simulated by a 10 mm dorsal wedge osteotomy centered 20 mm proximal to the tip of the radial styloid. Many previous biomechanical studies have used a similar fracture model (Gondusky et al., 2011; Kandemir et al., 2008; Klitscher et al., 2010; Klos et al., 2010; Mehling et al., 2010; Sobky et al., 2007; Trease et al., 2005; Weninger et al., 2010; Willis et al., 2006).

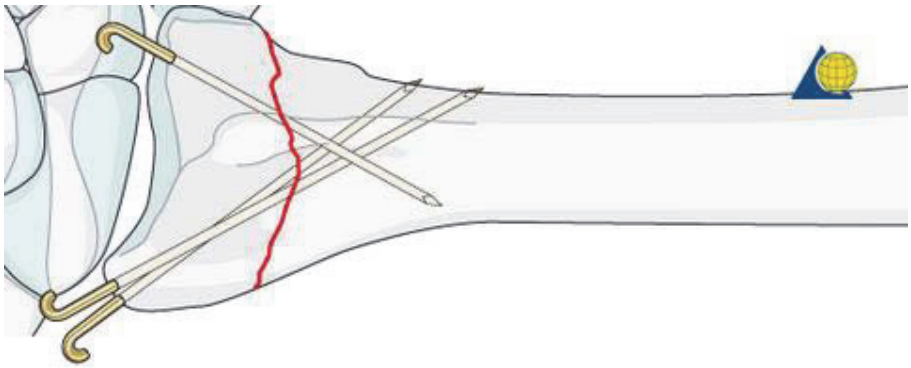

Figure 3.1: Standard k-wire technique used for experimental testing (AO Foundation)

In addition to the 12 FCS sawbones, 2 composite sawbones (Model #3407, Pacific Research Laboratories) treated with the novel implant were prepared. Composite sawbones have material properties that resemble healthy human bone. The cortical bone is simulated with a short fiber filled epoxy and cancellous bone is simulated with rigid polyurethane foam. The purpose of these additional tests was to compare failure loads and mechanisms between sawbones to provide some indication of how implant efficacy will be influenced by patient bone quality. All samples were tested in cyclic or quasi-static axial compression. All load testing was performed on an Instron (Model #8501) material testing machine using a 25 kN dynamic load cell. Data was collected at a sampling frequency of 100 Hz.

3.2.1.1 Cyclic Load Testing

Cyclic load testing was performed on a total of 6 samples; 4 FCS sawbones treated with k-wires and 2 FCS sawbones treated with implants. The objective was to determine whether mechanical fixation provided by the implant resulted in IFS's conducive to bone healing under simulated physiological loads. Samples were pre-loaded to 50 N and then cyclically loaded in a sinusoidal fashion from 10 to 110 N for 1000 cycles at 1 Hz. These loading parameters were selected to imitate cumulative physiological loads during the early stages of bone healing. The outcome measures used to assess fracture fixation were IFS and permanent deformation. To support new bone formation, IFS should be less than 15% (Claes et al., 1998; Egol et al., 2004; Perren et al, 1980). Fernandez (2001) suggested good clinical outcomes can be achieved if dorsal tilt is maintained below 10^{o}. Based on the fracture model used for testing, a linear displacement of 1.5 mm translates to 5^{o} of dorsal angulation. Therefore, to allow for a 5^{o} error in performing a closed reduction it is desired that permanent deformation be less than 1.5 mm.

3.2.1.2 Quasi-static Load Testing

Quasi-static loading was performed on a total of 8 samples; 2 FCS sawbones treated with k-wires, 4 FCS sawbones treated with implants, and 2 composite sawbones treated with implants. The objective was to quantify axial stiffness and failure strength for each of the samples. Samples were loaded at a rate of 1 N/s in axial compression until failure.

3.2.2 Sample Preparation

All samples were prepared using standardized methods in an effort to minimize variability between samples. Fractures were created with an oscillating saw using the custom cutting jig shown in Figure 3.2. A mold of the sawbones volar surface was made to accurately position each bone within the jig. Angular cutting blocks were used to guide the oscillating saw at the necessary angle to remove a 10 mm wide dorsal wedge. The initial fracture was created without compromising the volar cortex of the radius. The reason for this was to ensure the fractured bone was implanted in its anatomical position.

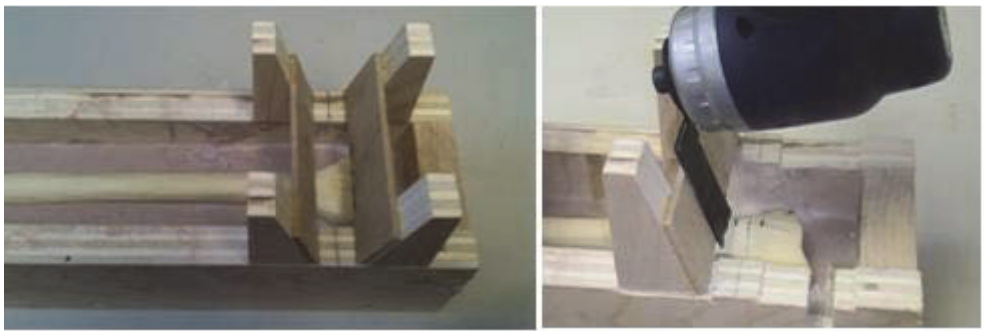

Figure 3.2: Custom cutting jig for creating fractures

Samples were fixed with either k-wires or the novel implant. K-wires were positioned based on targeted entry and exit points as specified by an orthopaedic surgeon. Entry points for the k-wires were identical between samples and exit points were within +/- 5 mm of the targeted position. In clinical practice k-wires are typically positioned free-handed, so this degree of variability was considered to be acceptable. K-wires were inserted such that the tip was just beginning to penetrate the cortical shell. For the FCS sawbones, implants were inserted using a prototyped version of the implant holder. They were implanted near the radial styloid and to a depth causing penetration of the medial cortex. For the composite sawbones a different approach was required due to the brittleness of the cortical shell material. A guide block was created so that three holes could be pre-drilled into the cortical shell corresponding to the three vertices of the angled implant. A thin file was used to remove the material between each of the three holes. This provided a v-shaped slot for the implant as shown in Figure 3.3, allowing it to be inserted without splitting the cortical shell. The hardness of the cortical layer prevented the implant from fully penetrating the medial cortex. Once the bones had been successfully implanted, an exacto knife was used to compromise the volar cortex while maintaining contact between the two pieces of bone.

Figure 3.3: V-shaped slot in composite sawbone to permit implantation

The proximal ends of the sawbones were removed such that the overall length of each sample was 180 mm. The custom potting jig shown in Figure 3.4 was used to pot each sample in an identical vertical orientation. The jig consists of a 2" diameter wooden dowel mounted to a ¾" thick board. A 5.5 mm diameter hole was drilled through the center of the dowel matching the central canal present in the sawbones. A steel rod with an equivalent diameter was positioned within the dowel extending 3" above the surface. The sawbones were able to slide over top of the steel rod allowing for repeatable vertical positioning. PVC tube, 2" in diameter and twice the height of the wooden dowel, was positioned over top of the dowel enclosing the bottom portion of the sawbones. Auto-body filler (Bondo) was used to fill the PVC tube and fix the bottom portion of the samples. The wooden dowel was covered in masking tape and sprayed with Pam to prevent the auto-body filler from bonding to its surface. Once the filler had set, the PVC tube was lifted off the dowel with the bone fixed in place. The potting jig was also designed to hold the samples during load testing. The ¾" board could easily be clamped to the Instron support plate and the samples were re-positioned on the wooden dowel for testing. Three set screws were used to clamp the bottom portion of the PVC tube to the wooden dowel to prevent rotation during testing.

Figure 3.4: Custom potting jig

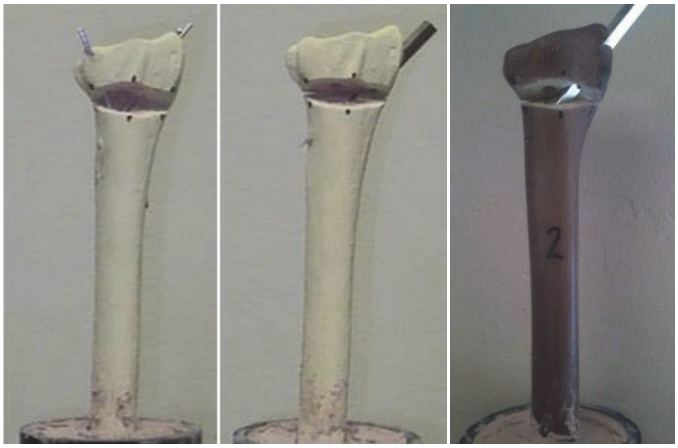

Figure 3.5: Implanted samples (left: FCS sawbone with k-wires, middle: FCS sawbone with implant, right: composite sawbone with implant)

3.2.3 Loading Configuration

Physiological loads on the radial joint surface are transferred from the scaphoid and lunate bones. Schuind et al. (1995) reported the load transmission ratio to be 61% through the radio-scaphoid joint and 39% through the radio-lunate joint with the hand in a neutral position. For experimental testing, the applied load was simplified as an evenly distributed force over the entire radial joint surface. Axial loads were transferred to the bone through a 1" diameter steel ball. Steel reinforced epoxy (JB Stik) was applied evenly over the joint surface and a ball was embedded on top. A sphere was selected for the loading interface to continually transfer axial loads even after initial dorsal displacement had occurred. The nature of the fracture model causes the fractured bone fragment to displace in dorsal angulation. As the fracture displaces, axial loads begin to induce a bending moment on the samples that is representative of hyperextension loading. Figure 3.6 shows the loading configuration used for experimental testing.

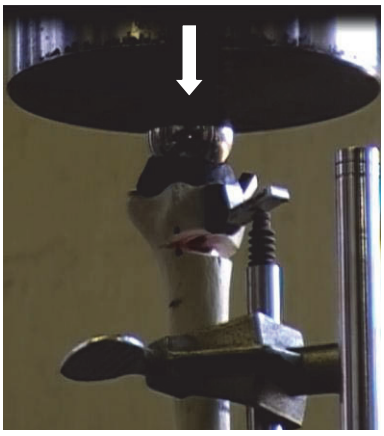

Figure 3.6: Loading configuration for experimental testing

3.2.4 Fracture Motion Measurement

Motion at the fracture site was measured using a linear variable displacement transducer (LVDT) (Model #2601-062, Instron). The maximum stroke length of this LVDT model is 6.0 mm. The LVDT is connected with the Instron material testing machine and operates at the same sampling frequency. A magnetic stand with an adjustable arm was fastened to the Instron support plate. The LVDT was positioned within the adjustable arm and next to the dorsal surface of the bone. An angled tab was bonded to the dorsal bone surface and flush with the distal fracture line using steel reinforced epoxy (JB Stik). The LVDT was positioned directly beneath the tab with only a

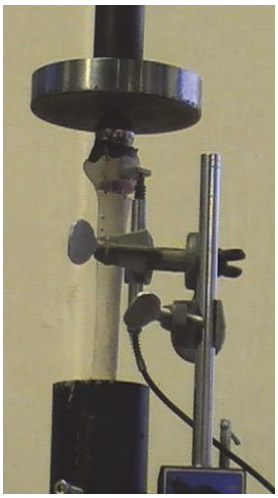

Figure 3.7: Experimental set-up of LVDT

slight displacement at no load in order to maximize the available stroke length. The experimental set-up can be seen in Figure 3.7.

3.2.5 Data Analysis

Four outcome measures were calculated from the experimental data: IFS, permanent deformation, axial stiffness, and failure strength. For this thesis, IFS was calculated using data from cyclic load testing. For a single cycle, IFS was calculated as the change in fracture gap width between the maximum and minimum peak loads divided by the fracture gap width at the minimum peak loads using the following equation:

$$\text{IFS}\ (\%) = \frac{\text{FD}_{\text{max}} - \text{FD}_{\text{min}}}{\text{FGW}_{\text{org}} - \text{FD}_{\text{min}}} * 100$$

The fracture gap width at the minimum peak load was determined by subtracting the fracture displacement at the minimum peak load from the original fracture gap width (FGW_{org}=10 mm). The first 50 load cycles were considered conditioning cycles to allow the fractured bone fragment to settle on the k-wires or implant. IFS was then calculated for each of the final 950 load cycles and the mean value was reported. Figure 3.8 shows how the parameters are defined on a plot showing fracture displacement at minimum and maximum peak loads. Permanent deformation was calculated as the difference between original fracture gap width and final fracture gap width after cyclic load testing. Measurements of fracture gap width were taken at the dorsal center of the fracture gap using calipers.

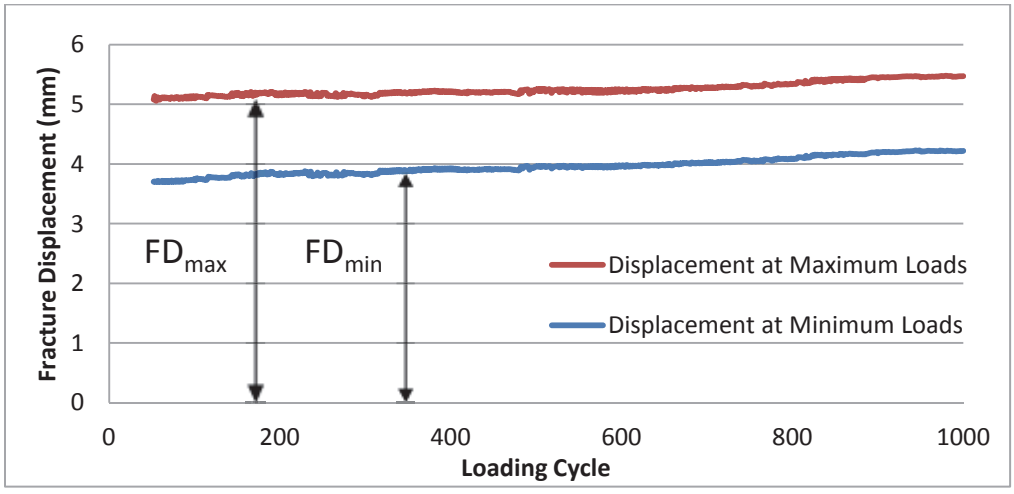

Figure 3.8: Parameters for IFS calculation from cyclic loading data

Axial stiffness and failure strength were both obtained from quasi-static load testing. Axial stiffness was calculated as the slope of the linear portion of the load versus displacement plots. The slope was obtained by fitting a linear trendline to the experimental data. Failure strength was defined as the load corresponding to the initial decrease in slope and was determined through visual inspection.

3.3 Results

Results from the *in vitro* experimental investigation are presented in two sections. First, data from the cyclic load testing is presented, followed by the quasi-static testing results.

3.3.1 Cyclic Load Testing

Desired magnitudes for maximum and minimum loads during cyclic testing could not be achieved experimentally due to the flexibility of the test samples and limitations of the Instron. The desired peak loads were 10 N and 110 N; however, experimental peak loads were approximately 30 N and 90 N. The inability of the Instron to reach the maximum and minimum loads was attributed to the short loading period and flexible nature of the sawbone material. Additionally, a 25 kN load cell was used for testing which is not optimized to operate at such low loads. The use of a 25 kN load cell contributed considerable noise to the loading curve. The cyclic load curve that was applied to the samples is shown in Figure 3.9.

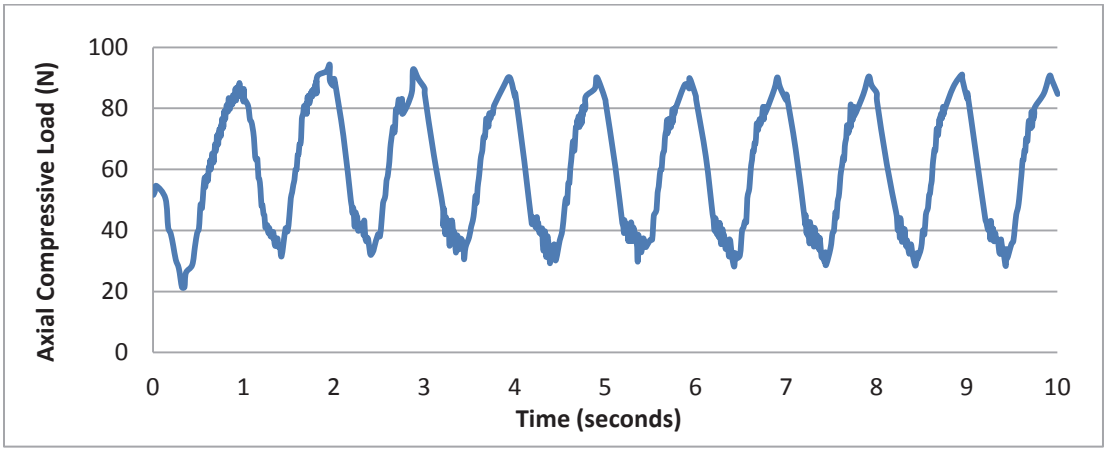

Figure 3.9: Experimental cyclic load curve (first 10 cycles)

A total of 6 samples were cyclically tested; 4 FCS sawbones treated with k-wires (Sample #'s: 1, 2, 3, 4), and 2 FCS sawbones treated with implants (Sample #'s: 5, 6). Calculated IFS's and permanent deformations are shown in Table 3.1. Of the 4 samples treated with k-wires, 2 endured the full 1000 cycle loading period and 2 failed within the first few loading cycles. Both samples treated with implants failed during early stages of loading. Load versus displacement plots and calculations for all samples can be found in Appendix A. For the two k-wire samples that endured the full loading period, load versus displacement was plotted for the first 50 cycles. For the remaining 950 cycles, fracture displacement at the minimum and maximum loads was plotted for each cycle. The calculated IFS's for these two samples were 21.44% and 24.03%. This level of relative motion is greater than the desired level required for new bone formation (15%). Permanent deformations at the fracture site were found to be 1.44 mm and 1.68 mm. These values are near the maximum threshold value of 1.5 mm indicative of poor clinical outcomes.

Table 3.1: Interfragmentary strains and permanent deformations for cyclically loaded samples

Sawbone Material Model	Fixation Type	Sample Number	Calculated IFS (%)	Permanent Deformation (mm)
Foam Cortical Shell	K-wires	1	21.44	1.44
Foam Cortical Shell	K-wires	2	Failed	Failed
Foam Cortical Shell	K-wires	3	24.03	1.68
Foam Cortical Shell	K-wires	4	Failed	Failed
Foam Cortical Shell	Implant	5	Failed	Failed
Foam Cortical Shell	Implant	6	Failed	Failed

The load versus displacement plots for k-wire samples #1 and #3 showed an interesting trend in k-wire stiffness. It was evident from the plots that the fractures displaced significantly over the first 2-3 loading cycles. After the first 2-3 cycles the load versus displacement became more consistent with only minor effects as a result of fatigue. This trend is shown in Figure 3.10, which displays the load versus displacement of k-wire sample #3 over the first 5 loading cycles. It appeared that this initial

displacement was a product of the fractured bone fragment slipping before settling on the k-wires, at which point the k-wires begin to support the load in bending. It is believed that failure in the cellular polyurethane foam core is a contributing factor to this initial displacement. The magnitude of the initial displacement was found to be in the range of 2.5-3.0 mm. Based on the calculated permanent deformations, some of this initial displacement was recovered once the load was the removed.

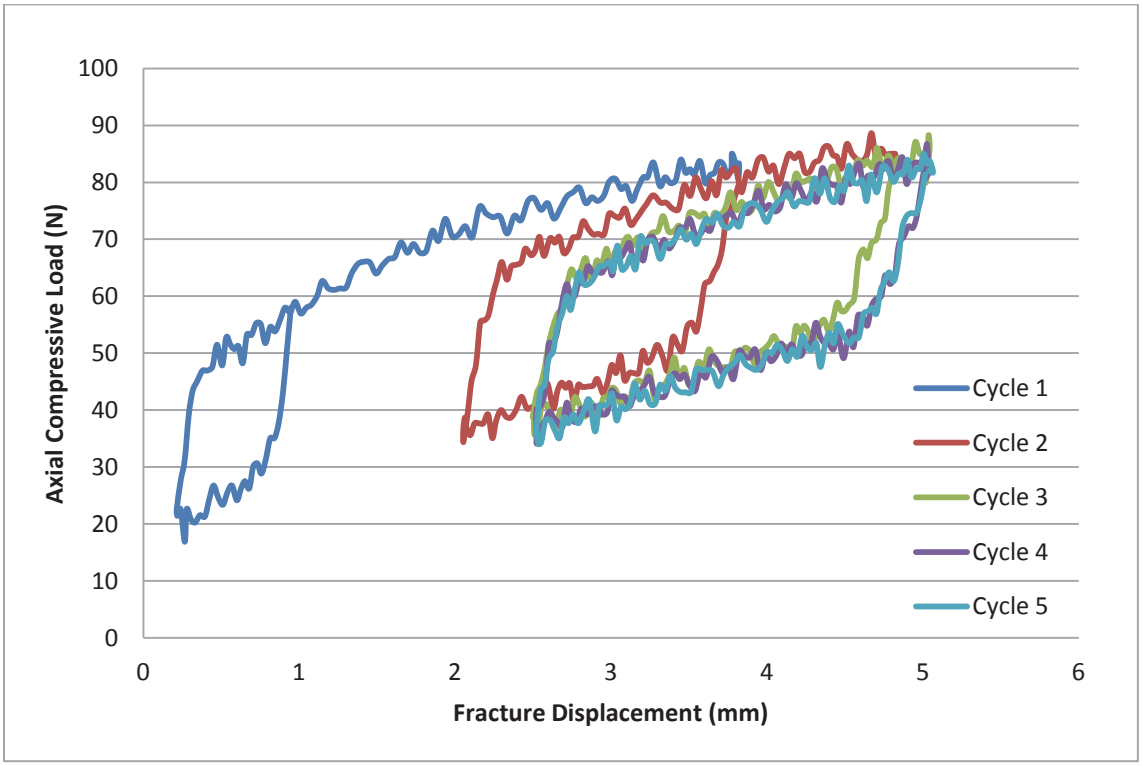

Figure 3.10: Load versus displacement for k-wire sample #3 over first 5 loading cycles

Inconsistent results were found between k-wire samples, with two enduring the full loading period and two failing during the early stages of loading. A comparison of the four k-wire samples exposed one major difference between samples #1 and #3 and samples #2 and #4. The difference was in the positioning of the k-wire inserted through the dorsoulnar rim of the radius. In samples #1 and #3 the placement of this k-wire was found to be on the dorsal side of the other two k-wires. However, in samples #2 and #4 this k-wire passed the other two k-wires on the volar side. Figure 3.11 shows the difference in k-wire placement.

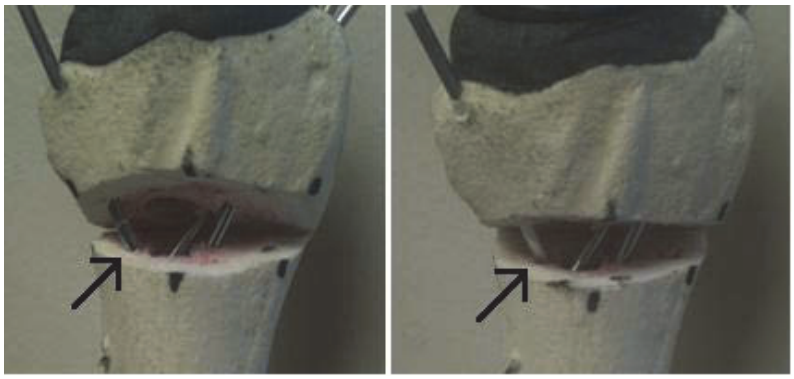

Figure 3.11: K-wire placement (left: k-wire sample #3, right: k-wire sample #4)

Failure of the two k-wire samples was caused as a result of k-wire loosening leading to fracture collapse. There was some evidence of failure in the cellular polyurethane foam core material caused by shearing forces generated at the k-wire interface. Also, as the load increased distal penetration of the k-wires was evident as shown in Figure 3.12. This combination of loosening and distal penetration led to displacement at the fracture site and eventual failure. Minor bending in the k-wires was apparent at higher loads. However, stresses in the k-wires did not appear to exceed the elastic limit as no plastic deformation was visible.

Figure 3.12: K-wire penetration through the medial cortex

The failure mode of the two samples treated with implants was also caused by implant loosening; however, the mode of implant loosening was different. It was clear that failure occurred in the rigid polyurethane foam shell at the implant/bone interface. As the load increased, a gap formed between the implant and bone near the point of entry as highlighted in Figure 3.13. As the size of this gap widened the fractured bone fragment became increasingly unstable and began to move freely around the implant. This eventually caused fracture collapse in dorsal angulation with a slight degree of rotation about the implant.

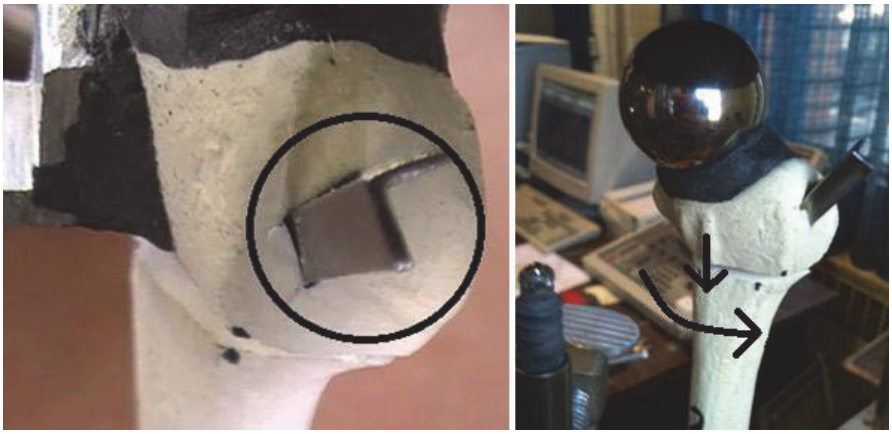

Figure 3.13: Failure mode of foam cortical shell sawbone treated with implant

3.3.2 Quasi-static Load Testing

The incidence of k-wire and implant failure during cyclic testing prevented accurate determination of the implants limitations. For cyclic testing, a pre-load of 50 N was applied to the samples making it difficult to interpret exactly when failures occurred. Therefore, quasi-static load testing was performed to accurately quantify axial stiffness and failure load.

A total of 8 samples were tested quasi-statically; 2 FCS sawbones treated with k-wires (Sample #'s: 7, 8), 4 FCS sawbones treated with implants (Sample #'s: 9, 10, 11, 12), and 2 composite sawbones treated with implants (Sample #'s: 13, 14). Calculated axial stiffness and failure strengths for each sample are shown in Table 3.2. Load versus displacement plots for each sample are provided in Appendix B.

Table 3.2: Axial stiffness and failure strength for quasi-statically loaded samples

Sawbone Material Model	Fixation Type	Sample Number	Calculated Axial Stiffness (N/mm)	Failure Strength (N)
Foam Cortical Shell	K-wires	7	20.71	40
Foam Cortical Shell	K-wires	8	20.96	85
Foam Cortical Shell	Implant	9	46.50	31
Foam Cortical Shell	Implant	10	37.54	30
Foam Cortical Shell	Implant	11	54.93	29
Foam Cortical Shell	Implant	12	39.72	32
Composite	Implant	13	98.74	105
Composite	Implant	14	498.41	175

The k-wire samples exhibited similar results to those found during cyclic load testing. Load versus displacement for the two k-wire samples are plotted in Figure 3.14. It was evident from these plots that two different levels of axial stiffness were present. The slope of the curve is steep initially until the fractured bone fragment slips and eventually settles on the k-wires. At this point the slope decreases until eventual failure. The initial axial stiffness was found to be 165.1 N/mm and 175.9 N/mm for samples #7 and #8, respectively. Axial stiffness drops to 20.71 N/mm and 20.96 N/mm once the fractured fragment has settled on the k-wires. As shown by the plots, sample #7 fails at less than half the failure load of sample #8. Comparison of k-wire placement showed the same difference that was seen between cyclically loaded samples. The k-wire inserted through the dorsoulnar rim of the radius was positioned on the volar side of the other two k-wires in sample #7 and on the dorsal side in sample #8. It appears that the positioning of this k-wire has a significant influence on failure strength of the k-wire samples.

As shown in Figure 3.15, results for the FCS sawbones treated with implants were fairly consistent. The mean axial stiffness was found to be 44.67 N/mm and the mean failure strength was 30.5 N. The axial stiffness of the implant samples was more than twice the stiffness of the k-wire samples, although failure strength was far lower than k-wire sample #8. The same mode of failure that was witnessed during cyclic loading was evident during quasi-static loading.

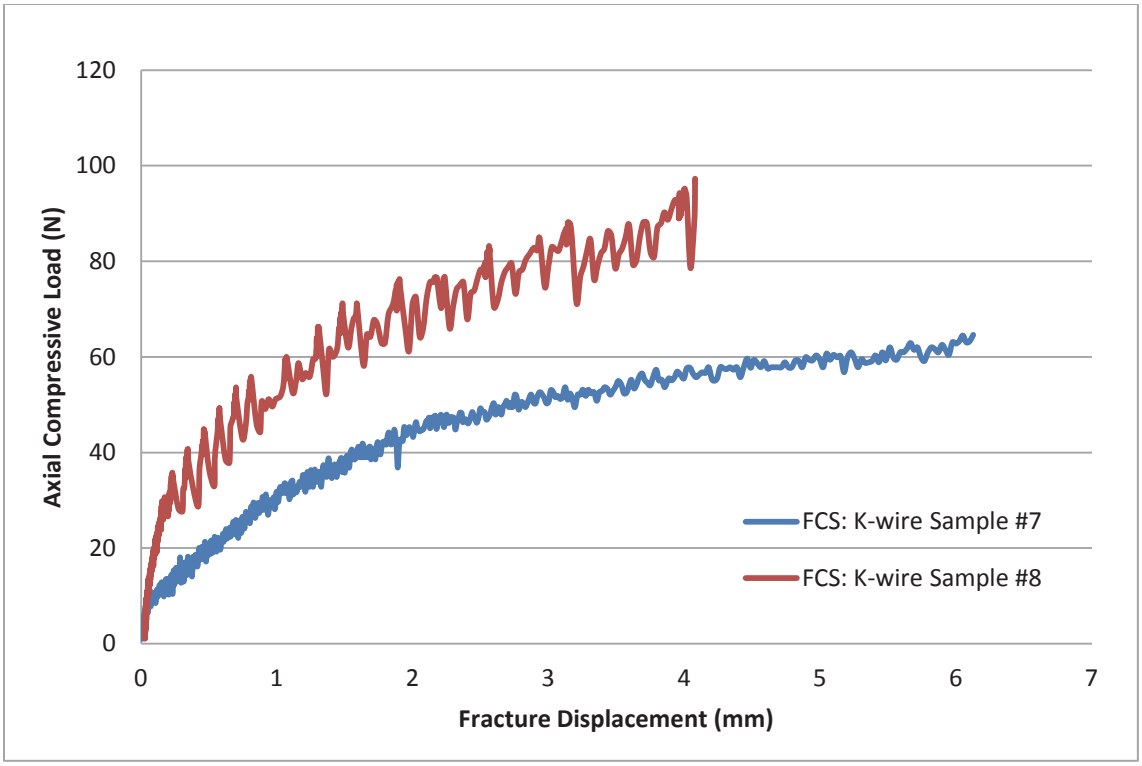

Figure 3.14: Load versus displacement plot for FCS k-wire samples tested quasi-statically

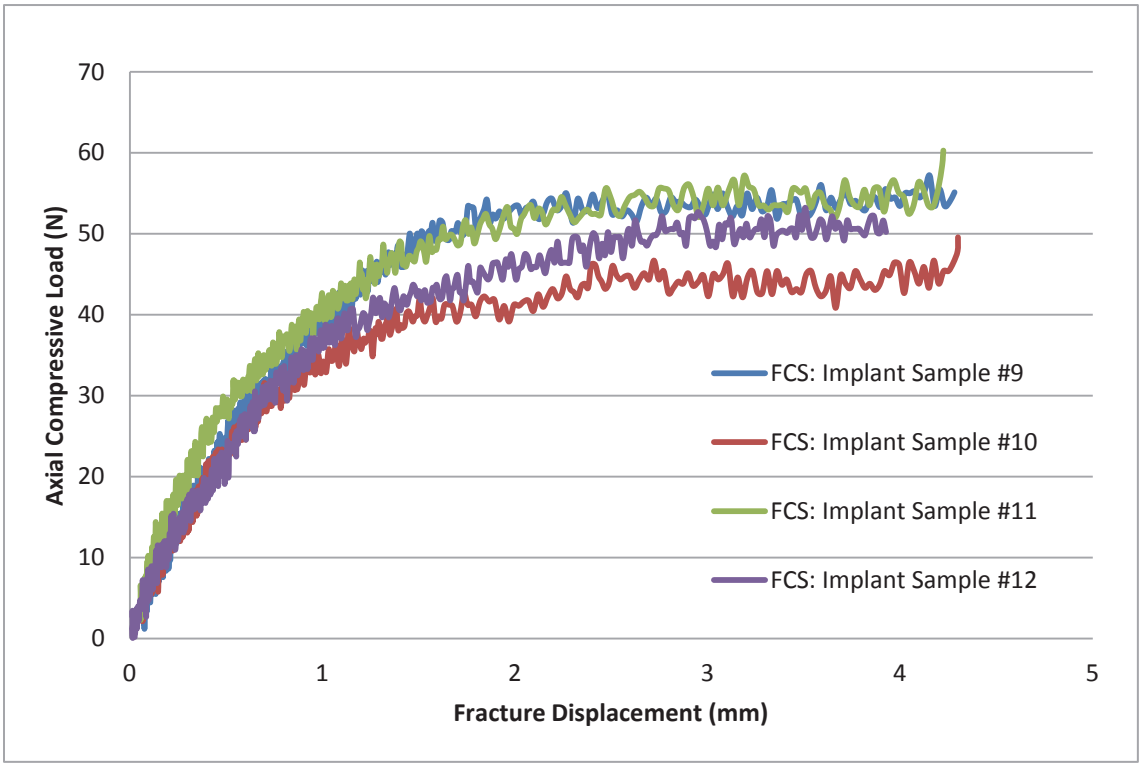

Figure 3.15: Load versus displacement plot for FCS implant samples tested quasi-statically

Load versus displacement plots for the two composite sawbones treated with implants are shown in Figure 3.16. Similar to the k-wire samples, two differing levels of axial stiffness were apparent. Initially the axial stiffness was 189.84 N/mm for sample #13 and 227.10 N/mm for sample #14. Once the load reached approximately 40 N, the axial stiffness of sample #13 decreased to 98.74 N/mm and the axial stiffness of sample #14 increased to 498.41 N/mm. It is believed that the change in axial stiffness is a result of compression failure in the rigid polyurethane foam core. The composite sawbones were prepared by first removing a v-shaped slot from the cortical shell prior to inserting the implant. The slots were likely oversized meaning the implant relied more heavily on purchase in the polyurethane foam core initially. The polyurethane foam core in composite sawbones is similar to the rigid polyurethane foam shell on FCS sawbones. As shown in the FCS samples, this material failed at loads beyond 30 N. This corresponds to the load at which a change in stiffness was seen in the composite samples. Once the polyurethane foam has compressed slightly it is expected that a greater proportion of the load would be distributed through the stronger cortical shell.

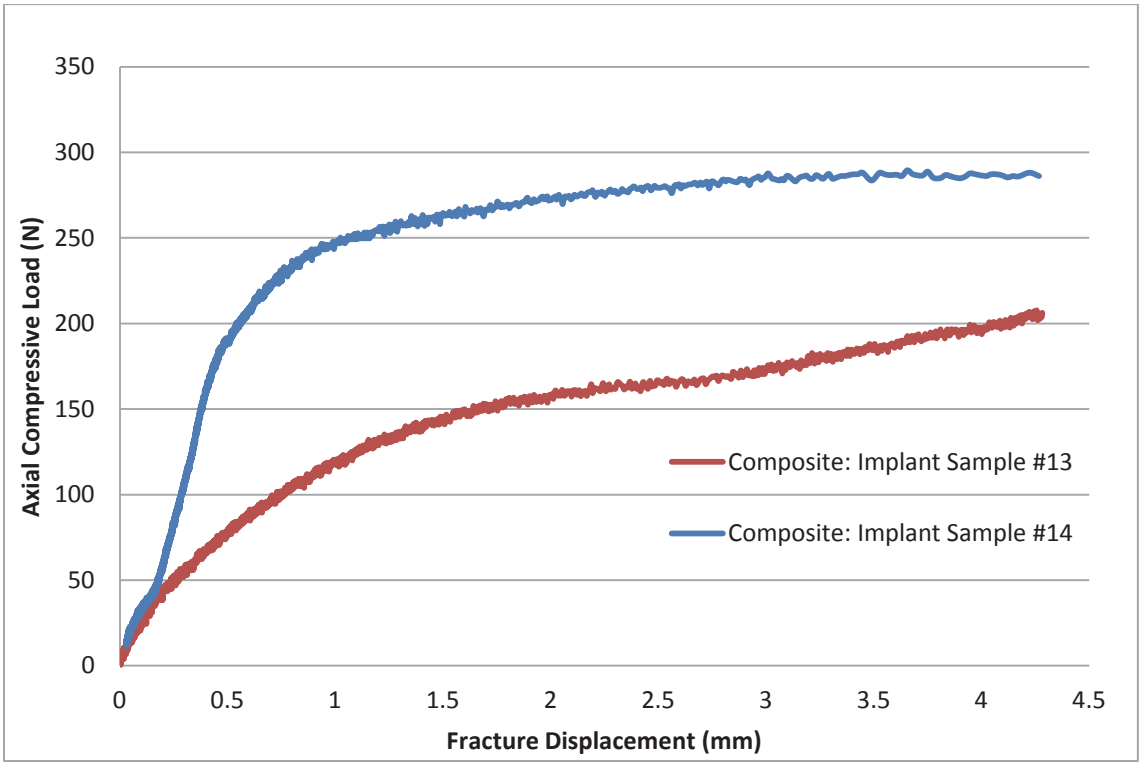

Figure 3.16: Load versus displacement plot for composite implant samples tested quasi-statically

As shown, the axial stiffness and failure strength of sample #14 is much higher than sample #13. Further inspection of the two samples showed that positioning of the steel balls used for loading may have contributed to the difference in stiffness. The ball on sample #13 was mounted with greater dorsal angulation as shown in Figure 3.17. This likely induced a greater bending moment on the sample causing increased displacement. During testing, bowing of the radial shaft was witnessed only on sample #13 further validating the hypothesis that it experienced a greater bending moment. Dorsal bending moments can be expected *in vivo* when the hand is in an extended position. Therefore, this is thought to be more representative of a typical loading scenario. The positioning of the steel ball on sample #14 was believed to be too volar, transferring greater loads through the contacting volar cortex, and resulting in a higher stiffness.

Figure 3.17: Composite sawbone samples (left: sample #13, right: sample #14)

Despite the variability between samples, stiffness and failure strengths were significantly higher in both composite sawbones compared to FCS sawbones. This was expected due to the increased strength of the cortical shell in composite sawbones. The failure mode was different as well, and was caused by a combination of failure in the cancellous foam core and implant bending.

3.4 Discussion

Results from the cyclic load tests in FCS sawbones revealed that mechanical fixation provided by the novel implant does not support physiological loads that would be expected during an early return to function. K-wires were found to provide improved fixation compared to implants, but were also unable to support physiological loads in a manner conducive to bone healing. This confirms the accepted clinical theory that although k-wires are capable of providing improved fixation they are unable to support an early return to function. The placement of the k-wire through the dorsoulnar rim of the radius was shown to have a significant impact on the failure strength of k-wire samples. For optimal fixation strength, care should be taken to position this k-wire on the dorsal side of the two k-wires inserted through the radial styloid. The dorsal side of the radius is inherently unstable in this fracture model making dorsal placement of this k-wire more advantageous.

The mean axial stiffness of the FCS sawbones treated with implants was found to be greater than the axial stiffness of the k-wire samples. The mean stiffness of the implant samples was calculated to be 44.67 N/mm; however, the mean failure strength was only 30.5 N. Failure occurred in the rigid polyurethane foam shell causing implant loosening and eventual fracture collapse. This mode of failure is attributed to the high degree of stiffness mismatch between the rigid polyurethane foam and the implant. The implant provides a single point of fixation meaning applied loads are transferred solely through that point. Evidently, this led to high stresses at the interface between the implant and bone that exceeded the yield strength of the rigid polyurethane foam. As the applied load increased, sawbone material failure resulted in the formation of a gap between the implant and bone leading to failure. Contrarily, k-wires provide three points of fixation allowing a more advantageous load distribution. Also, a single k-wire is far less stiff than the novel implant reducing the stiffness mismatch between the k-wire and sawbone material.

To further evaluate limitations of the novel implant, two additional quasi-static tests were performed on composite sawbones. Composite sawbones have properties that resemble healthy human bone. The yield strength of the composite cortical shell is 157

MPa, compared to just 8.4 MPa for the FCS sawbones. As a result the composite sawbones could withstand greater loads compared to FCS sawbones. The failure strengths of the two composite sawbone samples were 105 N and 175 N. Failure was caused by a combination of compression failure in the cancellous foam core and implant bending. These failure loads are at the low end of expected physiological loads confirming that the implant is unable to restore early function of the hand and wrist.

Several past biomechanical studies have used FCS sawbones (Drobetz et al., 2010; Lindley et al., 2012; Martineau et al., 2008; Sobky et al., 2007; Weninger et al, 2010; Willis et al., 2006) with a smaller number using composite sawbones (Dahl et al., 2012; Sokol et al., 2011). Each of these past studies was performed on internal fixation techniques to evaluate different plate designs and screw positioning. Willis et al. (2006) conducted a study using an identical FCS sawbone and fracture model to those used in this thesis. The findings showed volar locked plates to have an axial stiffness of approximately 230 N/mm. A similar result was reported by Lindley et al. (2012). In addition, Lindley evaluated failure strengths reporting clinical failure loads of 460 N and catastrophic failure loads of 892 N. Clinical failure was defined as fracture displacement greater than 2 mm and was caused by plastic deformation of the sawbone and plate materials. Catastrophic failure occurred via comminution of the distal fragment along the lines of screw placement resulting in complete fracture collapse. This mode of failure matches what was seen with the novel implant. However, stiffness and failure strengths of volar locked plates are significantly higher. Fixation with volar locked plates is achieved by positioning multiple screws through the distal bone fragment. Multiple points of fixation serve to increase construct stiffness while distributing the load over several screws. This helps to increase failure strength by minimizing areas of high stress concentration in the bone.

A comparable study conducted on composite sawbones found the axial stiffness of volar locked plates to vary between 150 N/mm and 300 N/mm (Dahl et al., 2012). Failure loads in composite sawbones were higher than in FCS sawbones with values ranging between 1000 N and 2000 N. The mode of failure was reported as plate bending in this study. These differences in failure strength and failure mode match the differences seen in this thesis between FCS and composite sawbones.

There is only one known study that has evaluated the k-wire fixation technique used in this thesis under axial loads (Knox et al., 2007). Knox used cadaver specimens to compare k-wires to volar locked plates. An intra-articular fracture was modeled and five motor tendons of the wrist were left intact. The tendons were connected to a loading device and the specimens were loaded incrementally from 36 N to 100 N. Displacement at the fracture site was measured with calipers at each load interval. At 36 N, mean fracture displacement in the k-wire specimens was 1.4 mm, compared to 3.7 mm at 100 N. This translates to an axial stiffness of approximately 28 N/mm. Given the major differences in study design this result is comparable to the mean stiffness of 20.8 N/mm for the k-wire samples in this thesis further validating the use of sawbones.

Axial loads were selected based on previous experimental data showing that 10 N of grip strength translates to between 26 N and 52 N of force on the radius (Putnam et al., 2000). It has been suggested that axial compressive forces caused by light active motion of the wrist are approximately 100 N, and that forces caused by combined motion of the wrist and digits do not exceed 250 N (Mehling et al., 2010). Although loads are not expected to surpass 250 N during the early stages of healing, higher failure strength is desirable. The average male grip strength has been reported as 463 N (Mathiowetz et al., 1985). This correlates to a maximum force on the radius upwards of 2410 N. This is higher than reported failure strengths of volar locked plates; however, maximal gripping activities are not likely to occur during early post-operative rehabilitation. Therefore, volar locked plates are considered to be sufficient to permit an early return to function. Based on the experimental failure strengths of the k-wire and implant constructs, neither treatment is capable of restoring hand and wrist mobility during the early stages of healing.

3.4.1 Limitations

A number of limitations were present in the design of the *in vitro* tests. *In vitro* testing was performed on sawbones as they offer consistent geometry and material properties at a low cost. However, it is difficult to interpret how the results will translate to human bone, particularly osteoporotic bone. In addition, the presence of surrounding soft tissues, neighboring bones, and hydrostatic pressures would influence how the

implant performs *in vivo*. For this thesis only axial loading was considered and loads were evenly distributed over the radial joint surface. Any future *in vitro* testing should consider bending and torsion loading as well. As well, the loading configuration could be improved to reduce variability between samples and more accurately represent the physiological loading scenario. This could be accomplished by performing tests on intact cadaver radii, and loading the radio-carpal joint using the extrinsic tendons that control hand motion. Also, variability was seen in the k-wire samples due to inconsistent positioning of the k-wire through the dorsoulnar rim. If any further comparisons are made, greater care should be taken when positioning the k-wires.

Additional improvements could be made to the set up of the experimental equipment. An LVDT was used to measure fracture displacement, which only captures motion in one direction. The fractured bone fragment displaced in dorsal angulation making it difficult to position the LVDT to measure linear motion. The positioning of the LVDT was offset from the dorsal cortex which may have impacted the accuracy of the displacement measurement. Also, because the tip of the LVDT was not attached to the measurement tab it had a tendency to slide along the tab as the fracture displaced. Ideally, a 3D motion capture system would be used to measure displacement in all directions. Testing was limited to the use of a 25 kN load cell due to equipment availability at the time of testing. This prevented the peak loads from being reached during cyclic testing and also created significant noise in the load curves. A 5 kN load cell would have been optimal for testing at loads within the range of 100 N.

3.4.2 Conclusion

In vitro testing on FCS sawbones demonstrated that mechanical fixation provided by the novel implant does not support an early return to function in an extra-articular dorsally comminuted fracture model. The implant had a greater axial stiffness than k-wire fixation, but lower failure strength. Although k-wire fixation had increased failure strength, IFS's were outside the desirable range for new bone formation. This result agrees with clinical practice that k-wire fixation is insufficient for providing an early return to function. The implant was found to have a higher axial stiffness and failure strength in composite sawbones compared to FCS sawbones. However, implant bending was evident at the low end of anticipated physiological loads.

CHAPTER 4 FINITE ELEMENT ANALYSIS OF THE NOVEL IMPLANT

4.1 Introduction

FEA is a computational technique used to numerically model mechanical stress and strain. The adaptability of a numerical model makes it a useful tool for collecting pre-clinical data. Experimental testing can be costly, time consuming and often requires several comparative studies on the same specimen. A numerical model has the unique ability to isolate and manipulate a single variable while measuring its effect quantitatively. There exist multiple approaches to creating a finite element model. A model can be extremely complex and offer highly accurate results, or a simpler model can be created that provides moderate to good results. The optimal tradeoff between complexity and model accuracy depends on the application and desired outcomes. To verify model accuracy, it is standard practice to perform a validation either qualitatively, analytically, or experimentally. An experimental validation is considered to be the gold standard as this proves the model matches the physical scenario.

The objective of this FEA was to create a model of a fractured distal radius treated with the novel implant, and to validate the model against the previously presented experimental results. The goal was to create a model that is able to calculate axial stiffness within +/-10% of the experimentally determined axial stiffness for both FCS and composite sawbones. The finite element model will be used as reassurance of the experimental data and for simulation of implant performance in human bone. A valid model will act as a valuable tool for future design optimization and alternative testing scenarios.

4.2 Methods

4.2.1 Model Generation

A geometric model of a fractured distal radius treated with the novel implant was created using Solid Edge CAD software. The dimensions of the radius bone were selected

to resemble the sawbones used for experimental testing. The distal region of the radius was simplified as a tapered cylinder to avoid modeling the complex surface contours of a radius. Based on the dimensions of the sawbones, the bone was modeled as a cylinder with a 35/20 mm taper beginning at the joint surface and extending an overall length of 75 mm. The area of interest is near the fracture site so it is reasonable to reduce the length in order to simplify the model and reduce computational cost. The sawbones are manufactured with a 5.5 mm diameter canal slightly offset from center. This canal was included in the model for improved accuracy.

A fracture identical to the one modeled experimentally was added to the CAD model. This was accomplished by removing a wedge of material 10 mm wide, centered 20 mm proximal to the joint surface. Next, a v-shaped slot was cut out from the bone at an angle closely matching the implant angle in the experimental samples. The proximal and distal bones were separated at the fracture line into two different part files. An assembly was then created to include the two pieces of bone as well as a model of the implant. The implant model was identical to the physical prototypes except for the exclusion of the sharp cutting edge. The reason for excluding the cutting edge is explained in the next section. The final assembly consisted of the two pieces of bone in their original alignment and the implant positioned within the v-shaped slot. Figure 4.1 shows a comparison of the experimental model and the geometry used for FEA.

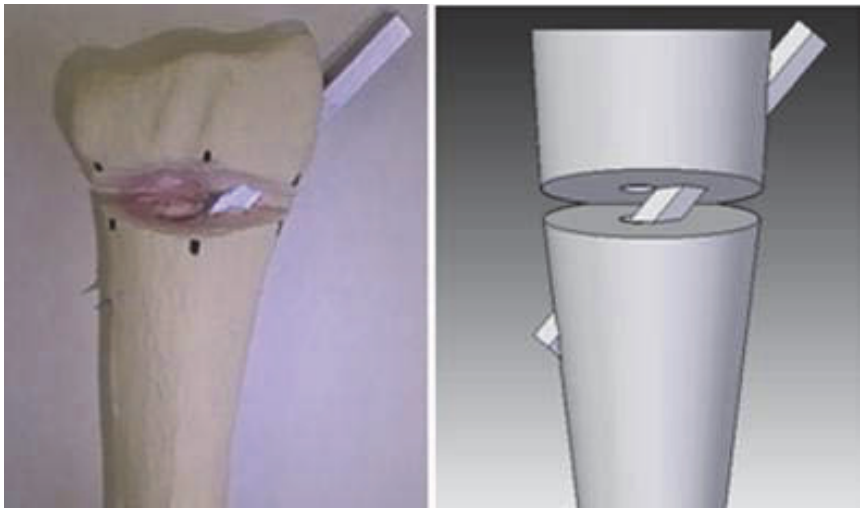

Figure 4.1: Experimental model versus finite element model geometry

4.2.2 Model Meshing

A finite element mesh was created using Altair HyperMesh software and LS-DYNA code was used for finite element computation. The geometry shown in Figure 4.1 was imported as an IGES file into Hypermesh. The first step was to create three different solid components: one for the implant and one for each piece of bone. Each of these components was meshed individually. In order to attain the desired level of accuracy it was necessary to use 3D brick elements. The simplicity of the implant geometry permitted the use of hexahedral brick elements. A 2D surface mesh consisting of quad elements was created on one end and was subsequently mapped over the length of the implant. This element choice provides accurate formulation for all forms of stress including bending and shear. The geometry of the bone was more intricate due to the presence of the fracture and the angled slot. As a result, the bone could not easily be meshed with hexahedral elements and instead tetrahedral elements were used. Although tetrahedral elements can only calculate constant stress and strain over an element they are very fast computationally and are sufficient for this problem.

In order to separate cortical bone from cancellous bone the entity sets command was used. An element set was created that was representative of the cortical and cancellous material for each piece of bone. The elements chosen for the cortical sets were selected to match the thickness of the cortical bone on the sawbones. The remaining elements were assigned to the cancellous bone sets. Four new component collectors were created and labeled: distal cortical bone, distal cancellous bone, proximal cortical bone, and proximal cancellous bone. Using the organize command, element sets were moved to their corresponding component collectors. The resulting mesh enabled the cortical and cancellous bone to be assigned different material properties without having to define an interface between them. It is reasonable to assume that the cancellous bone is permanently bonded to the cortical shell.

Again the entity sets command was used to create node sets for defining boundary conditions and loads. Three different node sets were created: one for all nodes at the distal end of the implant, one for all nodes on the proximal surface of the bone, and one for all nodes on the distal surface of the bone. Once this was completed, the mesh was exported as an LS-DYNA solver deck. Additional input decks were created for each part

file and one for material property definition. Finally, a driver file was created to load the mesh, part files, material properties, and to define boundary conditions, loads, and contacts.

Boundary conditions were applied to fully constrain the distal end of the implant and proximal surface of the bone. It is assumed that the sharp cutting edge of the implant provides a rigid fixation in the medial cortex of the radius. Fully constraining the distal end of the implant simulates this rigid fixation without having to model the intricate geometry of the sharp edge. The purpose of constraining the proximal surface of the bone was to analyze load transfer through the fracture site. This boundary condition replicates the experimental set-up. An external load was applied to the nodes on the distal surface of the bone. A load curve was defined to apply a quasi-static axial compressive load in a time period of 0.01 seconds. The short loading period was chosen to reduce computational time and will not impact accuracy because a linear elastic material model was used. The magnitude of the load was selected by dividing the overall desired load by the total number of nodes on the distal surface.

The implant relies on bone purchase to provide fracture fixation. Therefore, an additional boundary condition was required to characterize the implant/bone interface. An automatic surface to surface contact was defined based on a frictional contact between the implant and bone. Coefficients of friction were chosen as 0.3 and 0.5 for cancellous and cortical bone, respectively. These values have been previously validated for stainless steel pin fixation of distal radius fractures in cadaver radii (Rogge et al., 2002). One experimental study that evaluated the coefficient of friction between titanium and sawbone materials found values in the range of 0.35 (Lucas et al., 2006). Based on these results, 0.3 and 0.5 were considered to be reasonable approximations for both the sawbone and human bone models.

Prior to any calculations, a mesh convergence study was conducted to select an element size that would optimize computational time without limiting model accuracy. For the convergence study the bone was defined as one solid material to prevent variability in cortical shell thickness between element sizes from impacting the results. Meshes were created for six different element sizes: 8.0 mm, 4.0 mm, 2.0 mm, 1.0 mm, 0.5 mm, and 0.25 mm. Each model was loaded under 40 N of axial compression and

measures of fracture displacement were taken from the elements located at the center of the dorsal surface as shown in Figure 4.2.

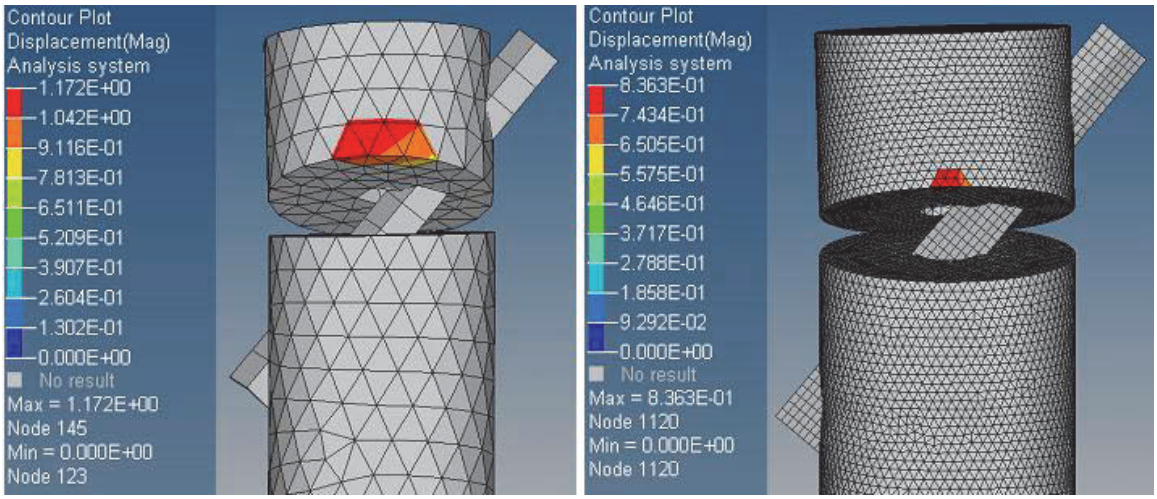

Figure 4.2: Dorsal edge displacement for 4.0 mm (left) and 1.0 mm (right) mesh sizes

The computational time for each element size was recorded and plotted along with fracture displacement as shown in Figure 4.3. Convergence of fracture displacement was seen between element sizes of 2.0 mm and 1.0 mm. However, when the element size was reduced to 0.5 mm the displacement decreased. It is known that reducing the size of tetrahedral elements can create an over-stiffening effect causing inaccurate results. An attempt was made to further reduce the mesh size to 0.25 mm; however, this caused Hypermesh to crash due to the large number of elements. Based on these results it was decided that an element size of 2.0 mm was optimal as it demonstrated convergence and required minimal computational cost. An element size of 2.0 mm has been selected using mesh convergence studies in previous finite element models of the distal radius as well (Cheng et al., 2007). This selection was validated against experimental results to confirm model accuracy and to reassure that the calculated displacement with a mesh size of 0.5 mm was a result of over-stiffening. Figure 4.4 shows the final mesh that was used for FEA of the sawbone models.

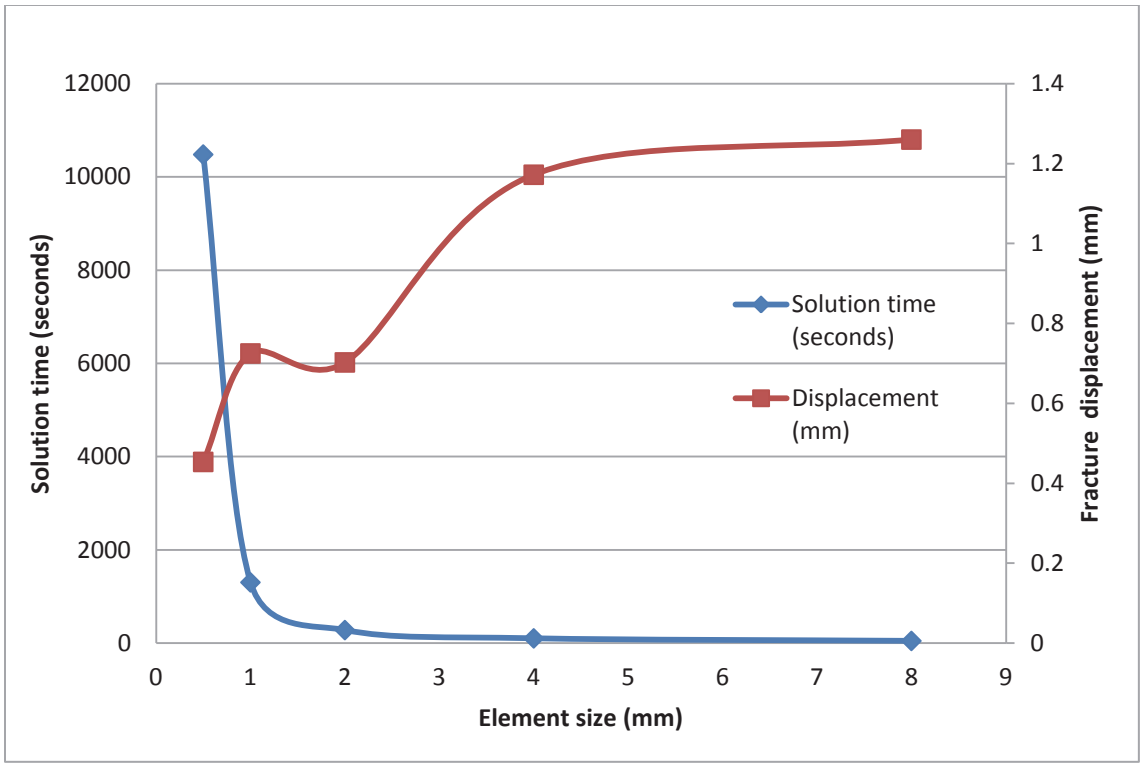

Figure 4.3: Results from mesh convergence study for fracture displacement

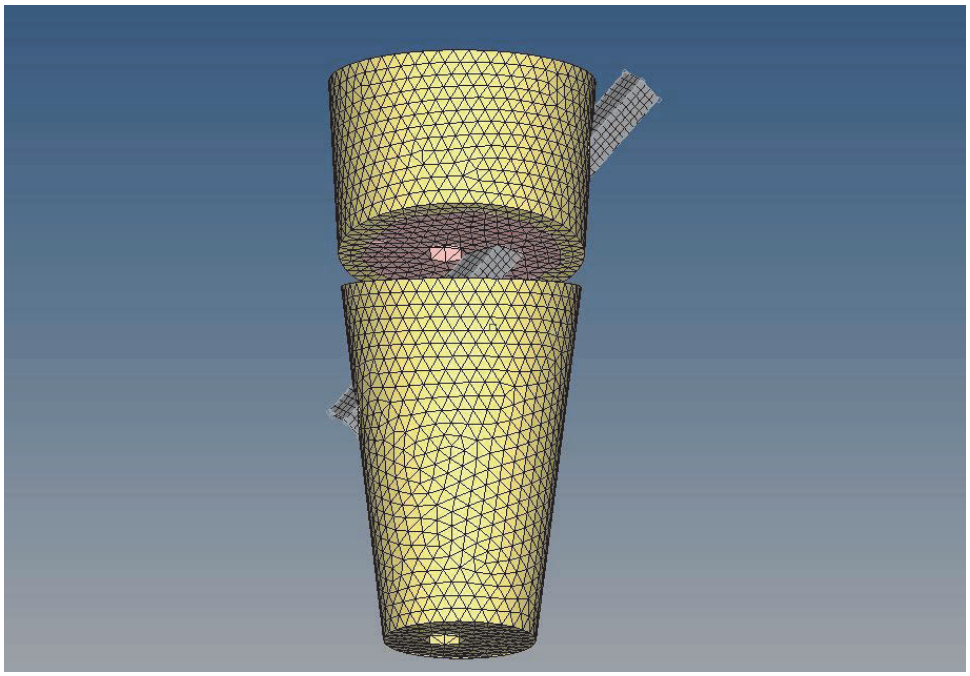

Figure 4.4: Finite element mesh (2 mm) for sawbone models

4.2.3 Model Validation

Model validation was performed using experimental data from quasi-static testing on both FCS and composite sawbones. Calculated values of axial stiffness from the experimental tests were compared to numerical results. Material properties shown in Table 4.1 were applied to the respective finite element models. All materials were defined as isotropic and linearly elastic. The stainless steel 316L implant was defined as having an elastic modulus of 193 GPa, density of 8.0 g/cc, and poisson's ratio of 0.3 (MatWeb). The suggested yield strength for this material is 205 MPa. Since materials were modeled as linearly elastic only loads within the experimental elastic range were applied to the finite element model. Finite element analyses were performed at five load points encompassing the experimental elastic region for the respective sawbone model. For each load, a single element located on the fractured fragment at the center of the dorsal bone surface was selected and displacement in the Z-direction was recorded. The Z-direction corresponds to the direction of linear displacement that was measured experimentally. These five data points were plotted and a linear trendline was fit to the data. The numerical axial stiffness was defined as the slope of this line. For the FCS sawbone model, numerical displacements were also compared to experimental displacements calculated from the mean experimental stiffness in order to approximate errors in displacement magnitude. Due to the variability in the two composite sawbones, numerical data was compared to experimental data from sample #13 for the composite sawbone model. It is believed that sample #14 was loaded too volarly, resulting in an abnormally high stiffness.

Table 4.1: Material properties of sawbone models used for FEA

Sawbone Model	Bone Material	Elastic Modulus (GPa)	Density (g/cc)	Poisson's Ratio	Comp. Yield Strength (MPa)
Foam Cortical Shell #1027	Cortical	0.210	0.32	0.3	8.4
	Cancellous	0.058	0.16	0.3	2.2
Composite #3407	Cortical	16.7	1.64	0.3	157
	Cancellous	0.155	0.27	0.3	6.0

Stress analysis was used as a secondary method for model validation. The maximum von Mises stress in the cortical and cancellous bone, as well as the implant was evaluated at each load. These values were compared to material yield strengths to determine if the model could be used to predict mode of failure, or more precisely failure strength.

4.2.4 Human Bone Model

Once the finite element model had been validated, a final model was created to simulate human bone. Aside from altering material properties, the human bone model was adjusted to compensate for the abnormally thick cortical layer present in sawbones. The cortical layer of bone in the distal metaphyseal region of a radius is known to be very thin. Figure 1.1 demonstrates how cortical bone diminishes from the shaft of the radius to the distal end. Nielson et al. (2001) used high-precision peripheral quantitative computed tomography to compare bone density and cortical bone thickness between female patients who had experienced a distal radius fracture and a younger group of healthy females. The results showed decreased bone density and cortical bone thickness in the fracture group. Cancellous and cortical bone densities in this group were in the range of 0.20 g/cc and 1.0 g/cc, respectively. These densities were applied to the finite element model in an attempt to simulate the properties of a typical patient. Cortical bone thickness in the distal region was found to be around 1.5 mm. To replicate this, the element size in the finite element model was reduced from 2.0 mm to 1.5 mm, and a single layer of elements was selected to represent cortical bone. The resultant finite element mesh is shown in Figure 4.5.

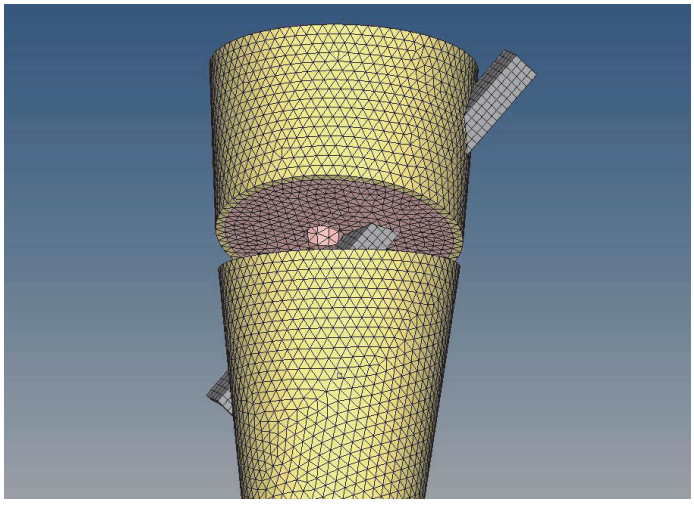

Figure 4.5: Finite element mesh for human bone model with thinner cortical layer

The elastic modulus of healthy cortical and cancellous bone is known to be approximately 17 GPa and 1.3 GPa, respectively. However, most patients who experience a distal radius fracture suffer from osteoporosis and are expected to have poorer bone properties. A number of density-modulus relationships have been presented in the literature for patient specific FEA. One particular relationship that has been proposed for the distal ulna is $E=8346\rho^{1.5}$ (MPa), where density (ρ) is in grams per cubic centimeter (Austman et al., 2009). Based on this relationship, the elastic modulus for cortical and cancellous bone were estimated from the densities reported by Neilson et al. Table 4.2 shows the final properties that were applied to the finite element model.

Table 4.2: Material properties of human bone used for FEA

Type of Bone	Elastic Modulus (GPa)	Density (g/cc)	Poisson's Ratio
Cortical	8.35	1.0	0.3
Cancellous	0.75	0.20	0.3

The finite element model was used to approximate axial stiffness of the implant in human bone by applying loads of 10, 30, 50, and 70 N and plotting load versus fracture displacement. Axial stiffness was calculated as the slope of a linear trendline fit to the data. To determine if the implant would provide IFS's conducive to bone healing a 110 N compressive load was applied to the model and fracture displacement was reported. IFS was calculated and compared to the maximum strain limit of 15% for new bone formation. To predict whether failure in the bone would occur at or below a load of 110 N, von Mises stress was also evaluated. Previous experimental tests conducted on the distal region of cadaver radii have shown the ultimate strength of bone to be 24 MPa (MacNeil et al., 2008). The von Mises yield criterion was used to determine whether failure was evident in the finite element model under simulated physiological loads.

4.3 Results

4.3.1 Foam Cortical Shell Sawbone Model

The FCS sawbone model was computed at loads of 5, 10, 20, 30, and 40 N. As shown in Figure 4.6, the numerical axial stiffness was found to be 49.55 N/mm. Figure 4.7 displays the difference between experimentally and numerically calculated axial stiffness. As shown, the numerical stiffness was found to be within the 90% confidence interval for true axial stiffness calculated from the experimental data. An error of 10.9% was found when comparing the sample mean of 44.67 N/mm for experimental stiffness to the numerical result. Based on the sample mean for experimental stiffness, the mean difference in magnitude between numerical and experimental displacements was calculated as 0.0548 mm (17.7%) as shown in Table 4.3.

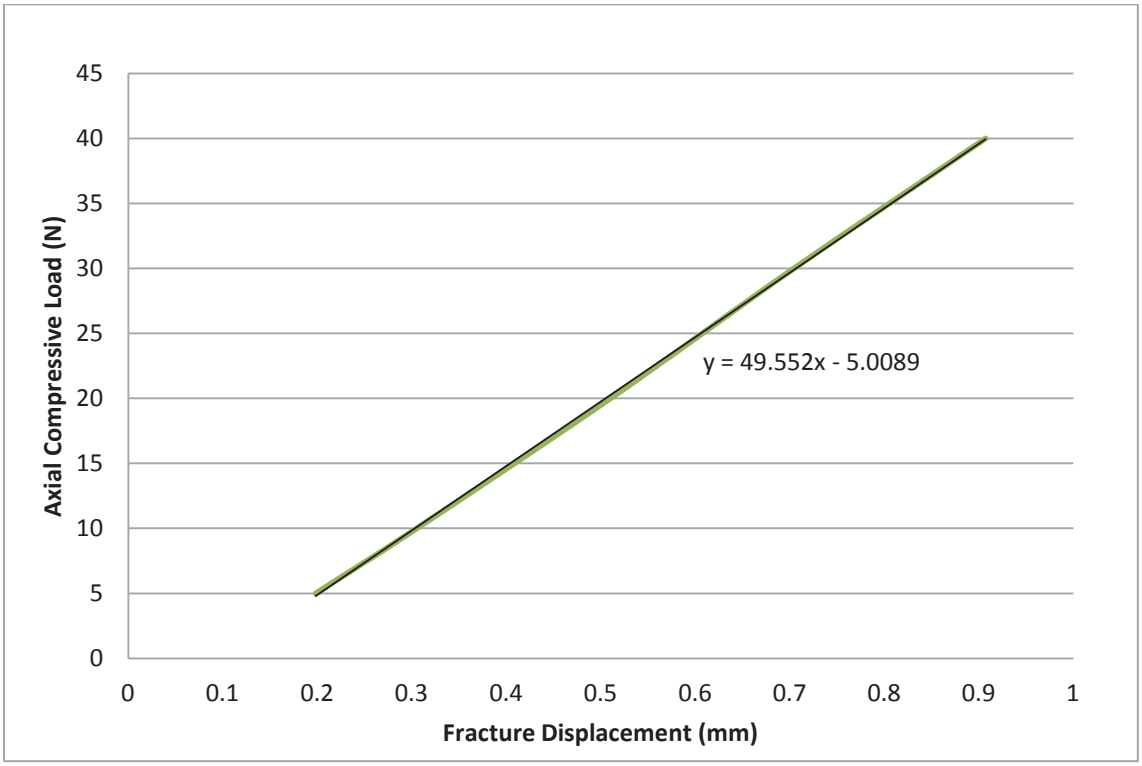

Figure 4.6: Numerical fracture displacement versus load for FCS sawbone model

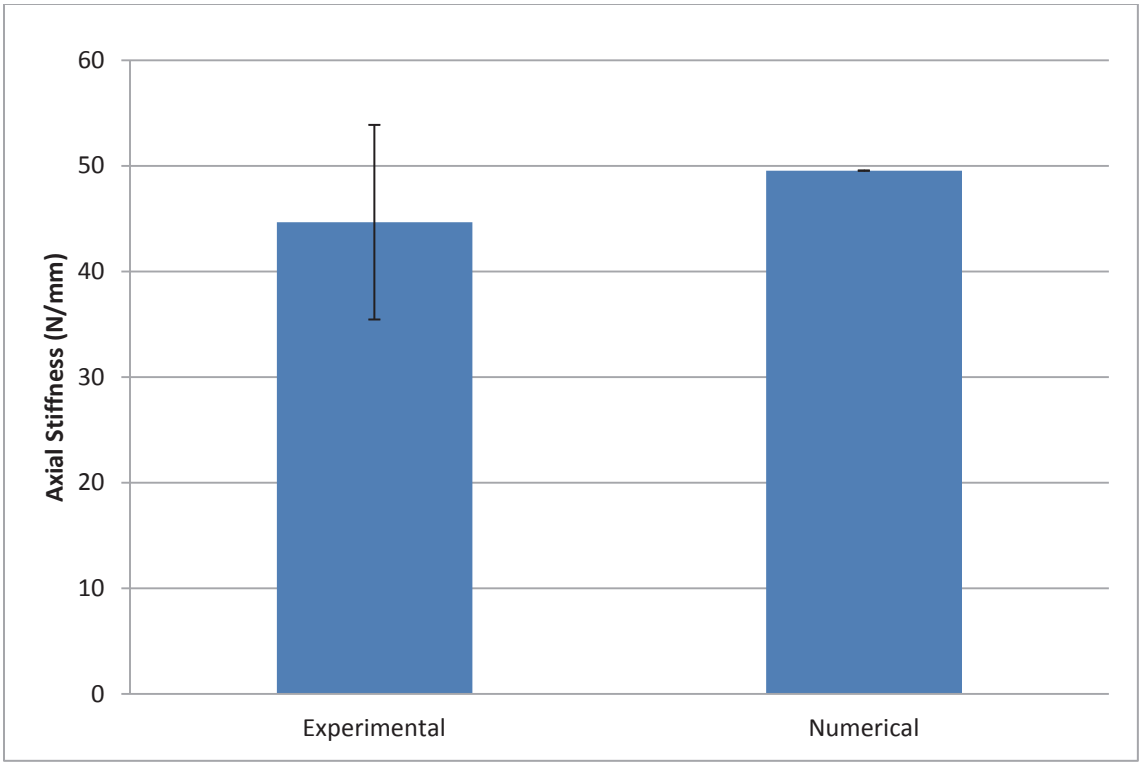

Figure 4.7: Experimental (with 90% confidence interval) versus numerical axial stiffness

Table 4.3: Mean experimental displacement versus numerical displacement for FCS model

Load (N)	Experimental Displacement (mm) =Load/44.67 N/mm	Numerical Displacement (mm)	Difference (mm)	Difference (%)
5	0.1119	0.1980	0.0861	43.5
10	0.2239	0.3049	0.0810	26.6
20	0.4477	0.5099	0.0622	12.2
30	0.6716	0.7043	0.0327	4.64
40	0.8955	0.9073	0.0118	1.30
		Mean Difference	**0.0548 mm**	**17.7 %**

Von Mises stress was evaluated at each of the five loads. Figure 4.8 shows the maximum von Mises stress in the cancellous and cortical bone plotted versus load. Based on the compressive yield strength of 2.2 MPa for the cancellous foam core, failure of this material would be expected at 20 N of load. Stress in the cortical shell was found to be 4.22 MPa at 30 N of load, which is representative of the mean experimental failure strength. This is below the compressive yield strength of 8.4 MPa defined for the material. Given that materials were modeled as linearly elastic, stress in the cortical shell is expected to be higher than reported numerically following failure of the cancellous foam core. If the cancellous foam core were to fail at 20 N, additional load would be transferred through the cortical shell. Figure 4.9 shows a von Mises stress plot at 30 N and it is evident that the areas of high stress are at the implant/bone interface. This result indicates that the finite element model is capable of predicting the mode of failure and the approximate failure strength. More accurate material modeling would be required to precisely calculate failure loads.

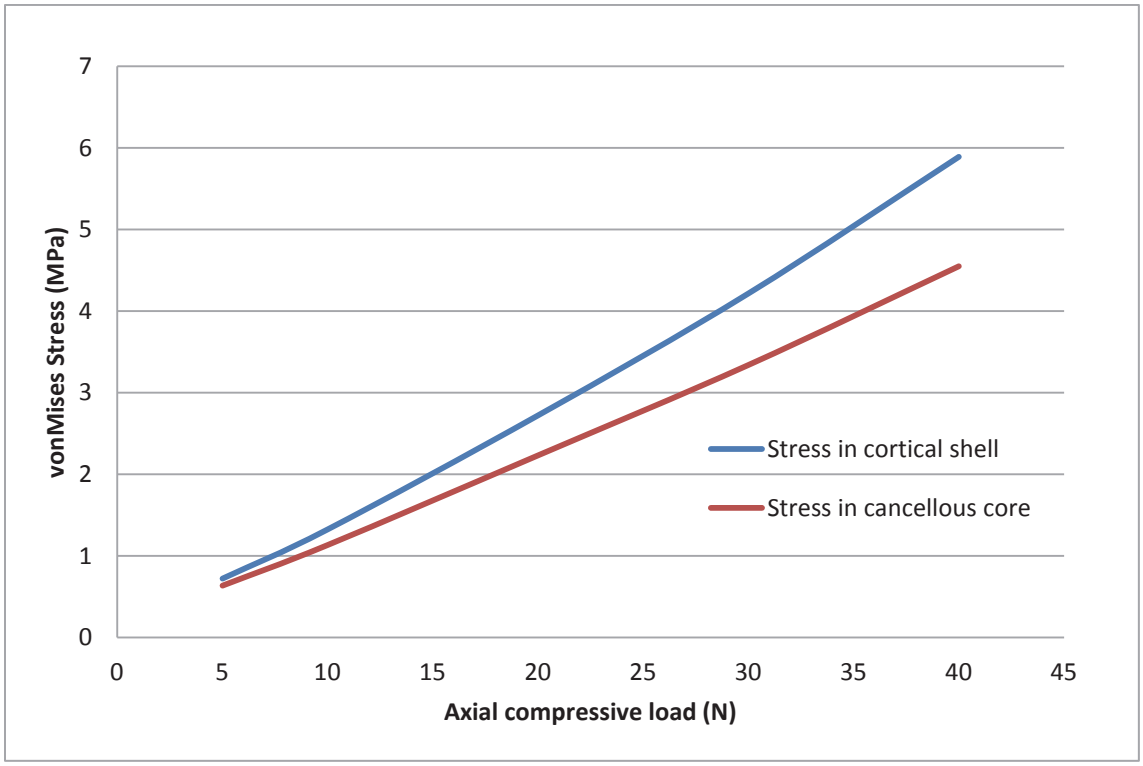

Figure 4.8: Maximum von Mises stress in cortical and cancellous bone in FCS sawbone model

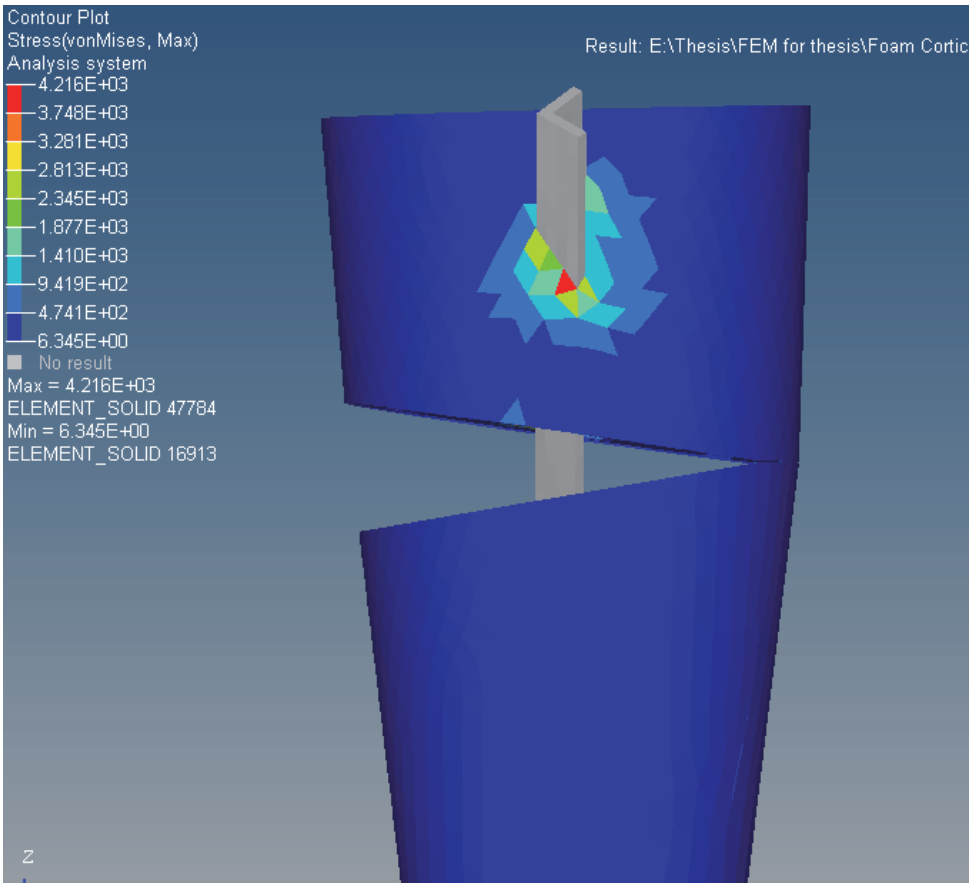

Figure 4.9: von Mises stress (kPa) contour plot under 30 N load in FCS sawbone model

4.3.2 Composite Sawbone Model

The composite sawbone model was computed at loads of 10, 30, 70, 90, and 110 N. The magnitude of the numerical displacement was plotted versus load and compared to experimental sample #13 as shown in Figure 4.10. The numerical axial stiffness was found to be 281.62 N/mm. The experimental stiffness for sample #13 was 189.84 N/mm initially, before decreasing to 98.74 N/mm at approximately 40 N of load. This translates to a 32.6% error in stiffness initially, and 64.9% following the decrease in stiffness. The lower value for experimental stiffness was attributed to the inability of the implant to penetrate the cortical shell of composite sawbones. The finite element model simulates a rigid fixation of the implant in the medial cortex. This could not be achieved experimentally because of the hardness of the cortical shell material. Without fixation in the medial cortex the implant relies heavily on fixation in the cancellous foam core. This is likely to result in a lower stiffness, and once the cancellous foam core begins to fail, a

decrease in stiffness would be expected as shown. Further experimental testing would be beneficial to more accurately quantify stiffness in composite sawbones.

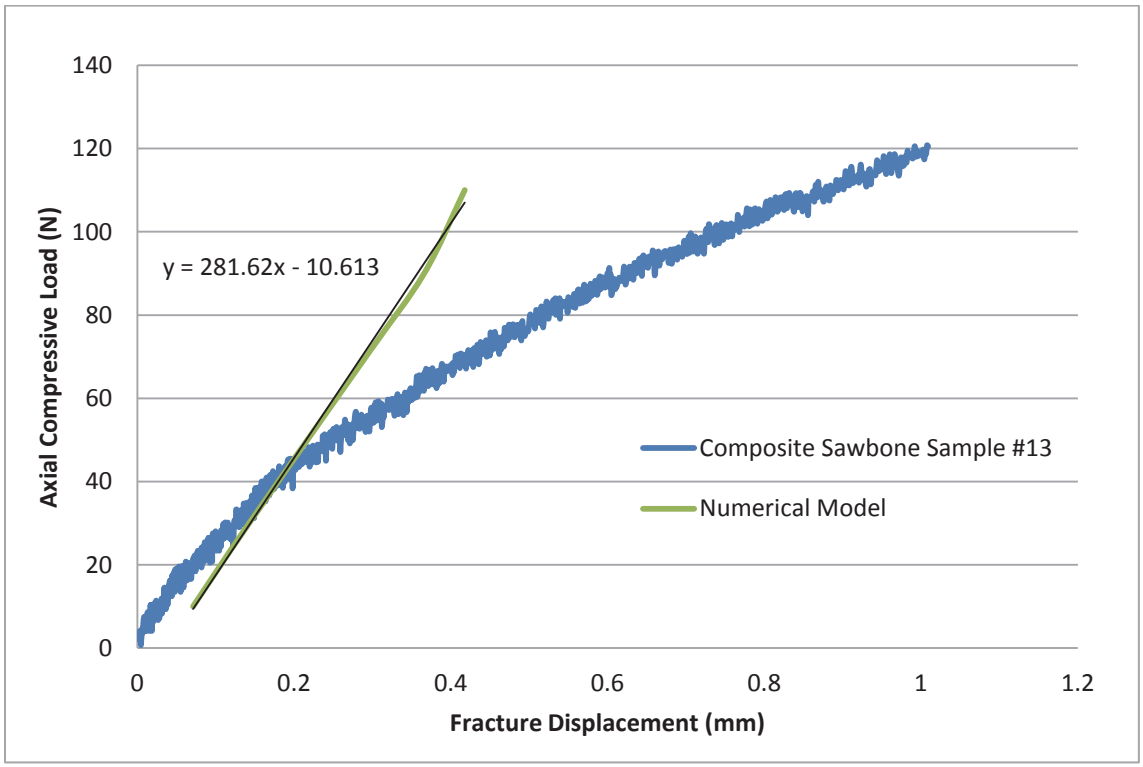

Figure 4.10: Experimental versus numerical displacement for composite sawbone model

Von Mises stress was evaluated to determine the mode of failure predicted by the finite element model. The failure strength of sample #13 was 105 N and was caused by a combination of failure in the cancellous foam core and implant bending. At a load of 110 N the maximum von Mises stress in the implant was calculated to be 216 MPa as shown in Figure 4.11. This exceeds the yield strength of 205 MPa defined for stainless steel 316L. The maximum von Mises stress in the cortical and cancellous bone at this load was 55.29 MPa and 6.47 MPa, respectively. The stress in the cancellous bone exceeds its yield strength of 6.0 MPa; however, the stress in the cortical bone is well below its yield strength of 157 MPa. Based on these values it can be assumed from the finite element model that failure will occur in the implant as well as in the cancellous foam core. Similar to the FCS sawbone model, the composite sawbone model is able to predict mode of failure and the approximate failure load. Again, further experimental testing would be

beneficial to more accurately quantify experimental failure strength in composite sawbones.

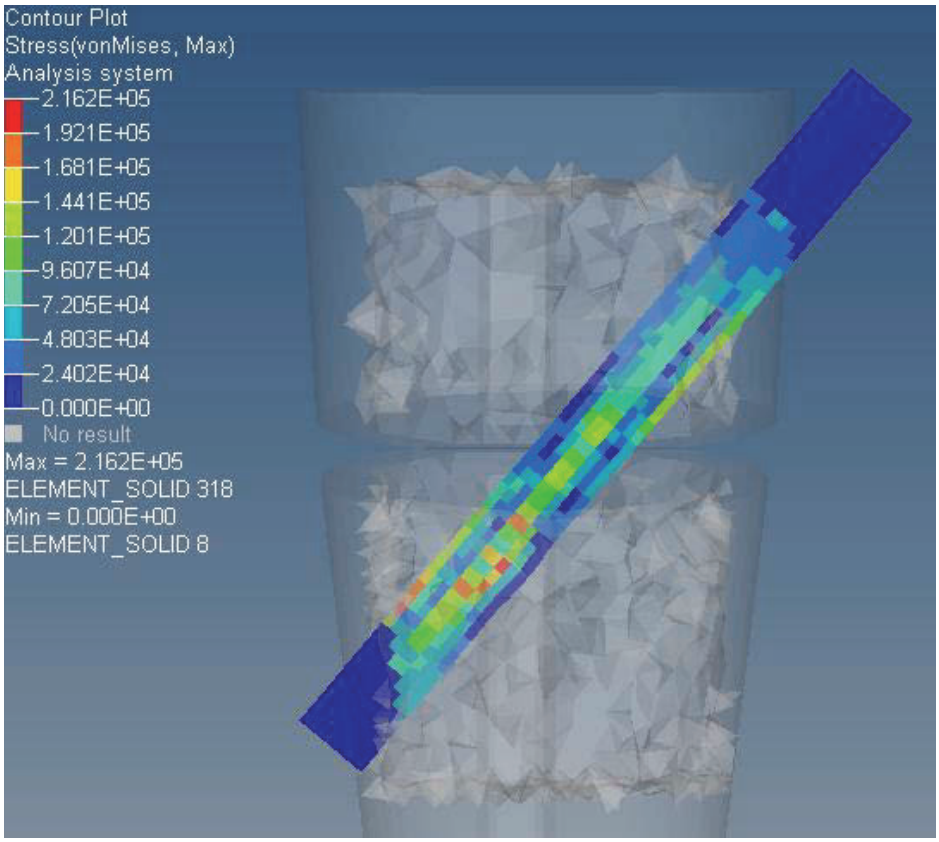

Figure 4.11: von Mises stress (kPa) contour plot under 110 N load in composite sawbone model

4.3.3 Human Bone Model

The human bone model was computed at loads of 10, 30, 50, 70 and 110 N. As shown in Figure 4.12, the axial stiffness was found to be 218.53 N/mm. The displacement at the dorsal center of the fracture under 110 N of load was calculated as 0.5295 mm. Based on this value, IFS in human bone under simulated physiological loads would be approximately 5.3%. This is within the desired range for new bone formation. However, as shown in Figure 4.13 the maximum von Mises stress in the cortical bone reaches 25.85 MPa at a load of 70 N. This exceeds the ultimate strength of 24 MPa previously reported in the literature for cadaver radii. Therefore, it can be assumed that failure will occur in the bone at a load of approximately 70 N.

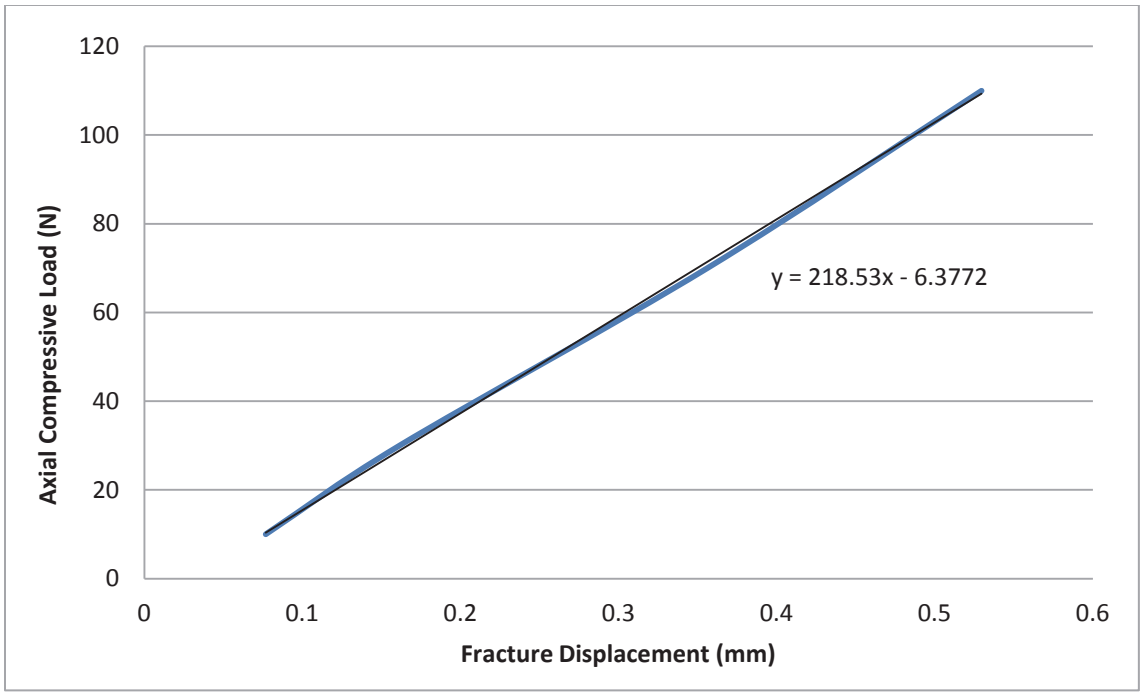

Figure 4.12: Numerical fracture displacement for human bone model

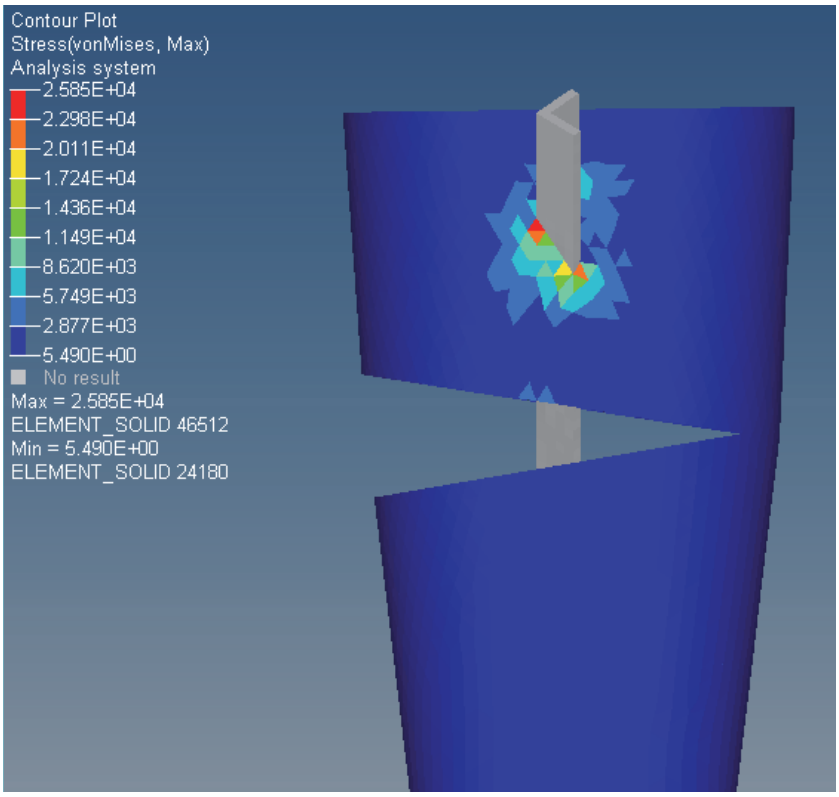

Figure 4.13: von Mises stress (kPa) contour plot under 70 N load in human bone model

4.4 Discussion

Results from the sawbone models showed good correlation with experimental results for calculating fracture displacement within the elastic region. The FCS sawbone model had a numerical axial stiffness of 49.55 N/mm compared to a mean experimental stiffness of 44.67 N/mm. The numerical stiffness was within the 90% confidence interval for stiffness calculated from experimental data and had only a 10.9% error compared to the mean experimental stiffness. The composite sawbone model had a numerical axial stiffness of 281.62 N/mm compared to an experimental stiffness of 189.84 N/mm. The experimental stiffness decreased to 98.74 N/mm at approximately 40 N of load. The difference in stiffness between the numerical and experimental models was attributed to the inability of the implant to penetrate the medial cortex of the composite sawbones. This is likely to have caused a lower experimental stiffness. Further experimental testing is recommended to more accurately quantify stiffness in composite sawbones.

The magnitude of displacements calculated by the FCS sawbone model was roughly 0.05 mm greater than experimentally measured displacements. This error may be attributed to the friction model that was used to define contact between the implant and bone. It is possible that the static coefficient of friction was underestimated in the sawbone models resulting in greater initial displacements numerically. The friction model was selected to be optimized for human bone. Considering the simplifications made to the finite element model an error of 0.05 mm is not significant. Based on these results the finite element model can be considered valid for approximating fracture displacement within the elastic range. The numerical model also confirms the validity of the previously collected experimental data.

The von Mises yield criterion was used to predict failure modes and failure strengths in both numerical sawbone models. The mean experimental failure strength in the foam cortical sawbones was found to be 30.5 N. Failure occurred in the rigid polyurethane foam shell at the implant/bone interface resulting in implant loosening. To assess this mode of failure numerically the maximum von Mises stress in the bone was reported at an axially applied load of 30 N. The maximum von Mises stress in the cortical bone was located at the implant/bone interface and was calculated to be 4.22 MPa. This

value is below the suggested compressive yield strength of 8.4 MPa reported for the material. One reason for the numerical von Mises stress being lower than the yield strength is due to the linearly elastic material model selected for FEA. The use of a linearly elastic material model allowed stress in the cancellous bone to exceed its yield strength at a load of 30 N. The maximum von Mises stress in the cancellous bone at 30 N was calculated as 3.34 MPa, which is greater than its yield strength of 2.2 MPa. If a non-linear material model was used the cancellous bone would have failed at approximately 20 N resulting in higher stresses in the cortical bone at a load of 30 N. Also, the finite element mesh was optimized for calculating displacement, so it is possible that higher stresses may be calculated if the mesh size was reduced.

The experimental failure strength for composite sawbone sample #13 was 105 N and occurred through a combination of failure in the cancellous foam core and implant bending. The finite element model predicted the von Mises stress in the implant and cancellous bone to surpass their yield strengths at approximately 110 N. At this load, stress in the cortical bone was not expected to exceed its material yield strength. This confirms that the model is able to correctly predict failure modes.

Based on the material properties reported in the literature, it is apparent that the properties of a human radius are somewhere in between those of FCS sawbones and composite sawbones. FEA found the implant to provide an axial stiffness of 218.53 N/mm in simulated human bone. As expected, the numerical stiffness in human bone is greater than in FCS sawbones and less than in composite sawbones. The calculated IFS under expected physiological loading was 5.3%, which is considered to be conducive to bone healing. However, the maximum von Mises stress in the bone at 70 N of load was calculated to be 25.85 MPa. This is greater than previously reported ultimate strengths for cadaver radii. Therefore, despite an optimal IFS rate, failure would be expected in the bone below anticipated physiological loads.

4.4.1 Limitations

The major limitation of this FEA was the use of an isotropic, linearly elastic material model. This prevented accurate prediction of failure strengths. It is possible to define material models to include in-homogeneities, visco-elasticity, non-linearity, and

anisotropic properties. In order to accurately implement these complex material models a significant amount of experimental data is required. Non-linear models can be defined using a variety of failure criterions and are often based off experimental stress-strain curves. A non-linear model would help improve the ability to predict failure loads. Isotropic material properties are considered adequate for modeling sawbones; however, accurately modeling human bone is more difficult due to its orthotropic properties. In order to determine these directionally dependent properties a large quantity of experimental data would need to be acquired. Based on the scope of this thesis, an isotropic, linearly elastic material model was considered to provide sufficiently accurate results while reducing computational costs.

An additional limitation of this FEA was the simplifications made to the geometric model. The geometry of the radius was simplified based on the dimensions of the synthetic radii. The bone was modeled as a tapered cylinder with a flat radial joint surface and without any complex surface contours. Furthermore, the sharp cutting edge on the implant was not included in the model. This was compensated for by constraining the distal end of the implant simulating a rigid fixation. Although this is believed to be a reasonable assumption, modeling the sharp tip and defining a contact with the bone would improve accuracy. In order to minimize the impact of the simplified geometry on the numerical results, the contact area between the implant and bone was carefully matched to the experimental samples.

The geometry of the model could be improved by using 3D laser scanning technology to obtain an accurate CAD model of a radius. Also, many previous finite element studies have used CT scans to create patient specific numerical models. This allows material properties to be more accurately defined using a density-modulus relationship, which can account for variability in bone density. For the human bone model in this analysis, material properties were chosen to best represent a typical patient. This could be improved by using CT scans from an actual patient to recreate a true human bone model.

4.4.2 Conclusion

FEA of the novel implant showed good correlation with *in vitro* testing results. The finite element model was validated against experimental testing on both FCS sawbones and composite sawbones, although further experimental testing is recommended on composite sawbones to more accurately characterize stiffness and failure strength. The valid model was used to estimate implant efficacy in human bone under simulated physiological loading. It was determined that treatment with the implant will cause failure in human bone below anticipated physiological loads during the early stages of healing.

CHAPTER 5 CONCLUSIONS & RECOMMENDATIONS

5.1 Conclusion

This thesis was intended as a biomechanical investigation of a novel implant for the stabilization of distal radius fractures. A novel implant was designed that could successfully be implanted using a minimally invasive surgical approach. Surgical instrumentation was designed to facilitate the procedure in a controlled manner. The goal was to develop a cost effective, minimally invasive treatment method that would permit early mobilization of the hand and wrist. However, results from experimental and numerical testing found the stabilization provided by the novel implant to be insufficient for allowing an early return to function.

In vitro experimental testing on FCS sawbones showed that the novel implant fails well below anticipated physiological loads. The axial stiffness of the implant was greater than k-wire fixation; however, k-wires had higher failure strength. Failure in the implant group was a result of sawbone material failure at the implant/bone interface causing loosening and fracture collapse. The single point of fixation in combination with a high degree of stiffness mismatch between the implant and bone created high stresses at the interface leading to material failure. Further testing on composite sawbones showed improved axial stiffness and failure strength over FCS sawbones. In composite sawbones implant failure was evident at the low end of expected physiological loads.

A finite element model of the novel implant was successfully validated against *in vitro* testing. The finite element model calculated fracture displacement with good accuracy and was able to predict modes of failure. The valid model was used to approximate implant efficacy in human bone considered to be representative of a typical fracture patient. The results showed that failure would occur in the bone below anticipated physiological loads.

In conclusion, the novel implant was unsuccessful at stabilizing an extra-articular, dorsally comminuted distal radius fracture in a manner that will support new bone formation during an early return to function. Experimental testing showed the implant to

be inferior to k-wire fixation and that neither treatment is capable of providing an early return to function. The novel implant should not be used in clinical practice and fractures should continue to be managed using current treatment methods. If an early return to function is desired, internal fixation with plates and screws is recommended.

5.2 Recommendations for Future Research

Based on the conclusive evidence from this thesis, it is not recommended that additional resources be exhausted on this implant design. The validated finite element model provides a useful and cost effective tool to explore alternative implant designs. The current design was limited because of high stress concentrations at the implant/bone interface. These areas of high stress are the result of poor load distribution due to the small surface area of the implant and having only a single point of fixation. The high stiffness of the implant also contributes to these high stresses. Future design considerations should include reducing the implant stiffness and providing multiple points of fixation. The reason for having a single point of fixation was for simplicity and to reduce procedural costs. As the stiffness is reduced and more points of fixation are included, the treatment becomes more similar to k-wire fixation and potential benefits are lost. Therefore, efforts should be focused on maintaining a single point of fixation for any new implant designs. It may be interesting to re-explore the use of porous foamed metals because of their reduced stiffness. It is possible that a trade-off exists between optimal porosity/stiffness and the ability of the implant to penetrate through bone without failing. This could be achieved by reducing the porosity of the original prototypes to increase their strength, or by manufacturing an implant with a thin solid core and a porous outer surface. It would also be valuable to explore the use of titanium alloys as they are known to have a lower modulus and higher yield strength compared to stainless steel.

It is recommended that any new design concepts are first evaluated using the finite element model prior to manufacturing prototypes and performing experimental tests. This may include refinement of the finite element model to improve geometry and incorporate orthotropic, non-linear material models. The finite element model can also be used as a tool to simulate different types of fractures and their influence on implant efficacy.

Aside from the implant, the design of a traction device that rests on a c-arm fluoroscopy unit is a novel approach to performing a closed reduction. The PCT application that was filed covers the intellectual property of this device. It is possible that this traction device may add value to current surgical procedures such as k-wire fixation or external fixation, which both require a closed reduction. Future research and investigation into the efficacy of this traction device may be of value. If pursued, it is recommended that the concept of performing surgery directly on a c-arm first be validated as a practical surgical technique. The next steps would involve design refinements and manufacturing of a beta prototype.

BIBLIOGRAPHY

AAOS. (2009). The Treatment of Distal Radius Fractures Guideline and Evidence Report. *AAOS*, (December 5).

AAOS Now. (2009). Chicago (IL): American Academy of Orthopaedic Surgeons.

Anderson, D. D., Deshpande, B. R., Daniel, T. E., & Baratz, M. E. (2005). A three-dimensional finite element model of the radiocarpal joint: distal radius fracture step-off and stress transfer. *The Iowa Orthopaedic Journal*, *25*, 108-117.

Anzarut, A., Johnson, J. a, Rowe, B. H., Lambert, R. G. W., Blitz, S., & Majumdar, S. R. (2004). Radiologic and patient-reported functional outcomes in an elderly cohort with conservatively treated distal radius fractures. *The Journal of hand surgery*, *29*(6), 1121-1127.

AO Foundation (1958-2012). Transforming Surgery – Changing Lives. Retrieved June 20, 2012 from: https://www.aofoundation.org/Structure/Pages/default.aspx

Arbenz, P., Lenthe, G. H. V., Mennel, U., & M, R. (2007). Multi-level μ-Finite Element Analysis for Human Bone Structures. *PARA 2006, LNCS 4699* (pp. 240-250).

Aro, H T, and E Y Chao. (1993). Biomechanics and biology of fracture repair under external fixation. *Hand clinics, 9*(4), 531-542.

Augat, P., Iida, H., Jiang, Y., Diao, E., & Genant, H. K. (1998). Distal Radius Fractures : Mechanisms of Injury and Strength Prediction by Bone Mineral Assessment. *Journal of Orthopaedic Research*, *16*, 629-635.

Austman, R. L., Milner, J. S., Holdsworth, D. W., & Dunning, C. E. (2009). Development of a customized density–modulus relationship for use in subject-specific finite element models of the ulna. *Journal of Engineering in Medicine*, *223*(6), 787-794.

Azzopardi, T., Ehrendorfer, S., Coulton, T., & Abela, M. (2005). Unstable extra-articular fractures of the distal radius a prospective, randomised study of immobilisation in a cast versus supplementary percutaneous pinning. *The Journal of Bone and Joint Surgery*, *87*, 837-840.

Beil, F. T., Barvencik, F., Gebauer, M., Mumme, M., Beil, B., Pogoda, P., Rueger, J. M., et al. (2011). The distal radius, the most frequent fracture localization in humans: a histomorphometric analysis of the microarchitecture of 60 human distal radii and its changes in aging. *The Journal of trauma*, *70*, 154-158.

Beumer, A., & McQueen, M. M. (2003). Fractures of the distal radius in low-demand elderly patients: closed reduction of no value in 53 of 60 wrists. *Acta orthopaedica Scandi*, *74*(1), 98-100.

Board, T., Kocialkowski, A., & Andrew, G. (1999). Does Kapandji wiring help in older patients? A retrospective comparative review of displaced intra-articular distal radial fractures in patients over 55 years. *Injury, Int. J. Care Injured*, *30*, 663-669.

Boutroy, S., Rietbergen, B. V., Sornay-rendu, E., Munoz, F., Bouxsein, M. L., Delmas, P. D., & Bmd, A. (2008). Finite Element Analysis Based on *In vivo* HR-pQCT Images of the Distal Radius Is Associated With Wrist Fracture in Postmenopausal Women. *Journal of Bone and Mineral Research*, *23*(3), 392-399.

Brogren, E., Petranek, M., & Atroshi, I. (2007). Incidence and characteristics of distal radius fractures in a southern Swedish region. *BMC musculoskeletal disorders*, *8*, 48.

Carter DR, Hayes WC. (1977). The compressive behavior of bone as a two-phase porous structure. *Journal of Bone and Joint Surgery, 59A*, 954–962.

Cheng, H.-Y. K., Lin, C.-L., Lin, Y.-H., & Chen, A. C.-Y. (2007). Biomechanical evaluation of the modified double-plating fixation for the distal radius fracture. *Clinical Biomechanics*, *22*, 510-517.

Cherubino, P., Bini, A., & Marcolli, D. (2010). Management of distal radius fractures: Treatment protocol and functional results. *Injury, Int. J. Care Injured*, *41*, 1120-1126.

Chung, K. C., Shauver, M. J., & Birkmeyer, J. D. (2009). Trends in the United States in the Treatment of Distal Radial Fractures in the Elderly. *The Journal of Bone and Joint Surgery*, *91*, 1868-1873.

Claes, L. E., Heigele, C. a, Neidlinger-Wilke, C., Kaspar, D., Seidl, W., Margevicius, K. J., & Augat, P. (1998). Effects of mechanical factors on the fracture healing process. *Clinical orthopaedics and related research*, (355S), S132-47.

Colles, A. (1814). The classic. On the fracture of the carpal extremity of the radius. Abraham Colles, Edinburgh Med. Surg. J., 1814. *Clinical orthopaedics and related research*, *83*, 3-5.

Cooney WP. (1993). Fracture of the distal radius. A modern treatment-based classification. *Orthop Clin, 24(2),* 211-212.

Cooney III, W.P., Linscheid, R.L., Dobyns, J.H., (1991). Fractures and dislocations of the wrist. *Rockwood and Green's Fractures in Adults*. JB Lippincott Company, Philadelphia, pp. 563-678.

Court-Brown, C. M., & Caesar, B. (2006). Epidemiology of adult fractures: A review. *Injury, Int. J. Care Injured*, *37*, 691-7.

Cömert, A., Kökat, A. M., Akkocaoğlu, M., Tekdemir, I., Akça, K., & Cehreli, M. C. (2009). Fresh-frozen vs. embalmed bone: is it possible to use formalin-fixed human bone for biomechanical experiments on implants? *Clinical oral implants research*, *20*, 521-5.

Cristofolini, L, et al. (1996). Mechanical validation of whole bone composite femur models. *Journal of Biomechanics, 29(4),* 525-535.

Dahl, W. J., Nassab, P. F., Burgess, K. M., Postak, P. D., Evans, P. J., Seitz, W. H., Greenwald, a S., et al. (2012). Biomechanical Properties of Fixed-Angle Volar Distal Radius Plates Under Dynamic Loading. *The Journal of hand surgery*, *xx*, 1-7.

Danis R. (1949) Theortes et Pratique de l'Osteosynthese. Paris: Masson

Diaz-Garcia, R., Oda, T., Shauver, M. J., & Chung, K. C. (2011). A Systematic Review of Outcomes and Complications of Treating Unstable Distal Radius Fractures in the Elderly. *Journal of Hand Surgery*, *36*, 824-835.e2.

Drobetz, H., Schueller, M., Tschegg, E. K., Heal, C., Redl, H., & Muller, R. (2011). Influence of screw diameter and number on reduction loss after plating of distal radius fractures. *ANZ Journal of Surgery*, *81*, 46-51.

Egol, K, Walsh, M., Tejwani, N., Mclaurin, T., Wynn, C., & Paksima, N. (2008). Bridging external fixation and supplementary Kirschner-wire fixation versus volar locked plating for unstable fractures of the distal radius. *The Journal of Bone and Joint Surgery*, *90-B*, 1214-1221.

Egol, Kenneth, Paksima, N., Puopolo, S., Klugman, J., Hiebert, R., & Koval, K. (2006). Treatment of External Fixation Pins About the Wrist : A Prospective, Randomized Trial. *The Journal of Bone and Joint Surgery*, *88-A*(2), 349-355.

Egol, Kenneth a, Kubiak, E. N., Fulkerson, E., Kummer, F. J., & Koval, K. J. (2004). Biomechanics of locked plates and screws. *Journal of orthopaedic trauma*, *18*(8), 488-93.

Fernandez, D. (2000). Should anatomic reduction be pursued in distal radial fractures. *Journal of hand surgery*, *25B*(6), 601-602.

Fernandez, D. L. (2001). Distal radius fracture: the rationale of a classification. *Chirurgie de la main*, *20*, 411-425.

Flinkkilä, T., Sirniö, K., Hippi, M., Hartonen, S., Ruuhela, R., Ohtonen, P., Hyvönen, P., et al. (2010). Epidemiology and seasonal variation of distal radius fractures in Oulu, Finland. *Osteoporosis international*.

Frost & Sullivan, (2003). U.S. Trauma Fixation Market Report.

Frykman, G. (1997). Fracture of the distal radius including sequelae shoulder-hand-finger syndrome, disturbance in the distal radio-ulnar joint and impairment of nerve function. A clinical and experimental study. *Acta Orthop Scand*., *3,* 108S.

Fulkerson, E., Koval, K., Preston, C. F., Iesaka, K., Kummer, F. J., & Egol, K. A. (2006). Fixation of Periprosthetic Femoral Shaft Fractures Associated With Cemented Femoral Stems and Conventional Cable Plates. *Journal of Orthopaedic Trauma*, *20*, 89-93.

Gehrmann, S. V., Windolf, J., & Kaufmann, R. a. (2008). Distal radius fracture management in elderly patients: a literature review. *The Journal of hand surgery*, *33A*, 421-429.

Gliatis, J. D., Plessas, S. J., & Davis, T. R. (2000). Outcome of distal radial fractures in young adults. *Journal of hand surgery*, *25B*(6), 535-543.

Gofton, W., & Liew, A. (2010). Distal radius fractures: nonoperative and percutaneous pinning treatment options. *Hand clinics*, *26*, 43-53.

Hargreaves, D.G., Drew, S.J., Eckersley, R. (2004). Kirschner wire pin tract infection rates: A randomized controlled trial between percutaneous and buried wires. *Journal of Hand Surgery*, *29*, 374-376.

Harley, B. J., Scharfenberger, A., Beaupre, L. A., Jomha, N., & Weber, D. W. (2004). Augmented External Fixation Versus Percutaneous Pinning and Casting for Unstable Fractures of the Distal Radius — A Prospective Randomized Trial. *The Journal of Hand Surgery*, *29A*(5), 815-824.

Hollevoet, N. (2010). Effect of patient age on malunion of operatively treated distal radius fractures. *Acta orthopaedica Belgica*, *76*(6), 743-50.

Jeudy, J., Steiger, V., Boyer, P., Cronier, P., Bizot, P., & Massin, P. (2012). Treatment of complex fractures of the distal radius : A prospective randomised comparison of external fixation " versus " locked volar plating. *Injury, Int. J. Care Injured*, *43*, 173-178.

Johnson A. L., Hulse D.A. (2002) Fundamentals of orthopedic surgery and fracture management. Fossum TW (ed), *Small Animal Surgery.* 2nd ed. St. Louis: Mosby, 855-859.

Jupiter, J. (2012). Future Treatment and Research Directions in Distal Radius Fracture. *Hand Clinics*, *28*, 245-248.

Kaderly, R. E. (1991) Primary bone healing. *Seminars in veterinary medicine and surgery (small animal), 6(1),* 21-25.

Kandemir, U., Matityahu, A., Desai, R., & Puttlitz, C. (2008). Does a volar locking plate provide equivalent stability as a dorsal nonlocking plate in a dorsally comminuted distal radius fracture?: a biomechanical study. *Journal of orthopaedic trauma*, *22*(9), 605-610.

Kannus, P., Niemi, S., Palvanen, M., Parkkari, J., Pasanen, M., Järvinen, M., & Vuori, I. (2001). Continuously rising problem of osteoporotic knee fractures in elderly women: nationwide statistics in Finland in 1970-1999 and predictions until the year 2030. *Bone*, *29*(5), 419-423.

Keast-Butler, O., & Schemitsch, E. H. (2008). Biology versus mechanics in the treatment of distal radial fractures. *Journal of orthopaedic trauma*, *22*(8S), S91-95.

Kilic, A., Ozkaya, U., Kabukcuoglu, Y., Sokucu, S., & Basilgan, S. (2009). The results of non-surgical treatment for unstable distal radius fractures in elderly patients. *Acta orthopaedica et traumatologica turcica*, *43*(3), 229-234.

Klitscher, D., Mehling, I., Nowak, L., Nowak, T., Rommens, P. M., & Müller, L. P. (2010). Biomechanical comparison of dorsal nail plate versus screw and K-wire construct for extra-articular distal radius fractures in a cadaver bone model. *The Journal of hand surgery*, *35A*, 611-618.

Klos, K., Rausch, S., Löffler, M., Fröber, R., Hofmeier, K., Lenz, M., Hofmann, G. O., et al. (2010). A biomechanical comparison of a biodegradable volar locked plate with two titanium volar locked plates in a distal radius fracture model. *The Journal of trauma*, *68*(4), 984-991.

Knight, D., Hajducka, C., Will, E., & McQueen, M. (2010). Locked volar plating for unstable distal radial fractures: clinical and radiological outcomes. *Injury, Int. J. Care Injured*, *41*, 184-189.

Knirk, Jerry; Jupiter, J. (1986). Intra-Articular Fractures of the Distal End of the Radius in Young Adults. *Journal of Bone and Joint Surgery*, *68*(5), 647-659.

Knox, J., Ambrose, H., McCallister, W., & Trumble, T. (2007). Percutaneous pins versus volar plates for unstable distal radius fractures: a biomechanic study using a cadaver model. *The Journal of hand surgery*, *32*(6), 813-817.

Kreder, H. J., Hanel, D. P., Agel, J., Mckee, M., Schemitsch, E. H., & Stephen, D. (2005). Indirect reduction and percutaneous fixation versus open reduction and internal fixation for displaced intra-articular fractures of the distal radius. *The Journal of Bone and Joint Surgery*, *87-B*(6), 829-836.

Krishnan, J., Wigg, A., Walker, R., & Slavotinek, J. (2003). Intra-Articular Fractures of the Distal Radius: A Prospective Randomised Controlled Trial Comparing Static Bridging and Dynamic Non-Bridging External Fixatoin. *Journal of Hand Surgery*, *28B*(5), 417-421.

Kural, C., Sungur, I., Kaya, I., Ugras, A., Ertürk, A., & Cetinus, E. (2010). Evaluation of the reliability of classification systems used for distal radius fractures. *Orthopedics*, *33*(11).

Lafontaine M, Hardy D, Delice P. (1989). Stability assessment of distal radius fractures. *Injury, 20,* 208–210.

Lin, C.-L., Lin, Y.-H., & Chen, A. C.-Y. (2006). Buttressing angle of the double-plating fixation of a distal radius fracture: a finite element study. *Medical & biological engineering & computing*, *44*, 665-673.

Lucas, M., MacBeath, A., McCulloch, E., & Cardoni, A. (2006). A finite element model for ultrasonic cutting. *Ultrasonics*, *44 Suppl 1*, e503-9.

Ludvigsen, T., Johansen, S., Svenningsen, S., & Saetermo, R. (1997). External fixation versus percutaneous pinning for unstable Colles ' fracture Equal outcome in a randomized study of 60 patients. *Acta Orthopaedica Scandinavica*, *68*(3), 255-258.

Macneil, J. a, & Boyd, S. K. (2008). Bone strength at the distal radius can be estimated from high-resolution peripheral quantitative computed tomography and the finite element method. *Bone*, *42*, 1203-1213.

Mann, F A, and J T Payne. (1989). Bone healing. *Seminars in veterinary medicine and surgery (small animal), 4(4),* 312-321.

Martineau, P. A., Waitayawinyu, T., Malone, K. J., Hanel, D. P., & Trumble, T. E. (2008). Volar Plating of AO C3 Distal Radius Fractures : Biomechanical Evaluation of Locking Screw and Locking Smooth Peg Configurations. *Journal of Hand Surgery*, *33A*, 827-834.

Martineau, P. a, Berry, G. K., & Harvey, E. J. (2010). Plating for distal radius fractures. *Hand clinics*, *26*, 61-69.

Mather, B S. (1968). Observations on the effects of static and impact loading on the human femur. *Journal of Biomechanics, 1(4),* 331-335.

Mathiowetz, V, Kashman, N, Volland, G, et al. (1985). Grip and pinch strength: Normative data for adults. *Archives of physical medicine and rehabilitation, 66(2),* 69-74.

Mattila, V., Huttunen, T., Sillanpaa, P., Niemi, S., Pihlajama, H., & Kannus, P. (2011). Significant Change in the Surgical Treatment of Distal Radius: A Nationwide Study Between 1998 and 2008 in Finland. *The Journal of Trauma*, *71*(4), 939-943.

Mcfadyen, I., Field, J., Mccann, P., Ward, J., Nicol, S., & Curwen, C. (2011). Should unstable extra-articular distal radial fractures be treated with fixed-angle volar-locked plates or percutaneous Kirschner wires ? A prospective randomised controlled trial. *Injury, Int. J. Care Injured*, *42*, 162-166.

Mckay, S. D., Macdermid, J. C., Roth, J. H., & Richards, R. S. (2001). Assessment of Complications of Distal Radius Fractures and Development of a Complication Checklist. *The Journal of Hand Surgery*, *26A*(5), 916-922.

Mcqueen, M. M. (1998). Redisplaced unstable fractures of the distal. A randomised, prospective study of bridging versus non-bridging external fixation. *The Journal of Bone and Joint Surgery*, *80-B*, 665-669.

Mehling, I., Müller, L. P., Delinsky, K., Mehler, D., Burkhart, K. J., & Rommens, P. M. (2010). Number and locations of screw fixation for volar fixed-angle plating of distal radius fractures: biomechanical study. *The Journal of hand surgery*, *35A*, 885-891.

Melone, CP Jr. (1984). Articular fractures of the distal radius. *Orthop Clin North Am*., *15,* 217-236.

Millis, D L. (1999). Bone- and non-bone-derived growth factors and effects on bone healing. *The Veterinary clinics of North America. Small animal practice, 29(5),* 1221-1246.

Mizuno K, Mineo K, Tachibana T, et al (1990) The osteogenic potential of fracture hematoma. Subperiosteal and intramuscular transplantation of the hematoma. *Journal of Bone and Joint Surgery, 72(5),* 822-829.

Muller ME. (1991) The principle of the classification. In: Muller ME, Allgower M, Schneider R, Willenegger H, eds. *Manual of Internal Fixation: Techniques Recommended by the AO/ASIF Group*. New York, NY: Springer-Verlag; 118.

Muller, M. E., Webber, C. E., & Bouxsein, M. L. (2003). Predicting the failure load of the distal radius. *Osteoporosis international*, *14*, 345-352.

Naidu, S. H., Capo, J. T., Moulton, M., Ciccone, W., & Radin, A. (1997). Percutaneous pinning of distal radius fractures: a biomechanical study. *The Journal of hand surgery*, *22A*(2), 252-257.

Nellans, K. W., Kowalski, E., & Chung, K. C. (2012). The Epidemiology of Distal Radius Fractures. *Hand Clinics*, *28*, 113-125.

Netter, F., Craig, J., & Machado, C. (2005-2012). Netterimages.com. The Most Trusted Name in Medical Illustration. Retrieved July 5, 2012 from: http://www.netterimages.com/image/36672.htm

Nielsen, S. P., Xie, X., & Barenholdt, O. (2001). Geometric Properties of Distal Radius and Pathogenesis of Colles Fracture. *Journal of Clinical Densitometry*, *4*(3), 209-219.

Orbay, J. L., & Touhami, A. (2006). Current concepts in volar fixed-angle fixation of unstable distal radius fractures. *Clinical orthopaedics and related research*, *445*, 58-67.

Papini, M, et al. (2007). The biomechanics of human femurs in axial and torsional loading: comparison of finite element analysis, human cadaveric femurs, and synthetic femurs. *Journal of biomechanical engineering, 129(1),* 12-19.

Pistoia, W., Lill, C. A., Eckstein, F., Rietbergen, B. V. A. N., Lochmu, E., & Ru, P. (2002). Estimation of Distal Radius Failure Load With Micro-Finite Element Analysis Models Based on Three-dimensional Peripheral Quantitative Computed Tomography Images. *Bone*, *30*(6), 842- 848.

Proceedings of a symposium. (1991). Consensus Development Conference on Osteoporosis. Copenhagen, Denmark. *Am J Med., 91,* 1S-68.

Putnam, M. D., Meyer, N. J., Nelson, E. W., Gesensway, D., & Lewis, J. L. (2000). Distal radial metaphyseal forces in an extrinsic grip model: implications for postfracture rehabilitation. *The Journal of hand surgery*, *25A*, 469-475.

Rahn BA (2002) Bone healing: histologic and physiologic concepts. Fackelman GE (ed), *Bone in Clinical Orthopaedics*. Stuttgart New York: 287-326.

Rancourt D, Shirazi-Adl A, Drouin G, Paiement G. (1990). Friction properties of the interface between porous-surfaced metals and tibial cancellous bone. *J Biomed Mater Res, 24,* 1503–1519.

Roesler, H. (1987). The history of some fundamental concepts in bone biomechanics. *J Biomech,, 20(11),* 1025-1034.

Rogge, R. D., Adams, B. D., & Goel, V. K. (2002). An Analysis of Bone Stresses and Fixation Stability Using a Finite Element Model of Simulated Distal Radius Fractures. *The Journal of Hand Surgery*, *27A*(1), 86-92.

Schemitsch, E. H., Bhandari, M., Boden, S. D., Bourne, R. B., Bozic, K. J., Jacobs, J. J., & Zdero, R. (2010). AOA-COA Symposium: The Evidence-Based Approach in Bringing New Orthopaedic Devices to Market. *The Journal of Bone and Joint Surgery*, *92*, 1030-1037.

Schuind, F., Cooney, W. P., Linscheid, R. L., An, K. N., & Chao, E. Y. S. (1995). Force and Pressure Transmission Through the Normal Wrist. A Numerical Two-Dimensional Study in the Posteroanterior Plane. *Journal of biomechanics*, *28*(5), 587-601.

Shapiro, F. (1988). Cortical Bone Repair. The Relationship of the Lacunar-Canalicular System and Intercellular Gap Junctions to the Repair Process. *The Journal of Bone and Joint Surgery*, *70-A*(7), 1067-1081.

Shauver, M. J., Yin, H., Banerjee, M., & Chung, K. C. (2011). Current and Future National Costs to Medicare for the Treatment of Distal Radius Fracture in the Elderly. *Journal of Hand Surgery*, *36A*, 1282-1287.

Shyamalan, G., Theokli, C., Pearse, Y., & Tennent, D. (2009). Volar locking plates versus Kirschner wires for distal radial fractures — A cost analysis study. *Injury, Int. J. Care Injured*, *40*, 1279-1281.

Sobky, K., Baldini, T., Thomas, K., Bach, J., Williams, A., & Wolf, J. M. (2008). Biomechanical comparison of different volar fracture fixation plates for distal radius fractures. *Hand*, *3*, 96-101.

Sokol, S. C., Amanatullah, D. F., Curtiss, S., & Szabo, R. M. (2011). Biomechanical properties of volar hybrid and locked plate fixation in distal radius fractures. *The Journal of hand surgery*, *36A*, 591-597.

Soong, M., Earp, B. E., Bishop, G., Leung, A., & Blazar, P. (2011). Volar Locking Plate Implant Prominence and Flexor Tendon Rupture. *The Journal of Bone and Joint Surgery*, *93*, 328-335.

Steinburg, B.D., Plancher K.D. (1995). Clinical anatomy of the wrist and elbow. *Clinics in Sports Medicine, 14*(2)*,* 299-313.

Street, J., Winter, D., Wang, J. H., Wakai, A., Mcguinness, A., & Redmond, H. P. (2000). Is Human Fracture Hematoma Inherently Angiogenic? *Clinical orthopaedics and related research*, *378*, 224-237.

Trease, C., McIff, T., & Toby, E. B. (2005). Locking versus nonlocking T-plates for dorsal and volar fixation of dorsally comminuted distal radius fractures: a biomechanical study. *The Journal of hand surgery*, *30A*(4), 756-763.

Varga, P., Baumbach, S., Pahr, D., & Zysset, P. K. (2009). Validation of an anatomy specific finite element model of Colles' fracture. *Journal of biomechanics*, *42*, 1726-1731.

Wall, L. B., Brodt, M. D., Silva, M. J., Boyer, M. I., & Calfee, R. P. (2012). The effects of screw length on stability of simulated osteoporotic distal radius fractures fixed with volar locking plates. *The Journal of hand surgery*, *37A*, 446-453.

Weninger, P., Dall'Ara, E., Leixnering, M., Pezzei, C., Hertz, H., Drobetz, H., Redl, H., et al. (2010). Volar fixed-angle plating of extra-articular distal radius fractures--a biomechanical analysis comparing threaded screws and smooth pegs. *The Journal of trauma*, *69*(5), E46-55.

Wilcke, M. K. T., Abbaszadegan, H., & Adolphson, P. Y. (2011). Wrist function recovers more rapidly after volar locked plating than after external fixation but the outcomes are similar after 1 year. *Acta orthopaedica*, *82*(1), 76-81.

Williams, D. (2003). Revisiting the Definition of Biocompatibility. *Medical Device Technology*, 10-13.

Willis, A., Kutsumi, K., Zobitz, M., & Cooney, W. (2006). Internal Fixation of Dorsally Displaced Fractures of the Distal Part of the Radius. *The Journal of Bone and Joint Surgery*, *88-A*(11), 2411-2417.

Wolfe, SW. (2007). Distal Radius Fractures of the Wrist: Avoiding Complications with Proper Diagnosis and Treatment. *Hospital for Special Surgery*. Retrieved from: http://www.hss.edu/conditions_distal-radius-fractures-of-the-wrist.asp

Wood, A. M., Robertson, G. a, Rennie, L., Caesar, B. C., & Court-Brown, C. M. (2010). The epidemiology of sports-related fractures in adolescents. *Injury, Int. J. Care Injured*, *41*, 834-838.

Young, C. F., Nanu, A. M., & Checketts, R. G. (2003). Seven-Year Outcome Following Colles' Type Distal Radial Fracture. A comparison of Two Treatment Methods. *Journal of Hand Surgery*, *28B*(5), 422-426.

Van der Linden, W., & Ericson, R. (1981). Colles' fracture. How should its displacement be measured and how should it be immobilized? *The Journal of bone and joint surgery, 63,* 1285-1288.

APPENDIX A: Cyclic Experimental Testing Load vs. Displacement Plots

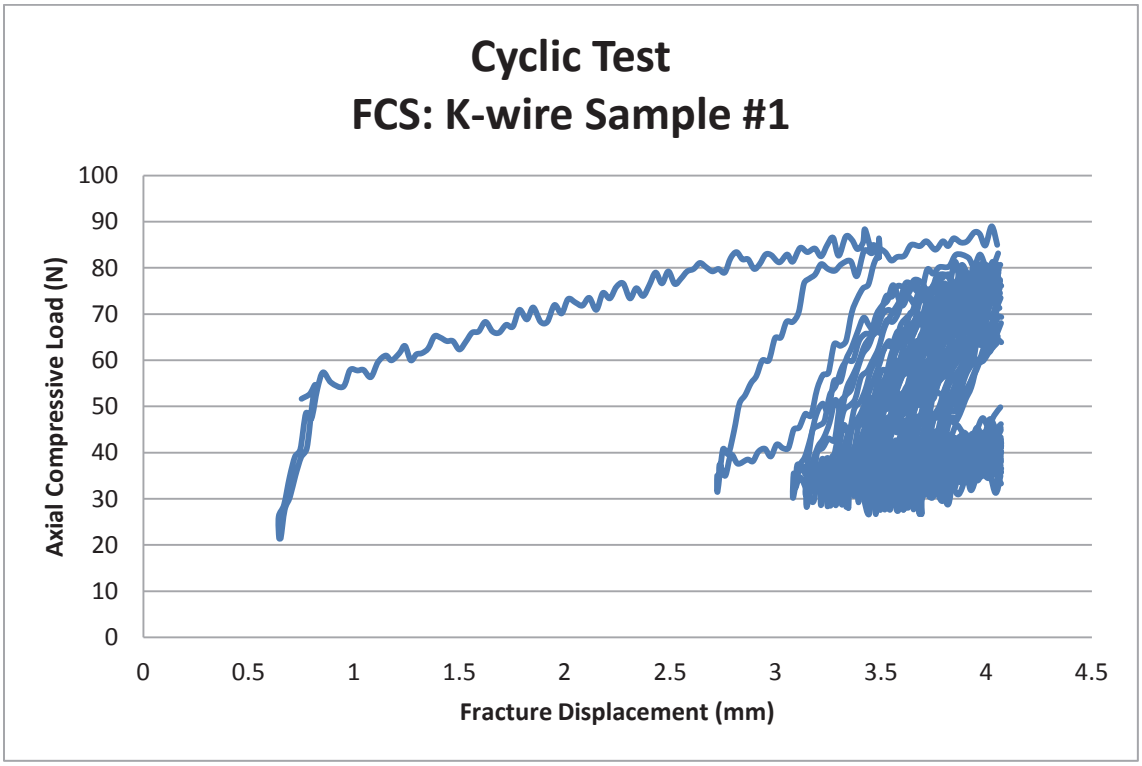

Figure A.1: Cyclic load versus displacement for FCS sawbone k-wire sample #1 This plot shows the first 50 loading cycles. Poor positioning of the LVDT caused it to go out of range beyond 4 mm of displacement. A significant amount of displacement over the first 2 loading cycles was noticed. This is representative of the fractured bone fragment slipping/settling on the k-wires.

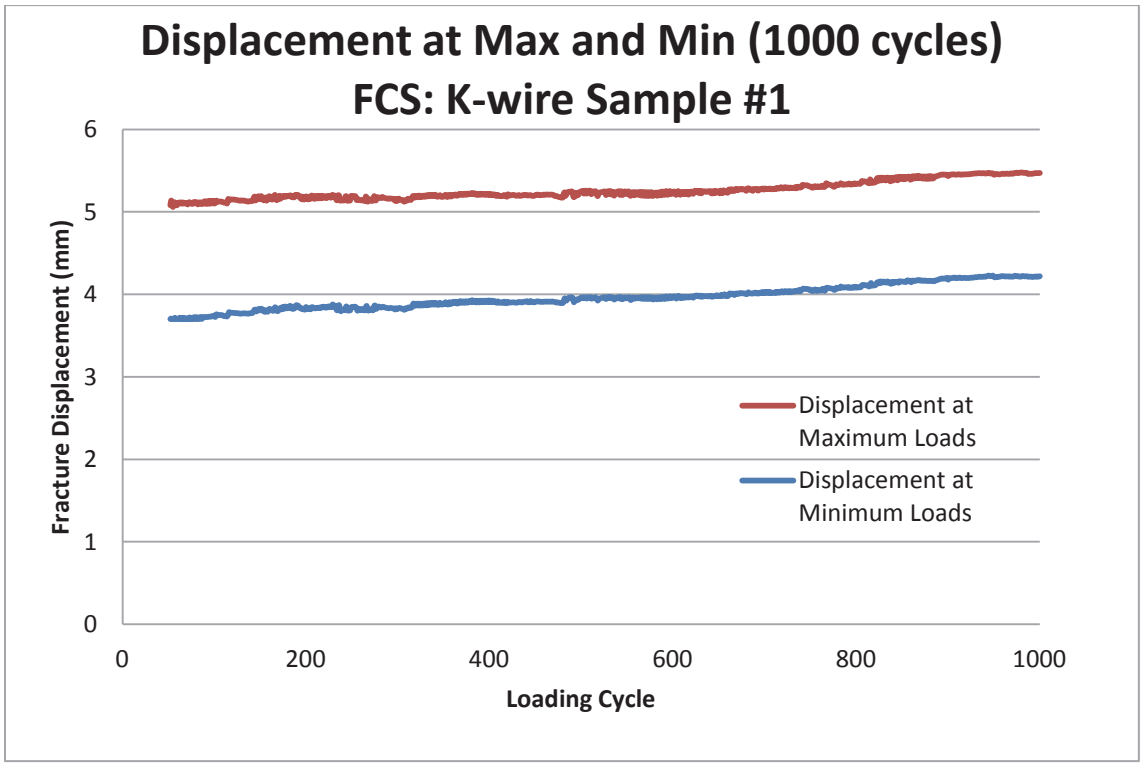

Figure A.2: Displacement at max and min loads for FCS sawbone k-wire sample #1 This plot was used to calculate IFS. The mean value of IFS was found to be 21.44%.

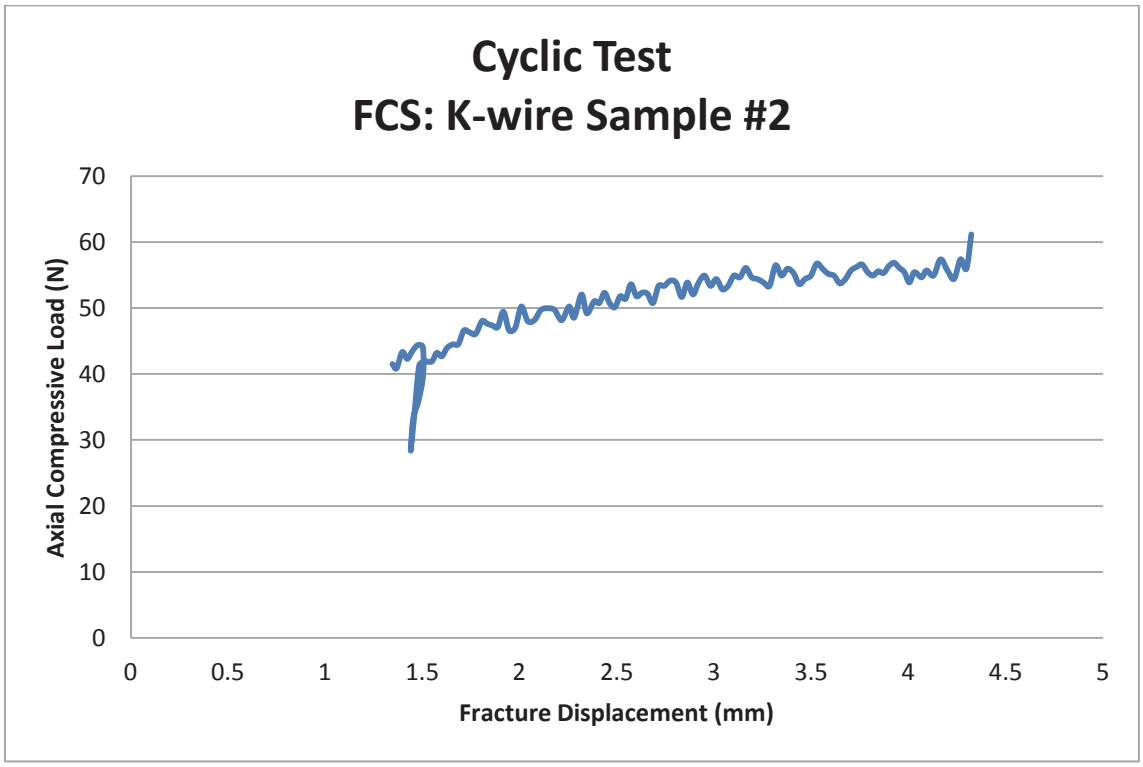

Figure A.3: Cylic load versus displacement for FCS sawbone k-wire sample #2 This plot shows the first loading cycle. It is evident that failure occurred below the maximum experimental load.

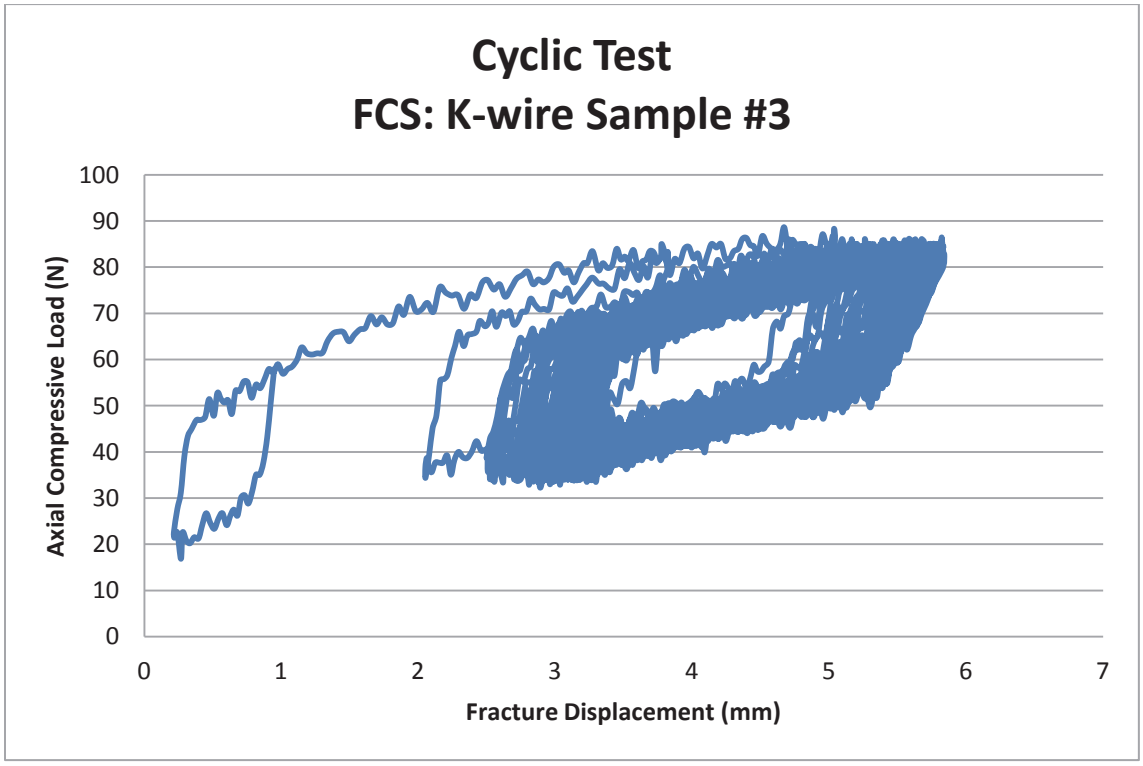

Figure A.4: Cyclic load versus displacement for FCS sawbone k-wire sample #3 This plot shows the first 50 loading cycles. A significant amount of displacement over the first 2 loading cycles was noticed. This is representative of the fractured bone fragment slipping/settling on the k-wires.

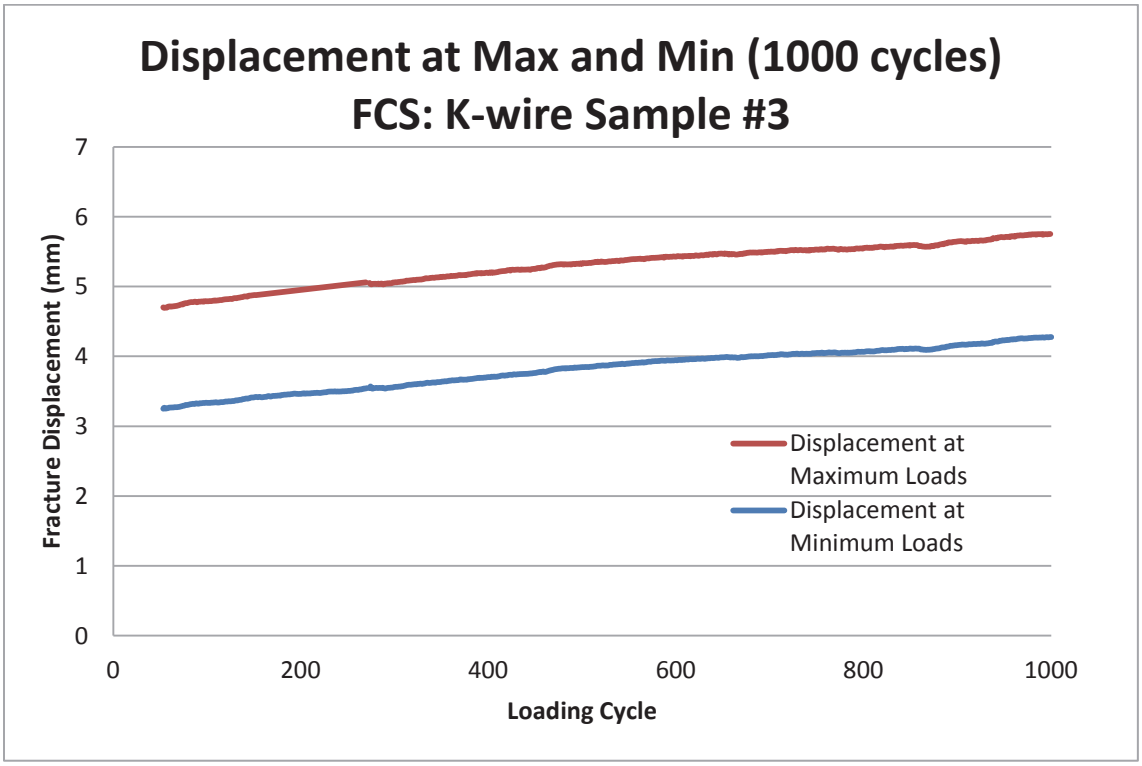

Figure A.5: Displacement at max and min loads for FCS sawbone k-wire sample #3 This plot was used to calculate IFS. The mean value of IFS was found to be 24.03%.

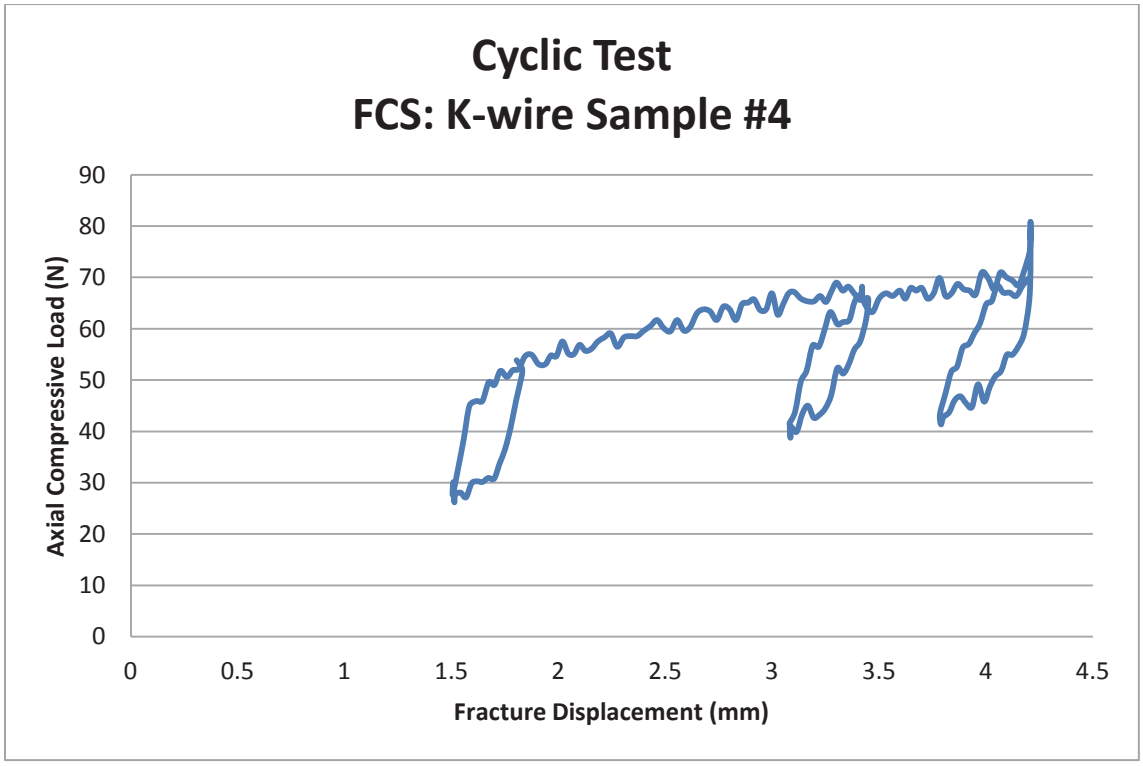

Figure A.6: Cyclic load versus displacement for FCS sawbone k-wire sample #4 This plot shows the first three loading cycles. It is evident that failure occurred below the maximum experimental load.

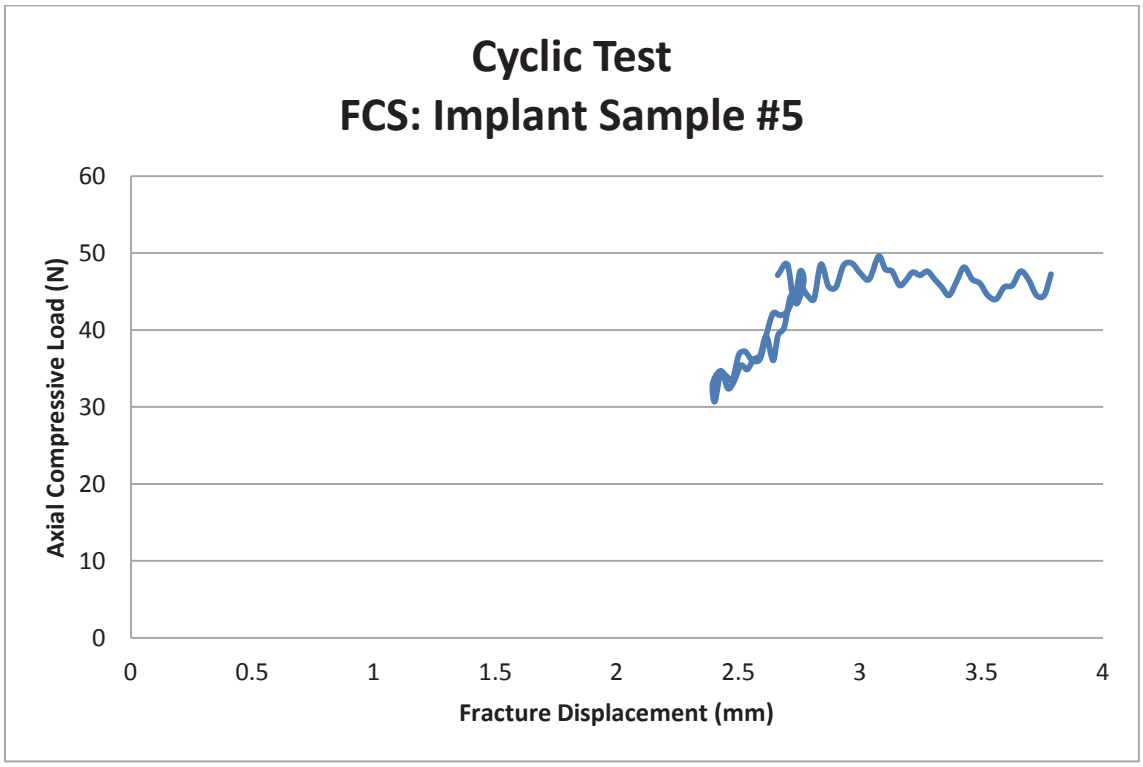

Figure A.7: Cyclic load versus displacement for FCS sawbone implant sample #5 This plot shows the first loading cycle. It is evident that failure occurred below the maximum experimental load.

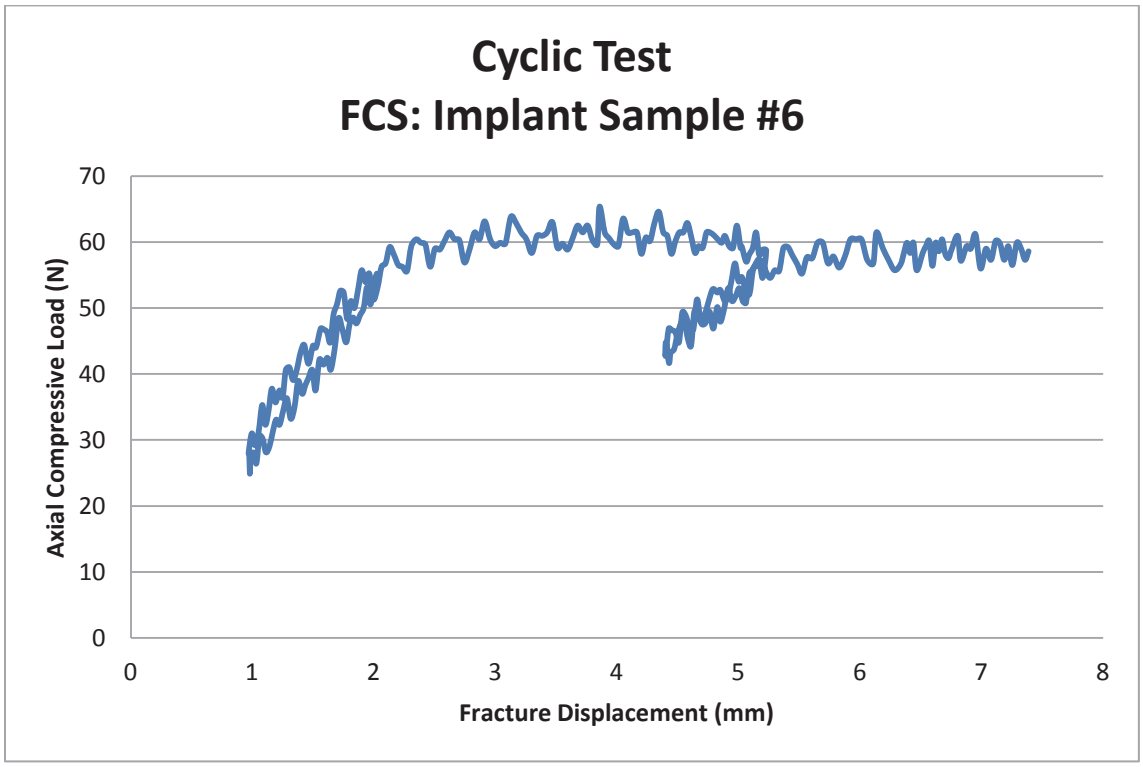

Figure A.8: Cyclic load versus displacement for FCS sawbone implant sample #6 This plot shows the first two loading cycles. It is evident that failure occurred below the maximum experimental load.

APPENDIX B: Quasi-Static Experimental Testing Load vs. Displacement Plots

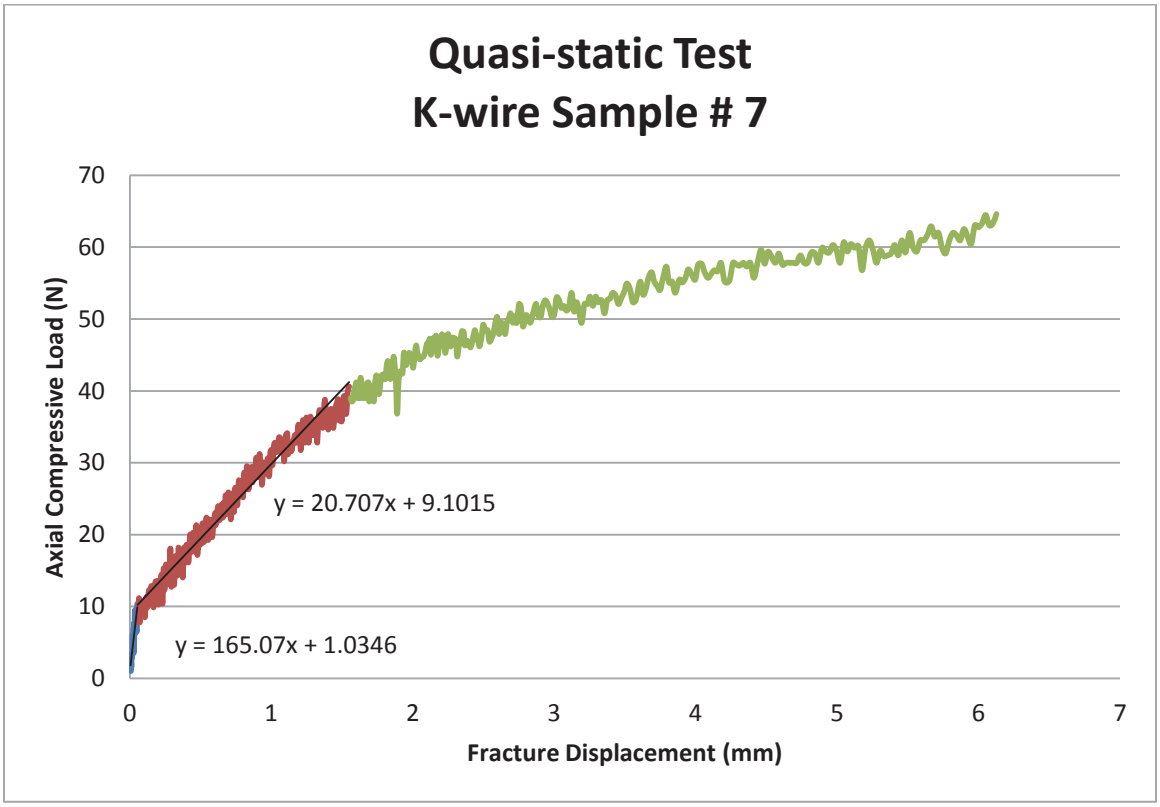

Figure B.1: Quasi-static load versus displacement for FCS sawbone k-wire sample #7 This plot shows the stiffness and failure strength. It is evident that the initial stiffness was 165.07 N/mm prior to the fractured bone fragment slipping/settling on the k-wires. The true axial stiffness was found to be 20.71 N/mm. Failure strength was defined as 40 N.

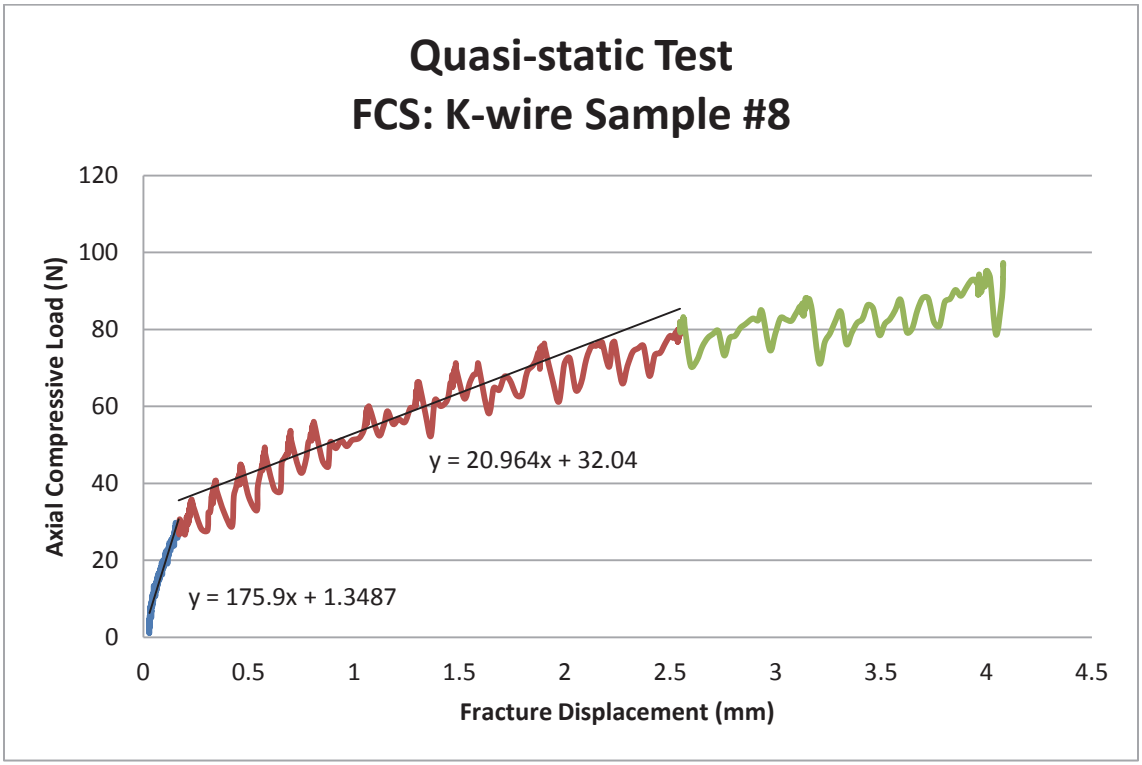

Figure B.2: Quasi-static load versus displacement for FCS sawbone k-wire sample #8 This plot shows the stiffness and failure strength. It is evident that the initial stiffness was 175.90 N/mm prior to the fractured bone fragment slipping/settling on the k-wires. The true axial stiffness was found to be 20.96 N/mm. Failure strength was defined as 85 N.

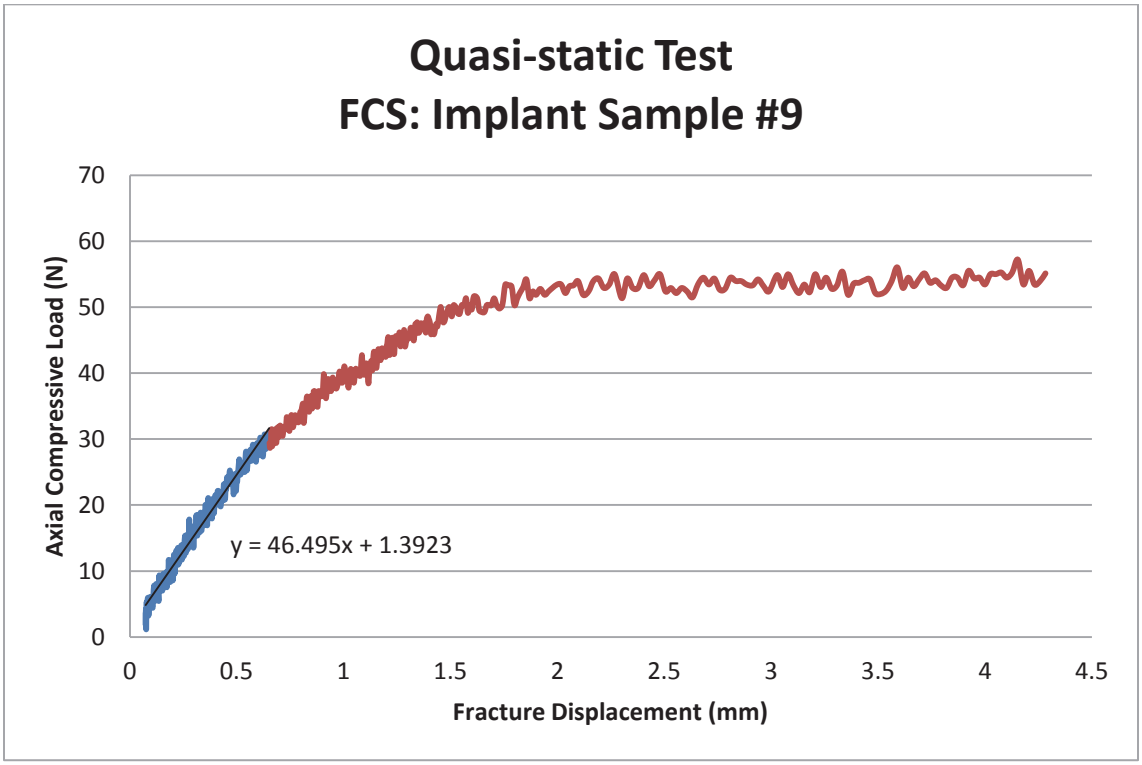

Figure B.3: Quasi-static load versus displacement for FCS sawbone implant sample #9 This plot shows the stiffness and failure strength. The axial stiffness was found to be 46.50 N/mm. Failure strength was defined as 31 N.

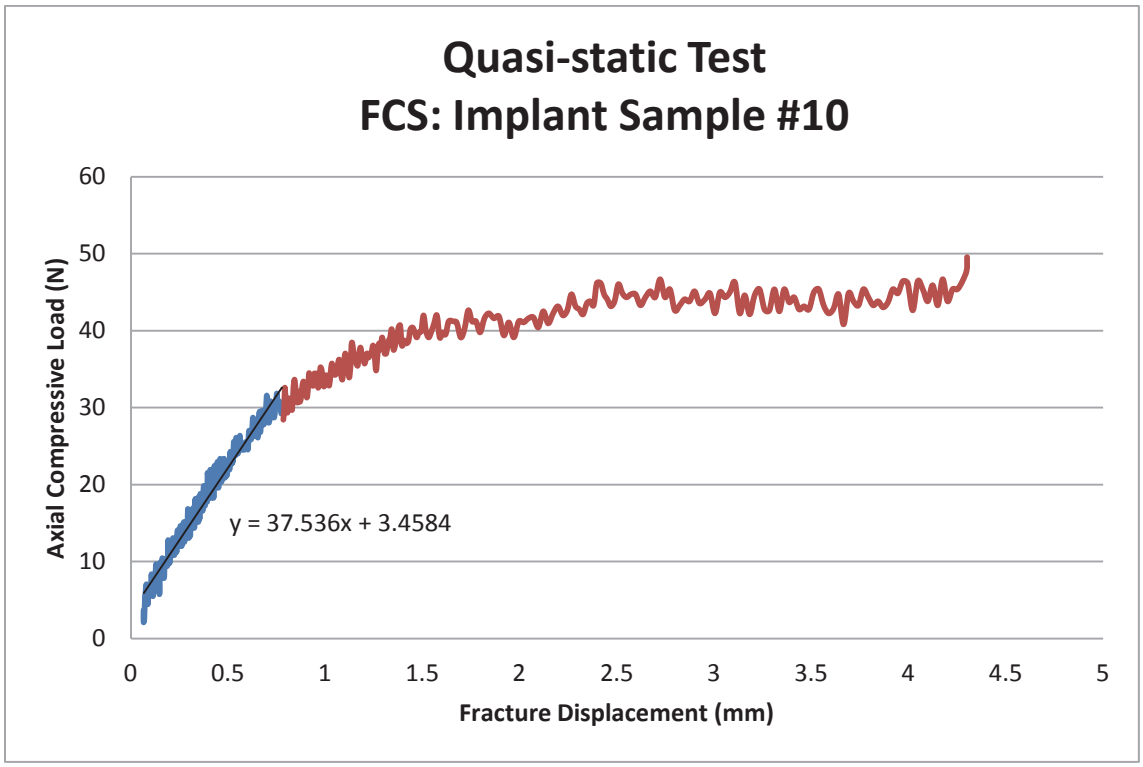

Figure B.4: Quasi-static load versus displacement for FCS sawbone implant sample #10 This plot shows the stiffness and failure strength. The axial stiffness was found to be 37.54 N/mm. Failure strength was defined as 30 N.

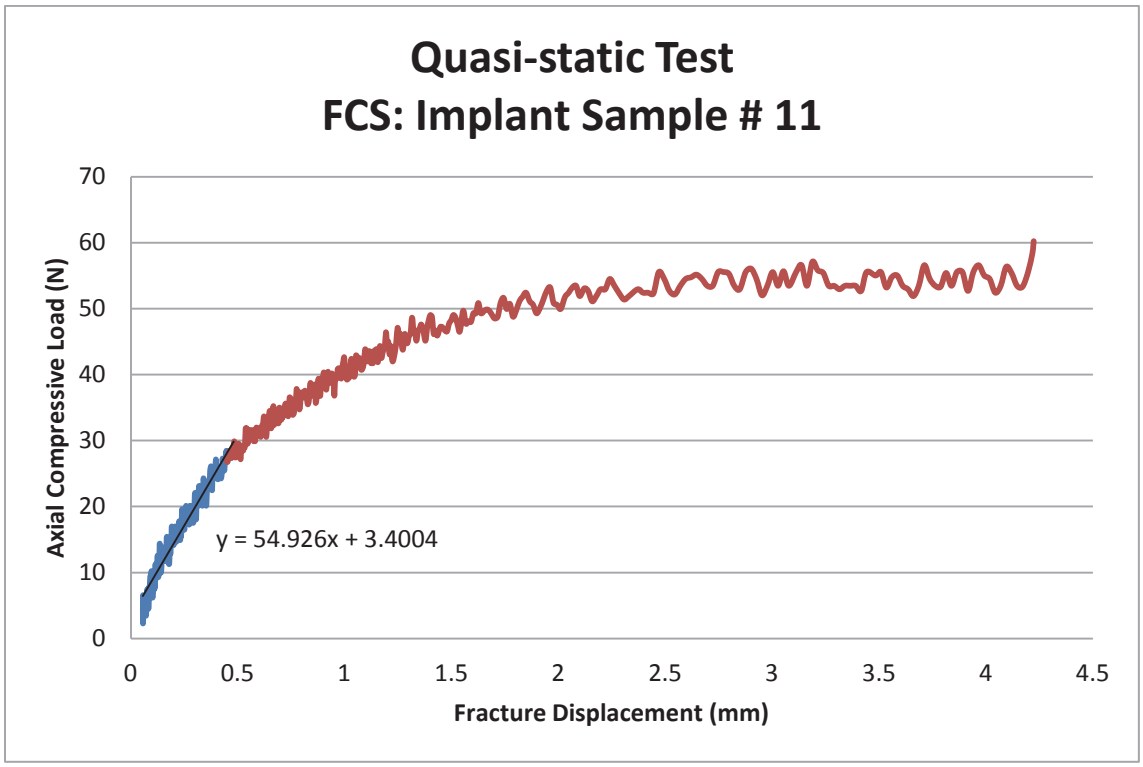

Figure B.5: Quasi-static load versus displacement for FCS sawbone implant sample #11 This plot shows the stiffness and failure strength. The axial stiffness was found to be 54.93 N/mm. Failure strength was defined as 29 N.

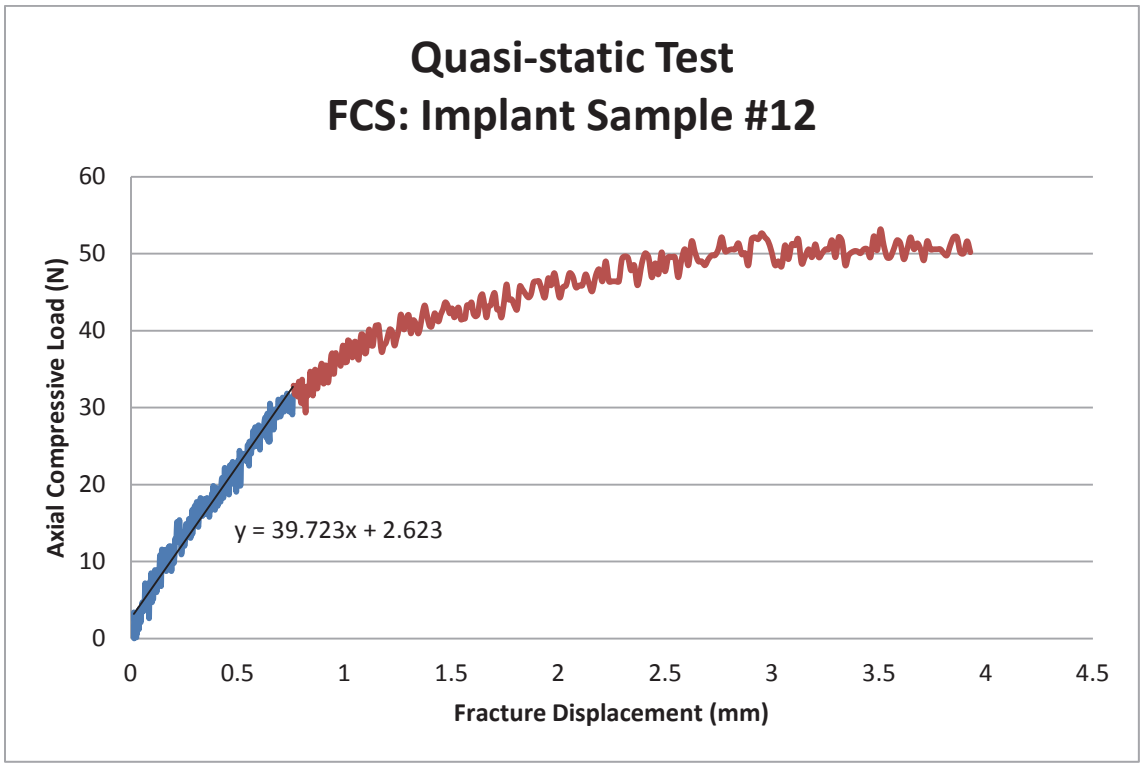

Figure B.6: Quasi-static load versus displacement for FCS sawbone implant sample #12 This plot shows the stiffness and failure strength. The axial stiffness was found to be 39.72 N/mm. Failure strength was defined as 32 N.

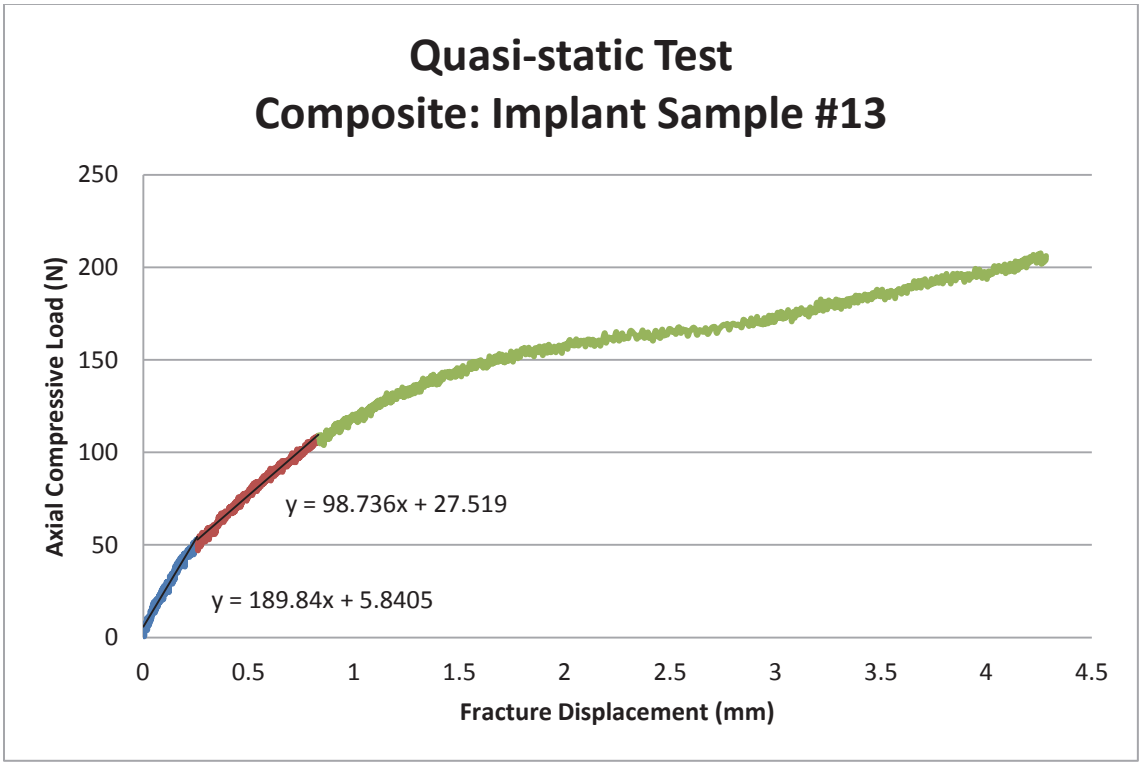

Figure B.7: Quasi-static load versus displacement for composite sawbone implant sample #13 This plot shows the stiffness and failure strength. The axial stiffness was found to be 189.84 N/mm initially and then decreased to 98.74 N/mm. Failure strength was defined as 105 N.

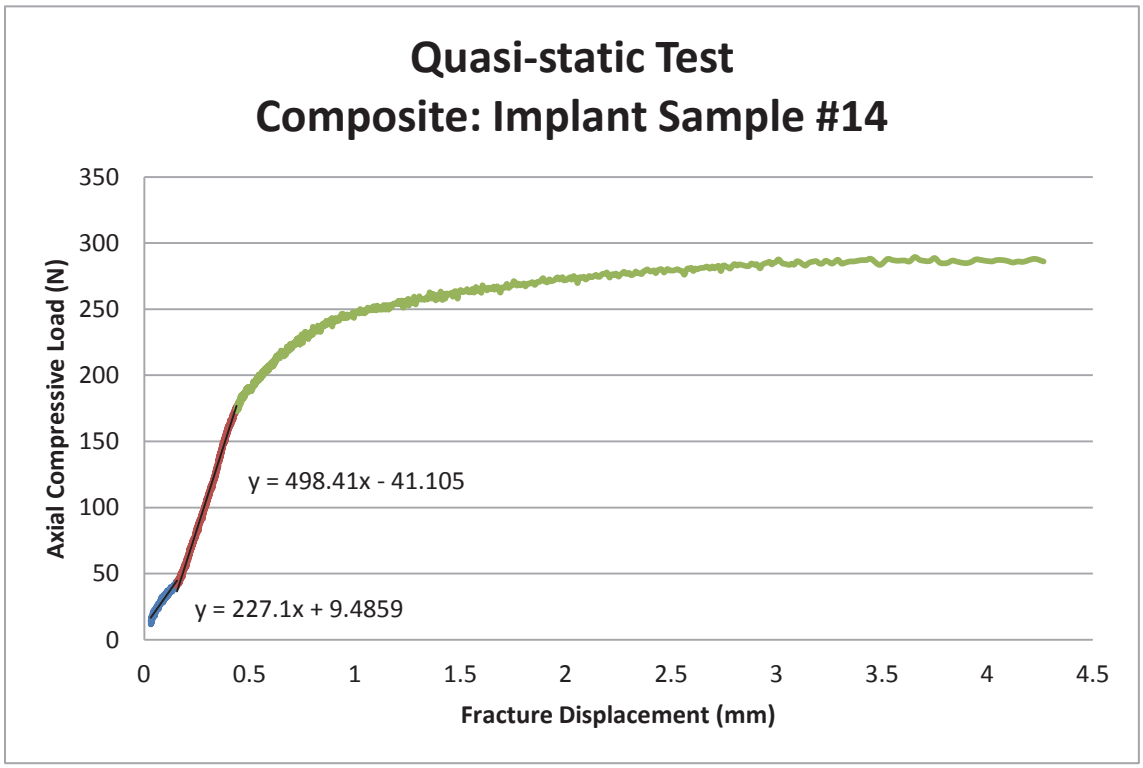

Figure B.8: Quasi-static load versus displacement for composite sawbone implant sample #14 This plot shows the stiffness and failure strength. The axial stiffness was found to be 227.1 N/mm initially and then increased to 498.41 N/mm. Failure strength was defined as 175 N.